Spin Transfer Torque and Dynamics

M. D. Stiles[1] and J. Miltat[2]

[1] Electron Physics Group, National Institute of Standards and Technology, Gaithersburg MD 20899-8412, USA *mark.stiles@nist.gov*
[2] Université Paris XI Orsay, 91405 Orsay, France *miltat@lps.u-psud.fr*

Summary. The currents in magnetic multilayers are spin polarized and can carry enough angular momentum that they can cause magnetic reversal and induce stable precession of the magnetization in thin magnetic layers. The flow of spins is determined by the spin-dependent transport properties, like conductivity, interface resistance, and spin-flip scattering in the magnetic multilayer. When an electron spin carried by the current interacts with a magnetic layer, the exchange interaction leads to torques between the spin and the magnetization. The torque that results from this interaction excites the magnetization when the current is large enough. The qualitative features of the dynamics that result from current-induced torques are captured by a simple model in which the magnetization of the layer is assumed to be uniform. Even greater agreement results when finite temperature effects are included and the magnetization is allowed to vary throughout the film.

1 Introduction

Ferromagnets are stable in multiple states, a property that can be used to store information, as in magnetic tapes, magnetic disk drives, and more recently magnetic random access memory (MRAM). In these magnetic devices, information is stored by switching the magnetic state to the desired configuration. The switching is accomplished by a magnetic field that overcomes the coercive force of the material. In many cases, in MRAM for example, the magnetic fields are generated by electrical currents, in which case they are referred to as Oersted fields. In 1996, Slonczewski [1] and Berger [2] predicted that the current flowing through magnetic multilayers could have a more direct effect on the magnetic state. When a current flows through a ferromagnet, it becomes spin polarized and hence carries angular momentum. The current remains polarized in neighboring non-magnetic layers so that the angular momentum carried by the current can interact with the magnetization in subsequent magnetic layers. The spin current exerts a *spin transfer torque* on the magnetizations in the device. For large enough currents this torque leads to precession and reversal.

In addition to the intrinsic scientific interest in this phenomena, it has several possible applications [3]. As mentioned above, in existing implementations of MRAM, the bits are switched by Oersted fields. The long range of these fields means that reduced fields are applied to neighboring bits. The requirement that only the correct bits switch, and those bits switch reliably, places severe manufacturing constraints on the devices. The possibility that this spin transfer torque could replace the Oersted fields for reversing otherwise stable magnetic configurations in MRAM has inspired a significant amount of the research on this effect. In MRAM, the information is stored in lithographically defined devices. A related technique could be used to store information in media like a magnetic hard disk. In this case, a probe would write magnetic bits with current pulses while being scanned over the media. Another possible application of spin transfer torques comes from the precessional behavior observed in other regimes of operation. Here, the precessional motion converts a DC input current into an AC output voltage. Such behavior might be useful for making current-controlled oscillators.

Since the prediction of the effect in 1996, spin transfer induced magnetization dynamics have been observed in a number of laboratories [4, 5, 6, 7, 8, 9, 10, 11, 12, 13, 14, 15, 16, 17, 18, 19, 20]. These observations have been made in a number of device geometries, some of which are illustrated in Fig. 1, including mechanical point contacts [4, 14], lithographically defined point contacts [5, 11], electrochemically grown nanowires [6], manganite junctions [7], lithographically defined nanopillars [8, 9, 10, 12, 13, 15, 16, 17], tunnel junctions [21, 19, 22, 23], and semiconductor structures [20]. These devices all share two characteristics, magnetoresistive readout of the magnetic state and small cross sectional area.

In all of these devices, the resistance of the device depends on its magnetic state, typically through the giant magnetoresistance effect, so that measuring the resistance of the structure allows the magnetic state to be inferred. Frequently, the layers are fabricated so that one layer, referred to as the free layer, responds to the current induced torques and another, referred to as the fixed layer, does not. This layer stays fixed either because it is exchange biased by being coupled to an antiferromagnet or simply because it is thicker than the free layer and less susceptible to spin transfer torques. Typical measurements report the resistance V/I or differential resistance dV/dI as a function of the current. The signature of a spin transfer effect is a change in the resistance of the device that is asymmetric in the current. The change in resistance indicates that the magnetic configuration has changed. The asymmetry in current indicates that the cause is the spin transfer effect rather the the Oersted field. Any changes in the magnetic configuration due to the Oersted field alone are expected to be symmetric in the current, where as the spin transfer torque is explicitly asymmetric.

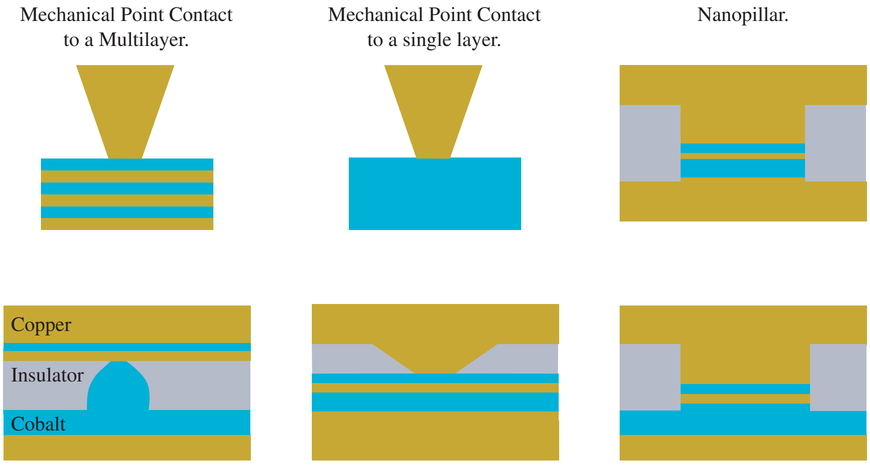
Mechanical Point Contact to a Multilayer.

Mechanical Point Contact to a single layer.

Nanopillar.

Lithographically defined point contact.

Lithographically defined point contact.

Nanopillar with extended fixed layer.

Fig. 1. Schematic experimental geometries. In each geometry, copper layers are tan, cobalt layers are blue, and insulating layers are gray, as labeled in the lower left panel. Other ferromagnetic materials may be substituted for Co and non-magnetic materials for Cu.

All of the devices have small cross sectional areas for two reasons. First, it turns out that fairly high current densities are required to transfer enough angular momentum to affect the magnetization. The heat generated by the current would destroy the device if it were not concentrated into a small area that is in good thermal contact to a large mass. Second, the relative effect of the Oersted field as compared to the direct spin transfer decreases as the cross sectional area decreases. For a uniform current density and uniform magnetization, the spin transfer torque is uniform. The spin transfer torque then couples strongly to the uniform precession mode. The torque per area is independent of the area for constant current density. The Oersted fields on the other hand are non-uniform and do not couple to the uniform precession of a uniform magnetization. As the cross sectional area decreases, the magnetization tends to become more uniform and it becomes harder to excite non-uniform modes. In addition, the maximum Oersted field decreases as the area decreases for a constant current density. Inside a wire with a circular cross-section for instance, the Oersted field increases linearly from the origin. Thus, the smaller the diameter, the smaller the maximum Oersted field.

The simplest way to get a small cross sectional area is through a mechanical point contact. In these devices, a sharp tip is lightly pressed into a sample. By monitoring the resistance of the junction while the tip is pressed into the sample, it is possible to stop when the contact area is small. The first observation of a spin transfer effect by Tsoi et al. [4] used such a mechanical point contact to a magnetic multilayer. They observed peaks in the differential resistance for only one polarity of the current, see Fig. 2, and interpreted them as evidence of a spin-transfer-torque induced transition into a precessing state. The current at which this peak occurred increased linearly with increasing magnetic field. Subsequent measurements on this system [24], showed that as the current was increased to values greater than that of the peak, the system made a transition into a state that coupled strongly to externally applied microwaves.

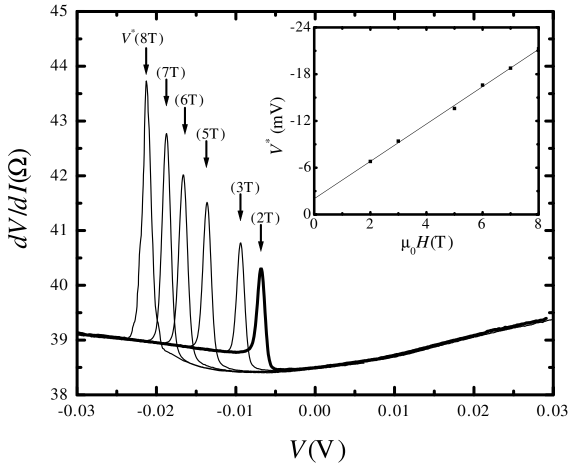

Fig. 2. Differential resistance of a mechanical point contact as a function of current for various applied magnetic fields. The peak in differential resistance that occurs for only one current direction indicates a spin transfer effect. The inset shows that the current at the peak in the differential resistance increases linearly with the applied field. Used by permission from Tsoi et al. [4].

More controlled devices can be made through nanolithography. Myers et al. [5] fabricated lithographically defined point contacts and Katine et al. [8] fabricated nanopillars. In high magnetic fields, both of these systems exhibited a similar peak in the differential resistance as seen in the mechanical point contact experiment. However, in lower fields, both showed hysteretic switching between two stable states, see Fig. 3. The resistivity of these states was equal to the resistivity of the parallel and antiparallel magnetic alignments measured in more standard magnetoresistance measurements. These experiments demonstrated that spin transfer torques could be used to switch the configuration of bistable magnetic devices. Subsequent experiments have shown that the hysteresis loops can be quite square showing clean switching between fully parallel and fully antiparallel alignments. Applied fields greater than the coercive field inhibit a stable antiparallel state and the system switches from a parallel configuration into more complicated states including precession.

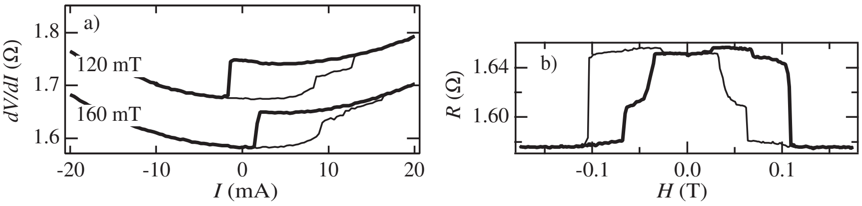

Fig. 3. Differential resistance. (a) dV/dI of a pillar device exhibits hysteretic jumps as the current is swept. The current sweeps begin at zero; light and dark lines indicate increasing and decreasing current, respectively. The traces lie on top of one another at high bias, so the 120.0 mT trace has been offset vertically. (b) Zero-bias magnetoresistive hysteresis loop for the same sample. Used by permission from Katine et al. [8]

Establishing the rest of the phenomenology for the behavior of these devices requires measurement of the time or frequency response of the resistance. Two processes dominate these measurements, two-level switching and precession. Hysteresis, as seen in Fig. 3 is always a time dependent phenomenon. Bistability is observed for a range of currents because the different states of the system are metastable. A system at finite temperature will find its ground state over a long enough measurement time. On even longer time scales, the system would exhibit two level switching between the two states with the relative time spent in each state dependent on the energy difference between them compared to the temperature. The rates for two level switching depend strongly on external parameters, and the switching can be quite prominent for the right choices of parameters [4, 25, 12, 26, 27].

Two level switching is one possible source for the low frequency noise frequently observed in these systems [28]. The frequency distribution of the noise is typically described by the power spectrum density. Sometimes the noise has a Lorentzian power spectrum density characteristic of true two level switching, but these systems also exhibit a variety of more general power spectral densities.

In the magnetic nanopillars, at low applied fields, the switching time is much longer than the measurement time for a range of currents and the system displays hysteresis. The width of the hysteretic region depends on the measurement time and temperature [25]. As the applied field is increased, the lifetime of the two states decreases and eventually crosses over with the measurement time, see Fig. 4. At this point, the hysteretic steps in the resistance combine and become a broadened, reversible transition between the two states. Urazhdin et al. [12] showed that the derivative of this transition gives the peak seen in the differential resistance.

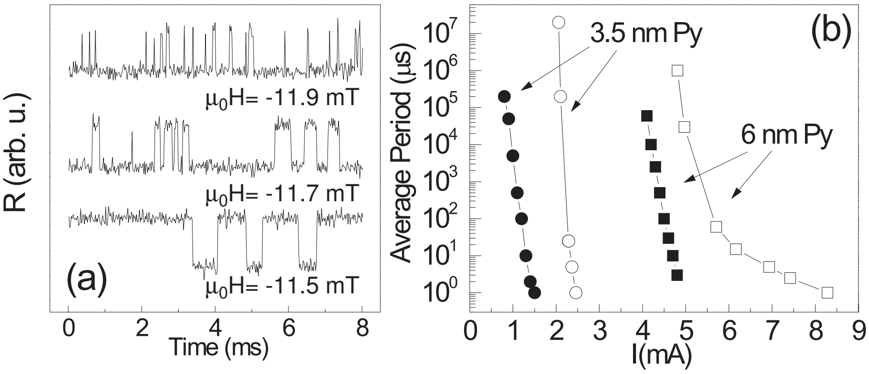

Fig. 4. Two-level switching. (a) Time traces of the static resistance $R = V/I$ at $T = 295$ K at different applied fields H. Top two curves are offset. (b) Current dependence of the average telegraph noise period. The applied field along the in-plane easy axis H was adjusted approximately linearly with current I, so that the average dwell times in antiparallel and parallel states were equal. Solid circles: $T =$ 295 K, $\mu_0 H = 9.3$ mT to 12.1 mT; open circles: same sample at 4.2 K, $\mu_0 H = 30.0$ mT to 31.5 mT; solid squares: different sample at 295 K, $\mu_0 H = 11.3$ mT to 12.3 mT; open squares: same sample at 4.2 K, $\mu_0 H = 30.0$ mT to 45.0 mT. Used by permission from Urazhdin et al. [12]

A topic of significant controversy in the interpretation of the two level switching is the degree to which there is heating of the magnetic degrees of freedom above the temperatures of the electronic and lattice degrees of freedom. Much of the experimental results can be understood using models based on magnetic heating [12, 26]. However, careful investigations of the temperature dependence at low temperatures by Krivorotov et al. [29] rule this out, at least for the system studied in that experiment.

The precessing state was first established through peaks in the power spectrum density in frequency dependent measurements by Kiselev et al. [28] and Rippard et al. [30]. Precession was observed for currents near the peak in the differential resistance previously attributed to precession, but also for a range of currents that extended below the peak. In these measurements, a DC input current generates a high frequency precessing state. Since the magnetization varies rapidly, the resistance does as well. While the precession is fast on human time scales, on the order of GHz, it is slow on electronic time scales, so the time varying resistance leads to a time varying voltage, which is what is measured, see Fig. 5. In some geometries, the resonance can be extremely narrow as a function of frequency, Q values as large as 18 000 have been observed [31]. These narrow resonances raise the possibility of using spin transfer effects to make current controlled oscillators for use in high speed electronic applications.

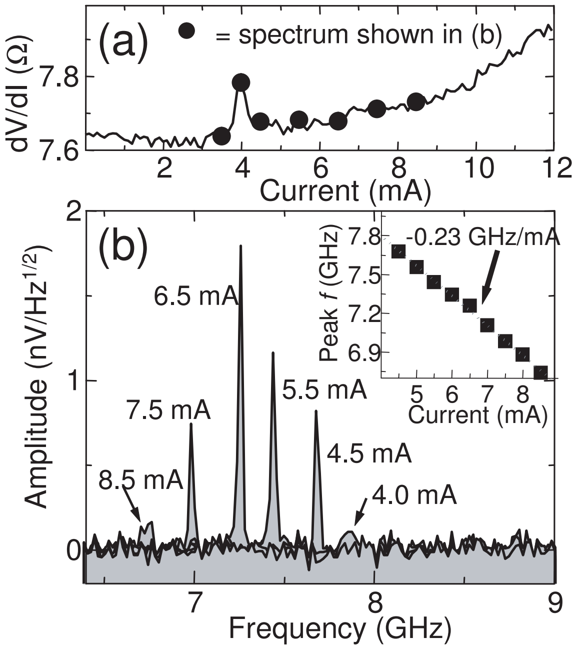

Fig. 5. Precession. (a) Differential resistance dV/dI vs. current I for $\mu_0 H = 0.1T$ along the in-plane easy axis. (b) High frequency spectra taken at several different values of current through the device, corresponding to the symbols in (a). Variation of frequency f with current (inset). Used by permission from Rippard et al. [30]

A number of experiments have tested the predictions of Slonczewski's model for spin transfer torques. Several authors [8, 32, 33] have compared predictions of macrospin simulations, see Section 4, with measured results, for example. The computed phase diagrams, the behavior as a function of applied magnetic field and current, qualitatively agree with those measured experimentally, see Fig. 6 for a measured phase diagram. Fully quantitative agreement is still difficult because many of the necessary parameters are not independently measurable.

Measurements of the thickness dependence [34] show that the critical currents increase as the thickness of the free layer increases. This behavior is consistent with the torque being an interface effect as opposed to an effect that is active throughout the bulk of the free layer. Measurements of the dependence of the critical current on the initial angle between the free and fixed layers [35] show the expected increase in critical current as the fixed layer magnetization becomes perpendicular to the easy axis of the free layer. While

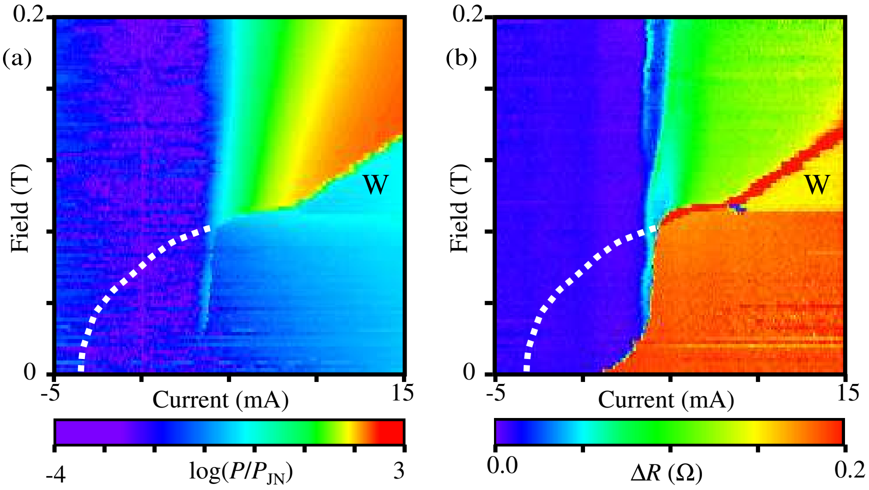

Fig. 6. Phase diagram. (a), Microwave power measured in a nanopillar plotted in color scale versus current I and applied field H along the in-plane easy axis. Current is swept from negative to positive values. The dotted white line shows the position of the antiparallel to parallel transition when current is swept in the opposite direction. (b), Differential resistance plotted in color scale. A smooth current-dependent, H-independent background has been subtracted. Resistance changes are measured relative to the parallel state. The "W" region is discussed in the text. Used by permission from Kiselev et al. [28]

asymmetry in the current is taken as an indication of spin transfer effects, such asymmetry only holds if the fixed layer and free layer are inequivalent. In one experiment [36], a symmetric structure showed symmetric behavior in current.

Several experiments have studied the changes in behavior due to changes in material properties. It is established that it is possible for ferromagnetic layers to polarize the currents with different signs, that is either majority or minority carriers can dominate the current. Measurements [37] show that the sign of the current that leads to an instability in the free layer depends on the spin-dependent conductivity of the fixed layer, but not the free layer. The model for spin transfer described in Sec. 3 shows that such dependence is expected for typical geometries. Other experiments [11] showed that the dependence of the critical current on the saturation magnetization and the polarization of the current are consistent with this model for spin transfer torques.

A set of related experiments grew out of the idea of repeating the original mechanical point contact experiment [4] but with a single film of Co rather than a multilayer. Ji et al. [14, 38] observed very similar peaks in the differential resistance as were observed for the multilayer. Nanopillar experiments by Özyilmaz et al. [39] also showed peaks that were asymmetric in current and evolved with magnetic field. These results are somewhat surprising because the models based on the work by Slonczewski depend on non collinearity between the magnetizations of the two layers to generate the dynamics. Section 3.7 discusses how these experiments might be explained by closely related models.

The rest of this chapter is organized to give a pedagogical understanding of spin transfer torques, in particular, the understanding that has evolved from Slonczewski's original work. Each section gives a result that forms the basis of the subsequent section, providing a hierarchical structure for the explanation. Section 2 addresses the question, "where does the spin transfer torque come from?" The answer is found in quantum mechanical calculations of the behavior of electrons scattering from magnetic interfaces. Given the torque as a function of the spin current raises the question, addressed in Section 3, "how big is the spin current?" Determining the spin current for different magnetic configurations is the domain of semiclassical calculations of the transport. The results of Section 2 enter these calculations as boundary conditions. Having found the spin transfer torque as a function of the magnetic configuration and current, leads to the next question, "how does the system respond?" Micromagnetic calculations of various types address this question, ranging from stability analysis of simple models to full micromagnetic simulations. These are discussed in Section 4.

2 Quantum scattering

In this section, we describe how a spin current incident on an interface with a ferromagnet exerts a torque on the magnetization. We start by considering the equations of motion for the spin density in the regions near an interface between a non-magnetic material and a ferromagnet. A variety of effects lead to a transfer of angular momentum from the flowing electrons to the magnetization. For many systems, there is essentially complete transfer of the transverse incident spin current. The transferred angular momentum can be interpreted as a torque.

The ultimate driving force for magnetic effects is the exchange interaction. In atomic physics, the exchange interaction causes most atoms to have magnetic moments. Hund's first rule describes the energetic considerations of arranging the electrons in a partially filled atomic level. It states the electrons should have as many spins as possible parallel. To understand why this is so, recall that the electronic wave function of an atom must be antisymmetric. A consequence of this antisymmetry is that the wave function must go to zero whenever two parallel spins are close to each other. This Pauli repulsion means that the Coulomb energy for parallel spins is lower than that for antiparallel spins. Within a partially filled level, where all states have the same kinetic energy in the absence of interactions, any cost in kinetic energy is smaller than the gain in Coulomb energy. In solids, where the electron states form bands, the situation is more complicated because it always costs kinetic energy when a minority electron is promoted into a majority electron. In most solids, the cost is too great for a polarization to develop. Nonetheless, in the transition metal ferromagnets, Fe, Co, and Ni, this intraatomic exchange is large enough to cause a ferromagnetic ground state. The resulting net polarization of the electronic spins means that majority (spins parallel to the majority of spins) and minority (spin antiparallel to the majority) electrons have different properties. These differences drive the effects described in the rest of this chapter.

In solid state physics, there is an additional consequence of the exchange interaction that is commonly discussed, interatomic (as opposed to intraatomic) exchange. In transition metal ferromagnets, this is the interaction that drives the spins on neighboring atoms to be parallel to each other. A common representation of this interaction is the Heisenberg form, $-J\mathbf{S}_i \cdot \mathbf{S}_j$, where $\mathbf{S}_i$ and $\mathbf{S}_j$ are the net spins on neighboring sites and J is the strength of the interaction. In micromagnetics, a mesoscale, continuum model for magnetism, the interatomic exchange interaction has the form

$$\frac{A_{\mathrm{ex}}}{M_{\mathrm{S}}^2} \int d^3r \left[(\boldsymbol{\nabla} M_x(\mathbf{r}))^2 + (\boldsymbol{\nabla} M_y(\mathbf{r}))^2 + (\boldsymbol{\nabla} M_z(\mathbf{r}))^2 \right] , \tag{1}$$

where A_{ex} is the exchange constant, and M_x is the x component of the vector magnetization $\mathbf{M}$. This energy has its minimum when all gradients are zero and the magnetization is uniform. This form of the exchange interaction will be important in Sec. 4, which discusses the time evolution of the magnetization.

A spin current consists of spins moving. Since both spin and velocity are vectors, the spin current is a tensor quantity. Classically, it is the outer product of the electron's spin and its velocity, $\mathbf{Q} = \mathbf{S} \otimes \mathbf{v}$. In a quantum mechanical description of an ensemble of spins, the spin density and the spin current are

$$\begin{aligned} \mathbf{s}(\mathbf{r}) &= \sum_{i\sigma\sigma'} \psi^*_{i\sigma}(\mathbf{r})\, \mathbf{S}_{\sigma,\sigma'}\, \psi_{i\sigma'}(\mathbf{r}) \\ \mathbf{Q}(\mathbf{r}) &= \sum_{i\sigma\sigma'} \mathrm{Re}\left[\psi^*_{i\sigma}(\mathbf{r})\, \mathbf{S}_{\sigma,\sigma'} \otimes \hat{\mathbf{v}}\, \psi_{i\sigma'}(\mathbf{r}) \right] , \end{aligned} \tag{2}$$

where $\hat{\mathbf{v}}$ is the velocity operator, $\mathbf{S}_{\sigma,\sigma'}$ are the spin operators ($\hbar/2$ times Pauli spin matrices), and the sum over i is over all occupied states. While the spin current for a collection of electrons cannot generally be factored into the outer product of a net spin direction and a net velocity vector, for one dimensional problems it usually can. In this case it is useful to factor the spin current into the outer product of a dimensionless spin direction $\hat{\mathbf{s}}$ and the number current $\mathbf{j}$ times a dimensionless, scalar polarization P

$$\mathbf{Q} = (\hbar/2)\, P\, \hat{\mathbf{s}} \otimes \mathbf{j}. \tag{3}$$

At various points in this chapter we will discuss the direction associated with a spin current even though the spin current is a tensor. The direction we mean is the direction of the spin taken from this factorization. In addition, transverse (or perpendicular) spin currents $\mathbf{Q}_\perp$ are the components of $\mathbf{Q}$ such that $\hat{\mathbf{M}} \cdot \mathbf{Q}_\perp = 0$, or

$$\mathbf{Q}_\perp = (\hbar/2)\, P\, [\hat{\mathbf{s}} - \hat{\mathbf{M}}(\hat{\mathbf{s}} \cdot \hat{\mathbf{M}})] \otimes \mathbf{j}, \tag{4}$$

in terms of the factorization in Eq. (3).

To develop the equation of motion for the spin density, it is useful to first consider the related expression for the electron number density n. The equation of motion for the number density is found by taking its commutator with the Hamiltonian. The number density commutes with each term in the Hamiltonian except the kinetic energy. The result is the familiar continuity equation

$$\frac{\partial n}{\partial t} = -\boldsymbol{\nabla} \cdot \mathbf{j}. \tag{5}$$

This equation simply states that the time rate of change in the density is given by the net flow of electrons into a region.

When this procedure is repeated for the spin density, the kinetic energy produces a similar term, but there are other terms in the Hamiltonian that do not commute with the spin density

$$\frac{\partial \mathbf{s}}{\partial t} = -\boldsymbol{\nabla} \cdot \mathbf{Q} + \mathbf{n}_{\mathrm{ext}}. \tag{6}$$

where $\boldsymbol{\nabla} \cdot \mathbf{Q} = \partial_k Q_{ik}$, summing over the repeated index k. The other terms in the Hamiltonian, which do not commute with the spin density, like the Zeeman interaction and the magnetocrystalline anisotropy, give rise to $\mathbf{n}_{\mathrm{ext}}$, the external torque density . The interpretation of Eq. (6) is similar to the continuity equation. The time rate of change in the spin density is given by the net flow of spins into a region plus the torques that tend to rotate the spin density.

There are two contributions to the spin current. One contribution $\mathbf{Q}_{\mathrm{ex}}$ is the mediator of the exchange interaction and is carried by all of the electrons contributing to the magnetization. In general, each electronic eigenstate in a solid carries a spin current. When a ferromagnet has a spatially uniform magnetization and there is no applied current, the spin current carried by the right moving states exactly cancels the spin current carried by the left moving states. However, when the magnetization direction in a ferromagnet is non-uniform, the spin currents carried by the eigenstates do not cancel, leaving a net spin current even in the absence of an applied current. The gradient of this spin current gives a torque that tends to rotate the inhomogeneous magnetization $\mathbf{n}_{\mathrm{ex}} = -\boldsymbol{\nabla} \cdot \mathbf{Q}_{\mathrm{ex}}$. This torque is the microscopic torque corresponding to the micromagnetic exchange interaction described in Eq. (1).

The contribution to the spin current of interest to this chapter, $\mathbf{Q}_{\mathrm{trans}}$, is the transport spin current, which is carried by an imbalance in the populations of the states near the Fermi energy. This strictly non-equilibrium spin current comes from an imbalance in the populations of the right moving and left moving states rather than a net spin current carried by equal populations of both. For the rest of this article we treat $\mathbf{n}_{\mathrm{ex}}$ as an explicit torque, grouping it into $\mathbf{n}_{\mathrm{ext}}$ and we refer to the transport spin current as $\mathbf{Q}$ dropping the "trans" label. This is the normal description for micromagnetics.

In transition metals, in which the orbital moment only makes a small contribution to the magnetization, multiplying the spin density by $g_e \mu_{\mathrm{B}}/\hbar$ gives the magnetization density. It is unfortunate that since $g_e \approx -2.002319$, the electron's spin and moment are opposite to each other. This leads to confusion when discussing spins in ferromagnets [40]. To minimize confusion in this discussion of transport, we will typically assume that the magnetization $\mathbf{M}$ is in the $-\hat{\mathbf{x}}$ direction so that the *ferromagnetic spin density* $\mathbf{s} = -\hbar\mathbf{M}/(|g_e|\mu_{\mathrm{B}})$ is in the $\hat{\mathbf{x}}$ direction. Thus, majority electrons have their spins along $\hat{\mathbf{x}}$ and can be referred to as "spin up". Their moments are along $-\hat{\mathbf{x}}$, parallel to the magnetization. The subscript $\uparrow$ refers to majority electrons, which have moments parallel and spins antiparallel to the magnetization. The subscript $\downarrow$ refers to minority electrons.

If the spin density is converted to magnetization, Eq. (6) becomes the Landau-Lifshitz-Gilbert equation without damping [105]. Damping is missing because Eq. (6) has been written for a single particle Hamiltonian. A more complete Hamiltonian that included the many body interactions with other parts of the system would lead to additional terms. Some of these terms can be combined to give phenomenological contributions to the right hand side

$$\frac{\partial \mathbf{s}}{\partial t} = -\boldsymbol{\nabla} \cdot \mathbf{Q} + \mathbf{n}_{\mathrm{ext}} - \alpha \hat{\mathbf{s}} \times \frac{\partial \mathbf{s}}{\partial t} - \hat{\mathbf{s}} \frac{\delta s}{\tau_{\mathrm{sf}}}, \tag{7}$$

where $\hat{\mathbf{s}}$ is a unit vector in the direction of the spin density and δs is spin density in excess of the equilibrium value (spin accumulation). The third term on the right hand side is the phenomenological damping with damping parameter α. The last term leads to relaxation of any deviation of the ferromagnetic spin density from its equilibrium value. It is characterized by a spin-flip scattering time, τ_{sf} and is discussed at greater length in Section 3.

It turns out that the spin transfer torque of interest in this article is an interface effect [1, 41, 42, 43], so we need to consider the equation of motion for the spin density near the interface. We consider a pillbox of area A that extends from just inside the non-magnet to just inside the ferromagnet, see Fig. 7. If we integrate the equation of motion for the spin density, Eq. (6) over the volume of the pillbox, the divergence of the spin current becomes a surface integral of the flux. Note that the spin flux is a vector because it is given by a tensor spin current dotted into the interface normal. For a uniform spin current incident from the non-magnet, the spin flux through the interface in the non-magnet has a contribution from the incident and the reflected spin currents $(\mathbf{Q}_{\mathrm{in}} + \mathbf{Q}_{\mathrm{ref}}) \cdot (-\hat{\mathbf{z}})A$. For this interface, the interface normal is $-\hat{\mathbf{z}}$. For the interface in the ferromagnet, the transmitted spin current in $\mathbf{Q}_{\mathrm{tr}} \cdot \hat{\mathbf{z}}A$. The total change in spin flux acts like a torque on the magnetization in the pillbox

$$\mathbf{N}_{\mathrm{c}} = (\mathbf{Q}^{\mathrm{in}} - \mathbf{Q}^{\mathrm{tr}} + \mathbf{Q}^{\mathrm{ref}}) \cdot A\hat{\mathbf{z}} \approx \mathbf{Q}^{\mathrm{in}}_{\perp} \cdot A\hat{\mathbf{z}}. \tag{8}$$

The equality in this expression holds for all systems. In the rest of this section we show that the approximate form, where $\mathbf{Q}^{\mathrm{in}}_{\perp}$ is the part of $\mathbf{Q}^{\mathrm{in}}$ with its spin direction perpendicular to $\hat{\mathbf{s}}$, holds for transition metal interfaces.

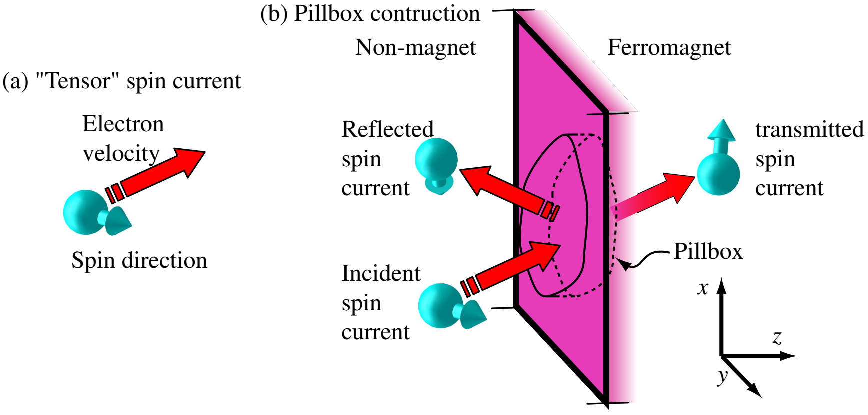

Fig. 7. (a) An electron moving in one direction with its spin in another illustrating a tensor spin current. (b) A pillbox around interface for computing the interfacial torque.

To proceed, it is instructive to consider the electronic structure of typical materials used to study the spin transfer effect. The electronic structure of transition metal ferromagnets is complicated. Ferromagnetism in transition metals is driven by atomic-like intraatomic exchange and correlation effects in the partially filled *d*-electron shells. The atomic-like effects suggests a localized description of this part of the electronic structure. However, the *d* orbitals are strongly hybridized with both *d* and *s*-*p* orbitals on neighboring atoms. The strong hybridization suggests an itinerant description of the electronic structure. Reconciling these aspects of the physics is an ongoing area of research, and the resulting models are not simple [44]. Here, we adopt the approach used in most calculations of transition metal electronic structure, the local spin density approximation (LSDA) [45]. This approximation accurately describes the itinerant aspects of the electronic structure while treating the atomic-like exchange and correlation effects in mean field theory. This approximation was derived for computing the ground state properties of materials. For transition metal ferromagnets, it works quite accurately for properties like the cohesive energy, equilibrium lattice constant, and the magnetic moment [46]. Formally, it is not justified for computing the electronic structure, but it is a good combination of simplicity and accuracy even for this case.

The Fermi surfaces of Cu and face-centered cubic (fcc) Co calculated using the LSDA are shown in Fig. 8. The Fermi surfaces for the Cu and Co majority electrons are close to free electron like, but that of the Co minority electrons is not. The complicated Fermi surface for the minority electrons is a consequence of the strong hybridization between the *d*-levels and also between the *d*-levels and the *s*-*p* levels. The differences in the Fermi surfaces lead to different properties for majority and minority electrons. Two important spin-dependent properties are the conductivity and the interface reflection. The former will be discussed in the next section and the latter will be of importance below.

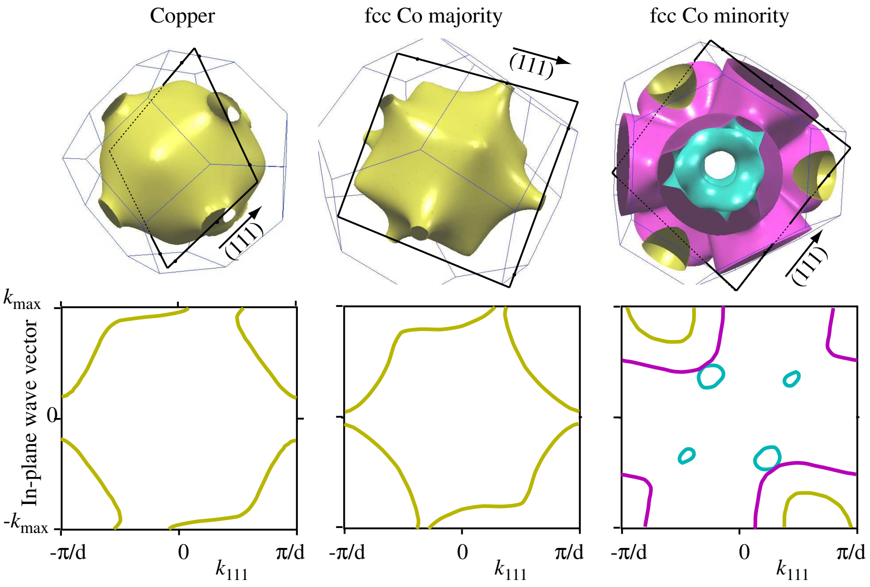

Fig. 8. The Fermi surfaces for Cu and fcc Co. The top three panels show 3-dimensional representations of the three Fermi surfaces. For the Co minority states, three bands intersect the Fermi energy, each is indicated in a separate color. Slices through the Fermi surfaces are indicated for each. The bottom three panels show these slices and the intersection of the slices with the Fermi surfaces. At (111) interfaces, electron states with the same in-plane wave vector, that is, along a horizontal line in the lower panels, couple across an interface. In Co, the Fermi energy is above the majority *d*-bands, but in the middle of the minority *d*-bands, so the majority Fermi surface is very similar to that for Cu, but the minority surface is very different.

Other models that are used to describe magnetic multilayers are the *s*-*d* model and the related local moment model. In these models, the *d* electrons are responsible for the magnetism and their itinerancy is ignored. The *s* electrons are responsible for transport, and they are only weakly spin-dependent. In these models, the Fermi surfaces are largely spin-independent. However, these models include spin-dependent scattering rates so they are able to capture most of the details of transport in these systems. However, when the details of the states at the Fermi surface are important, caution is required.

The behavior of spin currents at interfaces is dominated by the spin dependent reflection of electrons. The exchange interaction in the ferromagnet gives the electrons at the Fermi energy different properties depending on whether their moments are parallel or antiparallel to the magnetization. As a consequence, the reflection amplitudes for electrons coming from a non-magnet and scattering from the interface with a ferromagnet depend on whether the electron's moment is parallel, $R_\uparrow$, or antiparallel, $R_\downarrow$, to the magnetization. The transmission amplitudes , $T_\uparrow$ and $T_\downarrow$, are similarly spin dependent. The spin dependent reflection gives rise to a spin dependent interface resistance even for ideal interfaces [47]. These resistances will be discussed further in the next section, which deals with transport.

The reflection and transmission of electrons with moments at arbitrary angles to the magnetization (along $-\hat{\mathbf{x}}$) determines the torque. The behavior of these electrons is found with little additional work. Since electrons are spin-1/2 particles, the state of an electron with a spin at a polar angle θ and azimuthal angle ϕ is a coherent superposition of the spin up state and the spin down state

$$|\theta,\phi\rangle = \cos(\theta/2)\, e^{-i\phi/2}\, |{\uparrow}\rangle + \sin(\theta/2)\, e^{i\phi/2}\, |{\downarrow}\rangle\,. \tag{9}$$

Note that although polar coordinates are usually defined with respect to the z-axis, here we define them with respect to the x-axis for consistency with the coordinate choice made in the rest of this chapter. Thus, the reflection amplitudes for majority and minority electrons determine the reflection amplitudes for spins at arbitrary angles. When an electron starting in the non-magnet in the state $e^{ikz}\,|\theta,\phi\rangle$ reflects, it comes back in a different state

$$e^{-ikz}\left[R_\uparrow \cos(\theta/2)\, e^{-i\phi/2}\, |{\uparrow}\rangle + R_\downarrow \sin(\theta/2)\, e^{i\phi/2}\, |{\downarrow}\rangle\right]. \tag{10}$$

The reflected electron is rotated with respect to incident electron. The new polar angle θ' is determined by the relative magnitudes of the reflection amplitudes, $\tan(\theta'/2) = |R_\downarrow/R_\uparrow|\tan(\theta/2)$. The new azimuthal angle is determined by the relative phases of the reflection amplitudes $\phi' = \phi + \mathrm{Im}[\ln(R^*_\uparrow R_\downarrow)]$. For cartoons of these rotations, see Fig. 9.

Similar considerations apply to the transmitted electrons but with an additional complication. When the electrons are in the ferromagnet, the different spin components have different wave vectors, $k_\uparrow$ and $k_\downarrow$. The differences between the majority and minority Fermi surfaces seen in Fig. 8 illustrate the general difference between the wave vector for the two different states. The consequence of this difference is that the phase between the up spin and down spin amplitudes, $e^{i(k_\uparrow - k_\downarrow)z}$ changes as the electron penetrates further into the ferromagnet. As can be seen from Eq. (9), a change in the relative phase corresponds to a change in the azimuthal angle at which the spin is directed. This changing azimuthal angle is simply precession around the magnetization [48]. For cartoons of this precession, see Fig. 9.

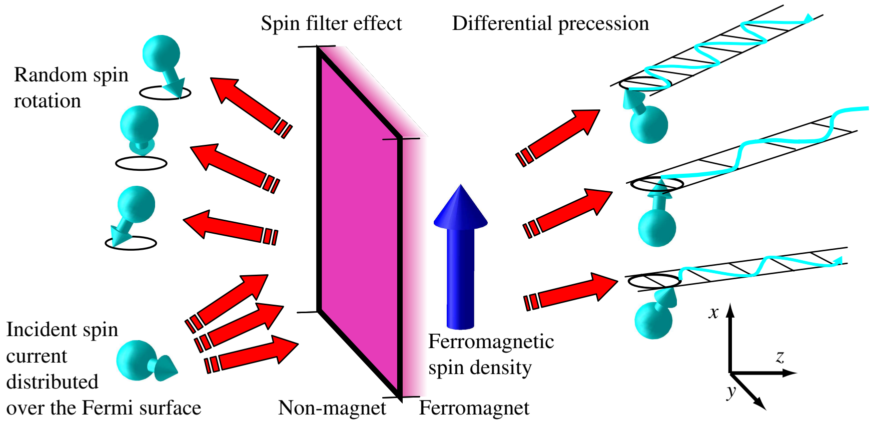

Fig. 9. Mechanisms contributing to absorption of incident transverse spin current. Electrons incident from the non-magnet (lower left) are distributed over a distribution of states represented by three different incident directions. All of these electrons are in the same spin state, which is transverse to the ferromagnetic spin density (blue arrow). The reflected electron spins have predominantly minority character and their transverse components are distributed over many directions (random spin rotation) because of the variation over the Fermi surface of the phases of the reflection amplitudes. The transmitted electron spins precess as they go into the ferromagnet because the wave vectors for the majority and minority components are different. Electrons with different initial conditions precess at different rates, leading to classical dephasing (differential precession).

To see the consequences of non-collinear spin scattering, it is useful to consider a simple model first described by Waintal et al. [41] in which the reflection probability for minority spins is one and for majority spins is zero. While this situation is not typical, neither is it uncommon [49]. Imagine an electron with its spin perpendicular (along $\hat{\mathbf{z}}$) to the ferromagnetic spin density (along $\hat{\mathbf{x}}$) scattering from this interface. This electron is a coherent superposition of majority and minority amplitudes. After scattering from the interface, all of the majority amplitude is transmitted into the ferromagnet and all of the minority amplitude is reflected back into the non-magnet. The incident, reflected and transmitted spin currents are

$$\begin{aligned}\mathbf{Q}_{\mathrm{in}} &= \frac{\hbar}{2}\hat{\mathbf{z}}\otimes v\hat{\mathbf{z}}\\ \mathbf{Q}_{\mathrm{refl}} &= \frac{\hbar}{4}(-\hat{\mathbf{x}})\otimes(-v\hat{\mathbf{z}})\\ \mathbf{Q}_{\mathrm{trans}} &= \frac{\hbar}{4}\hat{\mathbf{x}}\otimes v\hat{\mathbf{z}}\end{aligned}\qquad(11)$$

Computing the torque on the ferromagnetic spin density inside the pillbox of Fig. 7 as in Eq. (8) gives $\mathbf{N}_{\mathrm{c}} = \hat{\mathbf{z}}Av\hbar/2$. This simple model illustrates two key aspects of the scattering process. The first, which holds in all cases, is that the spin current along the magnetization is conserved. In this example, there is no spin current along the magnetization in the incoming state, and no net spin current along the magnetization in the outgoing states. The torque is always perpendicular to the magnetization. The second aspect is that the reflected and transmitted spin currents have no transverse components. This feature is only approximately true in general as is discussed below. In combination, these two aspects give the simple result that the spin transfer torque is approximately given by the absorption of the transverse part of the incident spin current.

This model simply illustrates one of the ideas behind Slonczewski's original model [1] for this effect. Here, a spin filter effect spatially separates the majority and minority spin currents from each other. Since the two components do not overlap, they no longer interfere with each other so that there is no transverse spin current in the outgoing states. The transverse part of the incident spin current has been absorbed by the magnetization. The mechanism for this transfer of angular momentum is the exchange interaction felt by electrons in the ferromagnet. The exchange interaction exerts a torque on the electron spins. In turn, there is a reaction torque on the magnetization.

Even though the assumptions of this simple model do not hold for realistic cases, the conclusion holds approximately for transition metal interfaces like Co/Cu [42, 43]. Two other effects contribute to its approximate validity; both are illustrated schematically in Fig. 9. In general, the reflected spins have a transverse component. However, as shown in Eq. (10), the transverse component will be rotated with respect to the incident state. It turns out that the relative phase of the reflection amplitudes varies widely over the Fermi surface, so the azimuthal rotation does as well. In fact, when the distribution of electrons carrying the current is summed over the Fermi surface, the reflected transverse spin largely cancels out and ends up close to zero. This random spin rotation is an example of classical dephasing.

The same dephasing occurs for transmitted electrons, but it is not as effective at eliminating the transverse component. However, as discussed above, the electron spins precess as they penetrate the ferromagnet [1, 50]. Electrons on different parts of the Fermi surface precess at different rates. So, while the dephasing was not complete just after transmission in to the ferromagnet, the differential precession increases the cancellation the greater the distance into the ferromagnet. For free electron models with different spherical Fermi surfaces for majority and minority electrons, the magnitude of the transverse spin current decays as one over this distance into the ferromagnet. For transition metal interfaces the transverse spin current is reduced to 10 % of its incident value after a distance of roughly 1 nm [43].

In calculations of spin transfer based on the local moment model, such as those by Heide et al. [51], the similarity of all the Fermi surfaces greatly reduces or even eliminates the mechanisms for spin transfer described above. In this model, the transverse spin current is not transferred to the magnetization at the interface, so that a transverse spin accumulation develops in the ferromagnet. This spin accumulation precesses relatively slowly around the magnetization giving a reaction torque on the magnetization. However, when scattering is included [52, 53, 54] the spin accumulation decays exponentially from the interface on a short length scale so that the transverse spin current is effectively absorbed at the interface.

Finally, it is important to note that the descriptions of spin transfer given above treat the magnetization of the ferromagnet as a classical quantity. It can be excited in arbitrarily small increments of energy and angular momentum. In fact, the excitations of the magnetization, spin waves, have a finite minimum energy and a discrete angular momentum. Urazhdin [55] shows that a quantum mechanical description of the magnetization changes the transfer dynamics. However, this model ignores the quantum mechanical aspects of the electron motion so it is difficult to determine how the changes will survive in a calculation that includes all of the quantum mechanical details.

Several groups [2, 56, 57, 51, 58] have developed a model originally proposed by Berger in which the current induced torque is due to spin-flip scattering creating a coherent excitation of the uniform spin wave. This model requires that the critical current for excitation is set by the spin accumulation (see the next section) being large enough that a spin can flip from minority to majority and excite a spin wave while conserving energy and angular momentum. Support for this model comes from the observation that experiments frequently show a critical voltage. However a critical voltage is equivalent to a critical current density. Further, Tserkovnyak et al. [59] showed that a model without direct magnon excitation can give the same critical current density.

3 Semiclassical Transport

The previous section describes how a spin current gives rise to a torque. Here we address the issue of how the spin current arises in the first place. This involves solving for the charge and spin transport throughout the whole device. The results of the previous section enter this section as boundary conditions.

Transport in magnetic multilayers occurs in three different regimes. In the most perfect samples and at low temperatures, electron transport can be quantum mechanically coherent. That is, when an electron reflects from several interfaces, the propagating wave interferes with the incident wave. This interference can then modify the transport through the structure. This type of interference is the origin of the oscillatory interlayer exchange coupling that has been extensively studied in magnetic multilayers [60]. However, even in multilayers showing interlayer exchange coupling, such effects have not been identified in the their transport properties. To a large extent, the interference features of transport get averaged out because electrons from most of the Fermi surface contribute to the transport. On the other hand, tunnel barriers can restrict the states that contribute to the transport to a small fraction of the Fermi surface. The restriction allows for the observation of interference effects on transport properties in multilayers with tunnel barriers [61, 62].

Even if the transport is not coherent, it can still be ballistic. In ballistic transport, the electrons do not scatter when they propagate from one interface to another. This limit is frequently achieved for thin layers. Finally, electrons that scatter multiple times when propagating from interface to interface are in the diffusive limit.

Most magnetic multilayers do not fall cleanly into one limit or the other. Even in a single structure, some layers may be thin enough to be in the ballistic limit while others are thicker or more disordered and in the diffusive limit. Frequently some layers are of a thickness where neither limit applies. This range of behaviors has led to a number different approaches to compute the transport properties; see Bauer et al. [63] for a discussion. Edwards et al. have treated the coherent limit [64] using the Keldysh formalism. There have been several calculations using the Boltzmann equation [53, 65] which can treat both the ballistic limit and the diffusive limit. The Boltzmann equation describes the evolution of the distribution function for states near the Fermi energy. It is based on the assumption that the distribution function can be defined locally. This assumption is consistent with ignoring quantum mechanical coherence between different parts of the device. If the layers are thin, the distribution function does not change much from one interface to the other, describing ballistic transport. On the other hand, if the layers are thick, there is a lot of scattering and the distribution function evolves diffusively. In this case many of the details of the scattering can be averaged over.

There are several approaches that can be used to derive equations of motion in which the details of the distribution are averaged over. One such approach to describe the transport through disordered bulk regions that does not depend on assuming a well defined distribution function in the disordered region is random matrix theory as used by Waintal et al. [41] Another approach is the drift-diffusion equation, which is an approximation to the Boltzmann equation that is valid in the diffusive limit [66, 9, 67]. This approach has been used extensively in the context of giant magnetoresistance where it is known as Valet-Fert theory [68]. Here the behavior of individual electron states is summed over and the theory is described in terms of currents and densities. A slightly different approach, which also sums over the behavior of individual electrons states, is the circuit theory of Brataas et al. [69]. Slonczewski has used a model that grafted circuit theory to an approximate Boltzmann equation to generate a simple analytic expression for the torque as a function of the relative angles of the magnetization [92, 70].

In each of these approaches, the behavior of the current carrying electrons as they cross interfaces is described by their transmission and reflection probabilities. In the Boltzmann equation, these probabilities enter directly into boundary conditions for the distribution functions. For the drift-diffusion equation, particular combinations of these transmission and reflection probabilities give rise to interface resistances which relate the currents across the interface to the electrochemical potential differences across them. Circuit theory is formulated in terms of interface conductances, which are slightly different combinations of the same transmission and reflection probabilities.

3.1 Boltzmann equation and drift-diffusion approximation

In this section, we describe the Boltzmann equation and how it can be manipulated to give a drift-diffusion description of the transport. In Sections 3.4 and 3.5, we describe the transport through magnetic multilayers in terms of the drift-diffusion approach. The variables in the drift-diffusion approach can be interpreted as sums over the distribution function used in the Boltzmann equation, so this description applies to most aspects of the latter approach. The connection to circuit theory is then made in Section 3.3. For a description of the same physics from the point of view of circuit theory, see [71].

The Boltzmann equation is based on the approximation that the electronic system can be described by the local occupation probability, $f_s(\mathbf{r},\mathbf{k},t)$, of well-defined bulk states of spin $s=\uparrow,\downarrow$. See Ref. [68] for the form of the Boltzmann equation and a formal reduction of it to the drift-diffusion equation. Strictly speaking, this form is only valid when the structure is slowly varying, so the bulk states can be defined. This approximation also ignores any coherence between states. In metallic systems, only the occupancies of the electrons close to the Fermi energy are changed due to transport. so it is common to linearize the distribution function

$$f_s(\mathbf{r},\mathbf{k},t) \approx f_0(\epsilon_s(\mathbf{k})) + g_s(\mathbf{r},\mathbf{k}_s^{\mathrm{F}},t) f_0'(\epsilon_s(\mathbf{k})). \tag{12}$$

where f_0 is the Fermi function, f_0' its energy derivative, and $\mathbf{k}_s^{\mathrm{F}}$ is a wave vector restricted to the Fermi surface for spin s. In the following discussion, we use the full form of the distribution function, but the idea that only the occupancies of the states near the Fermi surface vary plays an important role in describing the transport.

In a system with non-collinear magnetizations, the distribution function needs to be modified. In the non-magnet, the electron spin can point in any direction, so it is necessary to account for the coherence between the up and down spin components at each point on the Fermi surface. Thus the real distribution functions are generalized to the 2×2 Hermitian distribution matrices $f_{s,s'}(\mathbf{r},\mathbf{k},t)$. While this is a generalization of the distribution function used in the Boltzmann equation, it is a reduction of the full density matrix which includes the coherence between different parts of the Fermi surface. In the ferromagnet, this construction of a distribution matrix could not work because majority and minority spins have different Fermi surfaces. These surfaces only intersect along lines. Physically, this picture is consistent with the point made in the previous section – any transverse magnetization will rapidly dephase to zero. For a different point of view see [52, 53, 72].

To generate the drift-diffusion equation in the non-magnet, it is useful to use an equivalent formulation for the distribution matrix, which can be generated from the Pauli spin matrices

$$f_{s,s'}(\mathbf{r},\mathbf{k},t) = f(\mathbf{r},\mathbf{k},t)\delta_{s,s'} + \sum_{\alpha=x,y,z} f_\alpha(\mathbf{r},\mathbf{k},t)[\sigma_\alpha]_{s,s'}, \tag{13}$$

where σ_α is a Pauli spin matrix. The Boltzmann equation describes the evolution of f and can be written in terms of either form. The drift-diffusion equation is generated by taking moments of the Boltzmann equation and ignoring some of the details near interfaces. Its basic variables are moments of the distribution function. In the normal metal, these are the change in density δn, the number current $\mathbf{j}$, the spin accumulation $\mathbf{s}$, and the spin current $\mathbf{Q}$

$$\begin{aligned} n_0 + \delta n &= \sum_{\mathbf{k}} f(\mathbf{k}) & j_\beta &= \sum_{\mathbf{k}} f(\mathbf{k}) v_\beta(\mathbf{k}) \\ s_\alpha &= \frac{\hbar}{2}\sum_{\mathbf{k}} f_\alpha(\mathbf{k}) & Q_{\alpha\beta} &= \frac{\hbar}{2}\sum_{\mathbf{k}} f_\alpha(\mathbf{k}) v_\beta(\mathbf{k}) \end{aligned} \tag{14}$$

where v_β is a component of the velocity of the state at $\mathbf{k}$, and n_0 is the equilibrium density. The spin-independent moment of the Boltzmann equation gives the drift-diffusion equation in the non-magnet

$$j_\beta = (\sigma/e)E_\beta - D\nabla_\beta \delta n. \tag{15}$$

The first term is the drift term, with conductivity σ, and the second is the diffusion term, with diffusion constant D. An equivalent formulation is to use the density of states $(\partial n/\partial\mu)$ to write the number accumulation as a chemical potential $\mu = \delta n/(\partial n/\partial\mu)$. Then, using the Einstein relation, $e^2\sigma = D\partial n/\partial\mu$, the effect of both the local electric field and the diffusion of the charge accumulation is captured by the local electrochemical potential, $j_\beta = -(\sigma/e)\nabla_\beta(\mu + V)$. In fact, a local excess charge $-e\delta n$ creates a local electric field so that E and δn are related through Poisson's equation. However, only the electrochemical potential $\mu + V$ couples to the transport so it is not necessary to actually solve Poisson's equation and determine the charge accumulation and the electric field separately.

The spin moments of the Boltzmann equation give

$$Q_{\alpha\beta} = -D\nabla_\beta s_\alpha. \tag{16}$$

This expression simply states that for non-magnets in the diffusive limit, any spin current is due to the diffusion of a spatially inhomogeneous spin accumulation. In this equation, the spin current is given by the gradient of the spin accumulation. In the spin continuity equation, Eq. (7), for time-independent magnetization, the gradient of the spin current is proportional to the spin accumulation. Combining these two equations gives a diffusion equation that has exponential solutions characterized by the spin diffusion length $l_{\mathrm{sf}} = \sqrt{D\tau_{\mathrm{sf}}}$. This is the length scale over which a steady state spin accumulation decays to zero, the mean distance a spin diffuses before it flips. The spin accumulation is frequently written as a spin chemical potential, $(\hbar/2)\Delta\mu_\alpha = s_\alpha/(\partial n/\partial\mu)$.

In the bulk, the two are equivalent. At the interface between two materials with different chemical potentials, either formulation can be used, but the differences in the chemical potentials across the interface are directly related to the current and the spin currents.

In ferromagnetic materials, it is most natural to adopt the two-current formulation of the Boltzmann equation as done by Valet and Fert [68] provided all of the ferromagnet magnetizations are collinear. The majority and minority electrons are treated as two different species so that the variables in the drift-diffusion equation are

$$n_{s0} + \delta n_s = \sum_{\mathbf{k}} f_s(\mathbf{k}) \qquad j_{s\beta} = \sum_{\mathbf{k}} f_s(\mathbf{k}_s) v_\beta(\mathbf{k}), \tag{17}$$

where n_{s0} is the equilibrium spin density for each spin direction. The drift-diffusion equations are then

$$\mathbf{j}_s = (\sigma_s/e)\mathbf{E} - D_s \boldsymbol{\nabla} \delta n_s. \tag{18}$$

The sum and the difference of the equations for the two spins give the equations for the total current and the spin current respectively. The relative size of the conductivities for each spin, $\sigma_\uparrow$ and $\sigma_\downarrow$ is complicated. The ratio depends on the relative density of states, the effective velocities of the states and the scattering rates. In Co, the material principally discussed in this chapter, the differences in the scattering rates dominate giving a higher conductivity for majority electrons.

If the magnetization is uniform within each layer, the two current model can be used with appropriate boundary conditions. If the magnetization within a layer is is not uniform, the model needs to be generalized to treat a spatially varying magnetization direction. The simplest approach, which we will adopt, is to assume that the direction of the ferromagnetic spin density $\hat{\mathbf{u}}$ (opposite the magnetization) is sufficiently slowly varying that the spin direction of the spin current and the accumulated spin adiabatically follow the magnetization direction [73, 74]. In this case, the spin current is simply $(\hbar/2)\hat{\mathbf{u}} \otimes (\mathbf{j}_\uparrow - \mathbf{j}_\downarrow)$. When this form is inserted into the continuity equation, Eq. (7), it is clear that a polarized current flowing through a spatially varying magnetization direction gives rise to a torque. There is presently a large body of research on this topic [75], building on the original work by Berger [76]

As the interfaces play important roles in typical spin-transfer structures, so do the boundary conditions. The longitudinal boundary conditions are most simply written in terms of spin-dependent electrochemical potentials, rather than number and spin accumulations. Working in the frame of reference of the magnetization, the longitudinal current for each spin is conserved across the interface (ignoring spin-flip scattering localized to the interface) and is proportional to the difference in the electrochemical potentials across the interface

$$R_s \mathbf{j}_s \cdot \hat{\mathbf{n}} = \mu_s^{\mathrm{NM}} - \mu_s^{\mathrm{FM}}, \tag{19}$$

where $\hat{\mathbf{n}}$ is the interface normal pointing from the non-magnet into the ferromagnet. The spin dependent interface resistance R_s is determined by an appropriate sum over the transmission and reflection probabilities for individual states.

In the previous section, we argued that there is no transverse spin accumulation or spin current in the ferromagnet. In this case, the transverse spin current and spin accumulation in the non-magnet must be proportional to each other

$$\mathbf{Q}_{\perp} \cdot \hat{\mathbf{n}} = B\mathbf{s}_{\perp}. \tag{20}$$

B is the constant of proportionality and is defined in Eq. (22). The $\perp$ subscript indicates the transverse component. This boundary condition is actually simple to understand given that transverse spin currents get absorbed at the interface. If there is an accumulation of transverse spins, they diffuse in all directions. However, if they are absorbed at the interface there is no backflow of transverse spins giving a net transverse spin current toward the interface. This form can be derived by detailed consideration of the boundary conditions in the Boltzmann equation. The boundary conditions, Eqs. (19) and (20) are used in calculations of the spin transport through an interface in Appendix A. If the magnetization is time dependent, there is another term in this boundary condition due to spin pumping.

3.2 Spin pumping

Spin pumping, an effect originally proposed by Berger [2] and developed by Tserkovnyak et al. [77, 78], comes from the spin-dependence of the reflection amplitudes. The presence of the ferromagnet induces in the non-magnetic layer a small, decaying, oscillatory magnetization, which is closely related to the Friedel oscillations in the charge density near a surface. This magnetization arises from the partial reflection of electrons as they scatter from the interface. The incoming and outgoing components of the electron states interfere with each other. Each such state gives rise to an oscillatory density in the non-magnet. This density oscillation is also a spin density oscillation because the reflection amplitudes are spin-dependent. Summing over all electron states gives rise to a net induced spin density that decays into the non-magnet.

When the magnetization in the ferromagnet rotates, the induced magnetization rotates as well. Since the change in the induced magnetization is driven by the rotating magnetization in the ferromagnet, it must arise from spin currents "pumped" through the interface between the two materials. Since the spin density that rotates is a superposition of contributions from electron states at all energies below the Fermi energy, the spin current is carried by all of the electrons, not just those at the Fermi level. The perturbation to the electronic system, the rotating magnetization, is time dependent, so it allows for inelastic scattering. However, for the states well below the Fermi energy, all of the states are occupied and there is no possibility for energy transfer. Thus, the spin current carried by the electrons with energies well below the Fermi level is *reversible*. That is, if the magnetization returns to its initial configuration, no energy (or net spin current) has been transferred to the electronic states in the non-magnet. However, near the Fermi energy, electrons that interact with the rotating magnetization can be scattered from just below the Fermi energy to just above it. This inelastic scattering means that the component of the spin current which is carried by the electrons with energies near the Fermi energy is *irreversible*, that is, when the magnetization returns to its original configuration, there has been a net flow of energy (and spin current) into the non-magnet. These two components of the spin current, reversible and irreversible, are conceptually related to the real and imaginary parts of frequency-dependent susceptibilities.

While the idea that energy is transferred from the magnetic system into the electronic system of the non-magnet is relatively straightforward, it is not so obvious that angular momentum is also transferred. However, lowering the energy of the magnetic system requires increasing the alignment of the magnetization with the instantaneous internal field direction. Since the absolute magnitude of the magnetization is largely fixed, increasing the alignment of the magnetization with its internal field is equivalent to rotating the magnetization in a direction that is perpendicular both to the magnetization direction $\hat{\mathbf{u}}$ and to the direction in which the magnetization is precessing $\dot{\hat{\mathbf{u}}}$. The change in magnetization in the ferromagnet is pumped into the non-magnet through a spin current. Thus the boundary condition becomes

$$\mathbf{Q}_{\perp} \cdot \hat{\mathbf{n}} = B\mathbf{s}_{\perp} + B'\hat{\mathbf{u}} \times \dot{\hat{\mathbf{u}}}. \tag{21}$$

Since the spin pumping term has exactly the same form as Gilbert damping, it acts as an additional source of damping that is effective at the interfaces. This hand-waving argument for Eq. (21) is confirmed by calculations using several different approaches for different models of the electronic structure [77, 79, 80].

These same calculations further show that in the approximation that the transverse spin current is absorbed at the interfaces, the coefficients in Eq. (21) are simply related to the projected area of the Fermi surface in the non-metal A_{FS}

$$B' = \frac{A_{\mathrm{FS}}}{(2\pi)^3}\frac{\hbar}{2} = \frac{\hbar^2}{2}\frac{\partial n}{\partial \mu}B \tag{22}$$

This contribution to the damping has been studied extensively in ferromagnetic resonance [81, 82, 83, 84, 85, 86]. The measured behavior of the resonance linewidth as a function of layer thicknesses and frequency quantitatively confirms that spin pumping acts as an additional source of damping. Note that the pumped spin current only functions as an additional source of damping if it does not return to the precessing ferromagnet. Thus the angular momentum carried by the spin current needs to be absorbed by spin flip scattering in the bulk, or by scattering from another ferromagnetic layer with a non-collinear magnetization.

3.3 Circuit theory

The circuit theory of Brataas et al. [69, 71] is based on the approximation that devices can be divided into nodes and regions that connect them. In the nodes, the voltages (chemical potentials), and spin accumulation are assumed to be spatially uniform. The nodes are connected by conducting channels, across which the chemical potential differences drive charge and spin currents. The conductances of the channels are determined by the same transmission and reflection probabilities that enter as boundary conditions in the Boltzmann equation or determine the interface resistances in the drift-diffusion approximation. Since the spin accumulation in a non-magnetic node need not be collinear with the magnetization direction in a ferromagnetic node, describing the transport requires both the conductances for majority $g_\uparrow$ and minority $g_\downarrow$ electrons

$$g_\sigma = \frac{e^2}{h} \sum_{n\in\mathrm{NM}} \sum_{m\in\mathrm{FM}} |t_\sigma^{nm}|^2 \,, \tag{23}$$

as well as the "mixing conductance"

$$g_{\uparrow\downarrow} = \frac{e^2}{h} \sum_{n\in\mathrm{NM}} \left[1 - \sum_{m\in\mathrm{NM}} r_\uparrow^{nm} \left(r_\downarrow^{nm} \right)^* \right] . \tag{24}$$

The majority and minority conductances describe electrons going from one material into another and hence involve sums over channels in both materials. The mixing conductance on the other hand, describes a spin current that is absorbed by the ferromagnet. Thus, it only depends on a sum over channels in the non-magnet. The mixing conductance describes the behavior of spins in the non-magnet that are perpendicular to the magnetization in the ferromagnet. The real part gives the spin current that is aligned with the perpendicular part of the chemical potential. The imaginary part gives the spin current that is perpendicular both to the magnetization and to the chemical potential in the non-magnet. Both of these components are absorbed at the interface giving rise to a torque on the magnetization. As described in the previous section, the sum over the reflection amplitudes goes to zero because of spin filtering and dephasing. Thus, in transition metal systems the real part of the mixing conductance is roughly proportional to the number of conducting channels and the imaginary part is close to zero.

Circuit theory differs from the drift-diffusion approach in two ways. First, it is formulated in terms of conductances rather than resistances. This difference is minor, because the drift diffusion approach could be as well. The larger difference is the neglect of the spatial dependence of the chemical potential within the layers (nodes in the language of circuit theory). This approximation works well in devices in which the total resistance is dominated by the interface resistances. However, in devices that are beyond this limit, it is possible to augment circuit theory with a drift-diffusion calculation within a layer. Thus, the differences between the two approaches are largely conceptual.

Circuit theory does not naturally apply to structures where the chemical potentials vary in space, although it can be generalized to treat such systems. The real strength of circuit theory is that it is quite straightforward to treat complicated structures in which more than two ferromagnetic regions are attached to a non-magnetic node. The proposed spin-torque transistor of Brataas et al. is an example [69]. The Boltzmann equation and drift-diffusion approaches can also treat such cases, but solving the equations for geometries that are not essentially one dimensional is much more difficult, see Sec. 3.6.

3.4 Collinear Transport

The transport equations and boundary conditions of the previous section allow us to determine the current flow through magnetic multilayers. It is useful to consider the transport through magnetic multilayers in terms of simpler components of the structure, starting with a single interface. Early theoretical studies of the behavior of spin currents and accumulation at interfaces have been made by Aronov [87], Johnson and Silsbee [88], van Son et al. [89], and Valet and Fert [68]. Fig. 10 illustrates the spin current and the spin accumulation for electrons flowing into a ferromagnet from a non-magnet and the reverse. Much of the history of this topic is reviewed in [90]. Far away from the interface in either material, the spin current just depends on the spin dependence of the conductivity. In the non-magnet, the conductivity is unpolarized, so there are an equal number of majority and minority spins flowing. In the ferromagnet on the other hand, the conductivity is spin-dependent, and there is a finite spin current. For the case of electrons flowing from the non-magnet on the left, there are equal number of majority and minority electrons flowing toward the interface, but more majority electrons flowing away from it. This imbalance leads to accumulation of minority spins near the interface. These minority spins diffuse away from the interface into both materials. A diffusion of minority spins away from the interface in the $-\hat{\mathbf{z}}$ direction in the non-magnet gives rise to a positive spin current. On the other hand, the diffusion of minority spins in the $\hat{\mathbf{z}}$ direction into the ferromagnet gives a negative correction to the spin current flowing into the bulk. Interestingly, the diffusion of minority spins away from the interface means that the current in the non-magnet is spin polarized before it enters the ferromagnet.

The system reaches a steady state because of spin-flip scattering. As more non-equilibrium spins accumulate, they relax faster toward equilibrium. Eventually, the change in the magnetization due to spin-flip scattering exactly cancels the net arrival of excess spins. The length scale over which the spin current recovers its bulk values is the spin diffusion length. Here the spin diffusion length is shorter in the ferromagnet than the non-magnet. Spin-flip scattering is a result of the coupling of the electrons to the lattice and so serves

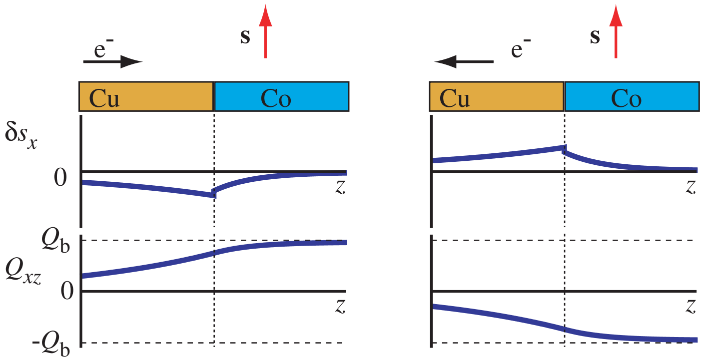

Fig. 10. Spin accumulation (δs_x) and spin current (Q_{xz}) for electron flow from a non-magnet into a ferromagnet (left side) and vice versa (right side). Q_b is the magnitude of the spin current in the bulk ferromagnet far from any interfaces due to the spin dependent conductivity. The magnetization in the ferromagnet, $\mathbf{M}$ is along the $-\hat{\mathbf{x}}$-direction so that the ferromagnetic spin density $\mathbf{s}$ is along the $\hat{\mathbf{x}}$-direction.

as a source of angular momentum in the electron subsystem. The electrons in the non magnet carry no angular momentum into the interface region, but the electrons in the ferromagnet carry some away. Spin flip scattering allows for this apparent non-conservation. The change in the spin-dependent conductivities in the structure plus the spin flip scattering leads to a transfer of angular momentum from the lattice into the flowing electrons.

There is a discontinuity in the spin chemical potential (spin accumulation) across the interface because the interface resistance is spin-dependent. To see the origin of the discontinuity, note that whenever the polarization of the current, P (see Eq. (3)), is different than the polarization of the *bulk* conductivity $P_\sigma = (\sigma_\uparrow - \sigma_\downarrow)/(\sigma_\uparrow + \sigma_\downarrow)$, there must be a gradient in the spin accumulation to provide a diffusive component. Similarly, whenever the polarization of the current is different than the polarization of the *interface* conductivity $P_\Sigma = (\Sigma_\uparrow - \Sigma_\downarrow)/(\Sigma_\uparrow + \Sigma_\downarrow)$, there must be a discontinuity in the spin chemical potential. On the other hand, the spin current is constant across the interface because there is no spin flip scattering localized to the interface (in this model).

The detailed forms of the currents and densities in Fig. 10 are found from the bulk solutions in the leads and the matching conditions at the interface. The details are given in Appendix A.

In the right side set of panels in Fig. 10, we see that for current flowing in the opposite direction, more majority electrons flow into the interface region than flow out, so there is an accumulation of majority spins near the interface, changing the sign of the spin accumulation. These majority electrons diffuse away from the interface changing the sign of the spin current.

The behavior of a current flowing through a finite thickness ferromagnetic layer embedded in a non-magnet can roughly be constructed by superposing the accumulation and spin current for single interfaces. The result is shown in Fig. 11. An equal number of majority and minority electrons flow into and out of the region near the interface, but more majority electrons flow through the ferromagnet. This leads to an accumulation of minority electrons before the ferromagnetic layer and an accumulation of majority electrons after the layer. These diffuse away from the interface giving rise to a current that is equally spin polarized before and after the layer. For this system, angular momentum is coupled into the electron system from the lattice in the left lead, is carried through the ferromagnetic layer and deposited in the lattice in the right lead.

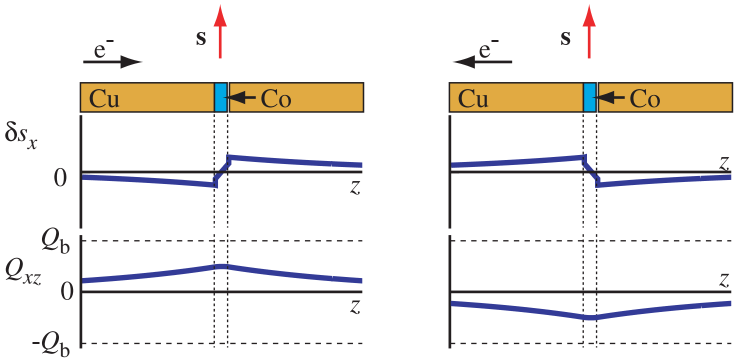

Fig. 11. Spin accumulation (δs_x) and spin current (Q_{xz}) for electron flow through a ferromagnetic layer embedded in a non-magnetic host. The current flow is in the positive $\hat{\mathbf{z}}$ direction on the left hand side and in the negative direction on the right. Q_b is the magnitude of the spin current in the bulk ferromagnet far from any interfaces due to the spin dependent conductivity. The ferromagnetic spin density in the ferromagnet, $\mathbf{M}$ is along the $-\hat{\mathbf{x}}$-direction so that the ferromagnetic spin density $\mathbf{s}$ is along the $\hat{\mathbf{x}}$-direction.

The spin current and spin accumulation for two ferromagnetic layers with a thin spacer layer can be seen as a superposition of the values for two single layers provided the two magnetizations are collinear with each other. Figure 12 illustrates this superposition for the cases of parallel and antiparallel alignment of the magnetizations. The case of parallel alignment looks very much like a single ferromagnetic layer. There is accumulation of minority spins before the layers, majority spins after the layers, and almost none in the spacer layer. A substantial spin current flows through the whole trilayer. The case of antiparallel alignment is just the opposite. There is almost no spin current and almost no spin accumulation in the leads. There is a large majority spin accumulation in the spacer layer. The spacer layer spin accumulation is a combination of majority spin accumulation after the first layer and minority (with respect to the reversed magnetization) accumulation before the second layer. This spatially varying spin accumulation provides the diffusive contribution necessary to cancel the natural bulk spin current in each ferromagnetic layer, Q_b.

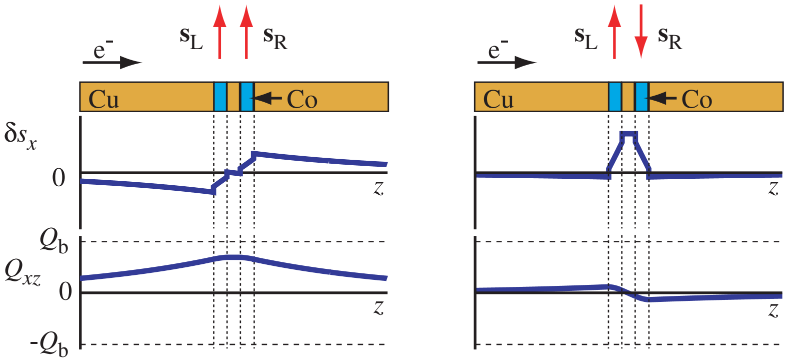

Fig. 12. Spin accumulation (δs_x) and spin current (Q_{xz}) for electron flow through two ferromagnetic layers embedded in a non-magnetic host and separated by a thin non-magnetic spacer layer. The magnetizations of the two layers are parallel along the $\hat{\mathbf{x}}$ direction on the left side and antiparallel on the right. Q_b is the magnitude of the spin current in the bulk ferromagnet far from any interfaces due to the spin dependent conductivity.

The difference in the spin current between the cases of parallel and antiparallel alignment is the origin of the giant magnetoresistance. In the case of parallel alignment, more of the current flows through the lower resistance majority channel, lowering the average resistance of the multilayer.

One of the important points of this section is that the polarization of the current and the spin polarization are not local properties. They depend on everything in the device within a few spin diffusion lengths in both directions. In Section 2, we showed that the torque depends on the transverse spin current. The arguments in this section show that the spin current depends on the properties of the whole device, not simply the materials in the immediate vicinity of the interface. Finding the torque will also require solving for the transport throughout the whole device.

3.5 Non-Collinear Transport and Torque

When the magnetizations of the two layers are not collinear, the direction of the spin accumulation and spin direction of the spin current, see Eq. (3), vary throughout the structure. Still, the transport can be understood in very much the same terms as the transport for collinear magnetizations with the addition of the absorption of the transverse component of the spin current at the interfaces. For example, consider the spins along $\hat{\mathbf{x}}$, collinear with the magnetization of the left layer, see Fig. 13. More majority electrons go through the layer, so there is an accumulation of minority electrons in the left lead. The majority electrons going through the layer go through the thin spacer relatively unchanged. However, when they reach the interface with the right ferromagnet, they are transverse and the transverse spin current goes to zero inside the ferromagnet. This gives a torque on the right ferromagnet that tends to rotate it into parallel alignment with the left ferromagnet. Note that while it is more natural to have the spins lie in the y-z plane, it is more difficult to illustrate in a figure. For this reason, we have chosen to have the magnetizations and spins lie in the x-z plane. Now consider the spins polarized along the $\hat{\mathbf{z}}$-direction, parallel to the right magnetization. When the transverse spin current hits the right ferromagnet and gets absorbed, primarily minority electrons get reflected and majority get transmitted, giving a positive spin current for a spin direction along $\hat{\mathbf{z}}$. The reflected minority electrons diffuse back to the interface with the left ferromagnet (note that minority electrons diffusing backwards also give a positive spin current along $\hat{\mathbf{z}}$), where they are transverse to the magnetization and get absorbed. Here, the absorption of the transverse spin current gives a torque that tends to rotate the left magnetization to be antiparallel to the right magnetization. The directions of the spin currents can be difficult to visualize from these graphs, so a cartoon of the spin currents is given at the bottom.

The torques described above tend to make the magnetizations “pinwheel” after each other rather than rotate toward or away from each other or even precess around each other. This apparent violation of the conservation of angular momentum derives from the fact that angular momentum is being provided by the coupling to the lattice through spin-flip scattering. The angular momentum coupled into the right magnetization comes from the lattice in the left lead and the magnetization coupled into the left ferromagnet comes from the right lead. As can be seen from the right side panels of Fig. 13, the current direction determines the direction of the pinwheeling. In most systems of experimental interest, in which the magnetization of one of the layers is held fixed, electrons flowing from the fixed layer into the other layer tend to bring the second layer magnetization into alignment with that of the fixed layer and electron flow from the second layer into the fixed layer tends to anti-align the magnetization of the second layer with that of the fixed layer.

The calculation illustrated in Fig. 13 can be repeated as a function of the angle between the magnetizations. This calculation gives two results: the torque as a function of angle and the magnetoresistance as a function of angle. Both have been studied by a number of authors [91, 92, 65, 93, 94, 95, 70]. The torque per unit area has the form

$$\frac{\mathbf{N}_{\mathrm{c}}}{A} = \frac{\hbar}{2}(\mathbf{j}\cdot\hat{\mathbf{z}})\ \mathcal{P}\ \left[\hat{\mathbf{s}}\times(\hat{\mathbf{s}}_0\times\hat{\mathbf{s}})\right], \tag{25}$$

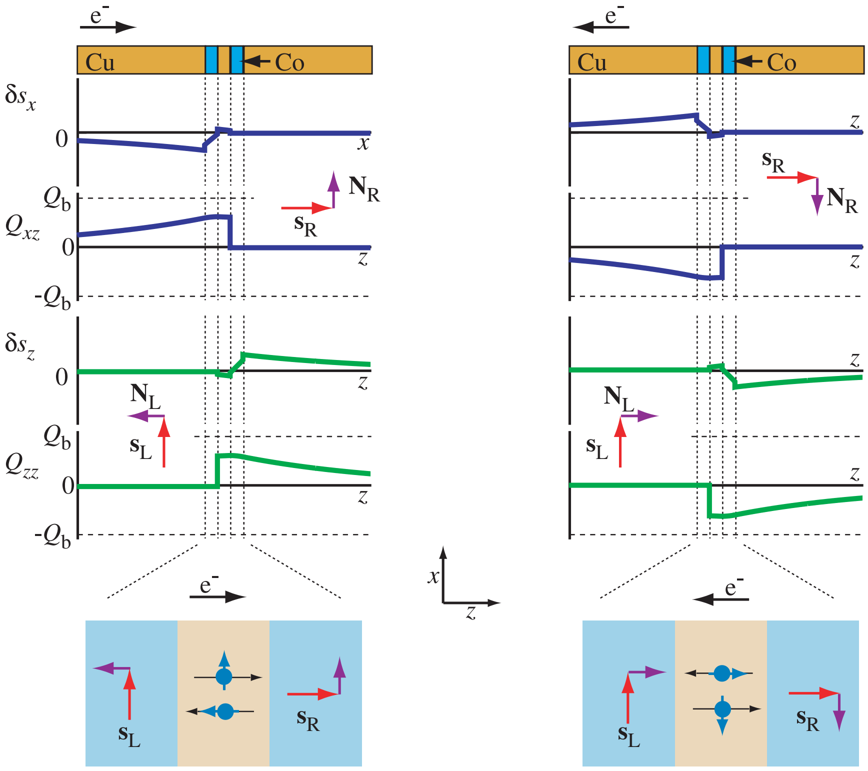

Fig. 13. Spin accumulation (δs_x and δs_z) and spin current (Q_{xz} and Q_{zz}) for electron flow through two ferromagnetic layers embedded in a non-magnetic host and separated by a thin non-magnetic spacer layer. The magnetizations of the two layers are perpendicular to each other, for purposes of illustration both are in the plane of the figure. On the left side the current flows in the $\hat{\mathbf{z}}$ direction and on the right in the $-\hat{\mathbf{z}}$ direction. Q_{b} is the magnitude of the spin current in the bulk ferromagnet far from any interfaces. The transverse component of the spin current is discontinuous at each interior interface giving rise to torques on the magnetizations of each layer. The directions of the torques are indicated for each of the interfaces. The bottom panel gives a cartoon of the spin current in the spacer layer. The blue arrows give the direction of the electron spins for electrons moving in the directions given by the black arrows (recall that the spin current for an electron with a spin in one direction moving to the left is the same as the spin current from an oppositely directed spin moving to the right). The purple arrows repeat the torques from above.

where $\hat{\mathbf{s}}$ and $\hat{\mathbf{s}}_0$ are the free and fixed layer ferromagnetic spin density directions respectively. If the spin current reaching the free layer were independent of the of the relative orientation of these directions, $\mathcal{P}$ would be a constant. The double cross product is the part of $\hat{\mathbf{s}}_0$ that is transverse to $\hat{\mathbf{s}}$, i.e. $\hat{\mathbf{s}}_0 - (\hat{\mathbf{s}}_0 \cdot \hat{\mathbf{s}})\hat{\mathbf{s}}$. This equation is simply the absorption of the transverse spin current, which has been assumed to be fixed. This form has been used in a number of micromagnetic simulations for the torque. However, one of the main points of this section is that the spin current is *not* independent of the relative orientations of the two magnetizations. The dependence of the spin current on the orientations of the magnetization has a substantial effect on the torque as seen in Fig. 14.

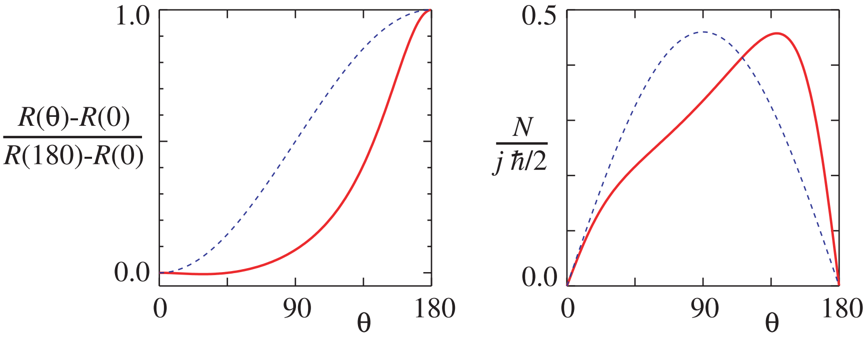

Fig. 14. The angular dependence of the torque and magnetoresistance as a function of the relative angle of the two magnetizations. The blue curves show the simple forms frequently used in micromagnetic simulations, $\sin^2(\theta/2)$ and $\mathcal{P}_0 \sin\theta$ for the relative magnetoresistance and the torque respectively. Here $\mathcal{P}_0$ is a constant

In general, it is necessary to solve a transport equation (Boltzmann, drift-diffusion, circuit theory) to compute the angular dependence of the torque. However, Slonczewski [92] has derived an analytic formula based on a calculation that combines a density matrix description of the spacer layer with a circuit theory [69] description of the remainder of the structure. This formula has been extended by several authors [96, 70, 97, 95]. Xiao et al. [70] have tested it by comparing it with the results of calculations using the Boltzmann equation. In general, the torque is given by Eq. (25) with

$$\mathcal{P} = \left[\frac{q_+}{B_0 + B_1 \cos\theta} + \frac{q_-}{B_0 - B_1 \cos\theta} \right] \tag{26}$$

where $\cos\theta = \hat{\mathbf{s}}_0 \cdot \hat{\mathbf{s}}$. The parameters B_0, B_1, q_+, and q_- depend on the geometry of the device and the physical properties of the layers and interfaces. In particular, they depend on effective spin-dependent resistances from the spacer layer in each direction over a cumulative spin diffusion length. A similar expression can be written for the angular dependence of the magnetoresistance

[95]. Fits to the curves in Fig. 14 with these formulae are indistinguishable from the full calculations.

Calculated values of q_-/q_+ and B_1/B_0 capture some of the important results of the various transport calculations that have been done. The ratio q_-/q_+ depends on the asymmetry of the structure. If the device is symmetric, the ratio goes to zero, giving the limit originally derived by Slonczewski [92]. Calculations show that this ratio becomes important when lead lengths become comparable to spin diffusion lengths, a situation not normally found in actual devices. The ratio B_1/B_0 describes the asymmetry of the slope of the torque between angles close to parallel and those close to antiparallel. All transport calculations find a substantial asymmetry. The ratio only becomes small when the spin current scattering from the free layer is independent of the direction of the free layer magnetization. This current is only independent of the free magnetization direction when the effective resistances approach the Sharvin resistance. Unfortunately, the torque vanishes in this limit. For some geometries, there are simple analytic formulas for the various parameters [92, 96, 70, 97, 95].

All transport calculations done to date give results consistent with Eq. (26). However, there is only limited experimental confirmation of this form. In most cases there is enough uncertainty about important aspects of the samples, as indicated by large sample-to-sample variation, that it is difficult to make a compelling test of the angular dependence of the torque. However, Smith et al. [98] have recently shown that critical currents they measured are best described when the angular dependence of the polarization and hence torque is described as in the first term of Eq. (26). For samples with short leads, q_- and hence the second term in that equation is generally negligible. There have been a few tests of the angular dependence of the magnetoresistance [99, 100]. These show clear deviation from simple $\sin^2(\theta/2)$ behavior, but less deviation than would be expected from the theories that lead to Eq. (26).

The spin-transfer torque is effective near the interface. In most simulations that treat the torque, the practitioners assume that the ferromagnetic layer is thin enough that the magnetization is constant throughout the thickness of the layer and so treat the spin transfer torque as spread out through the layer. In fact, it is an interfacial torque and needs to be balanced by another interfacial torque. In micromagnetic calculations, interfacial exchange torque is zero when the normal derivative of the magnetization is zero $(\hat{\mathbf{n}}\cdot\boldsymbol{\nabla})\mathbf{s}(\mathbf{r}) = 0$. In the presence of an interfacial spin transfer torque, this normal derivative becomes non-zero so that the exchange interaction gives rise to an interfacial torque that compensates the spin transfer torque. The finite derivative at the interface means that the magnetization direction is spatially varying as a function of position in the ferromagnet. The spatially varying magnetization is subject to an exchange torque that effectively spreads out the interfacial spin transfer torque. In other words, even though the spin transfer torque is an interfacial torque, the spin transfer torque plus the exchange interaction together act as though the spin transfer torque is uniformly spread out over layers provided those layers are thin enough.

These balancing torques have an interesting physical understanding. Recall from Section 2 that the micromagnetic exchange torque can be written as a divergence of a spin current that is carried by all of the electrons. In the non-magnet, the spin current is carried by the non-equilibrium electrons at the Fermi surface. In the ferromagnet, there is no transverse spin current, but there is an exchange torque, which is a spin current carried by all of the electrons. At the interface, these two spin currents are converted into each other.

3.6 Leads/reservoirs

The entire preceding discussion was based on a one dimensional approximation for the transport. However, as can be seen in Fig. 1, this is far from the actual situation. Possibly the most important difference is that leads become very wide close to the sample. In fact, this widening is important experimentally to remove the heat generated by the large current densities through the sample.

The simplest treatment of the leads is to treat them as reservoirs. In this context, a reservoir has an infinite density of states, so that the spin chemical potential is zero. This boundary condition is natural in circuit theory and is readily implemented into a drift-diffusion approach. In both of these approximations, the incoming and outgoing electrons are lumped together into a single spin density and a single spin current. In a Boltzmann equation, it is more complicated and the equivalent boundary condition is harder to implement. In this case, the boundary conditions is that the electrons leaving the reservoir must have a bulk-like distribution, but the electrons entering the reservoir can be in whatever state is dictated by the sample. This implementation can give very different results from the drift diffusion approach.

Even more meaningful results are given by calculations of the transport that treat all three dimensions [101, 102]. These calculations show that accounting for the geometry is important and not as simple as is assumed in treating them as reservoirs. These papers show that the variation of the spin chemical potential in the transition region is quite important. This can be understood from the argument that the effective width of the lead does not go abruptly from small to large, but rather the current spreads out into the leads. These calculations imply that care should be taken in interpreting any one dimensional calculations for which the results depend sensitively on the length of the leads.

3.7 Lateral Inhomogeneity

If the magnetization in the interface is not uniform, diffusion of spins parallel to the interface will lead to spin-transfer torques [103, 67]. Consider the case of electron flow from the non-magnet into the ferromagnet. The electrons that are reflected into the non-magnet and which accumulate there, are *on average* antiparallel to the magnetization direction.

If the magnetization is uniform across the interface, the accumulated spins are aligned. On average, these electrons diffuse away from the interface, but since their motion is diffusive, there is a significant probability that they return and scatter from the interface in a different location. One such trajectory is illustrated in Fig. 15. The Fermi velocity of the electrons is sufficiently high that the magnetization does not significantly rotate when the electron scatters from the interface. Even if the electron diffuses laterally, it is still antiparallel to the magnetization when it scatters from the interface.

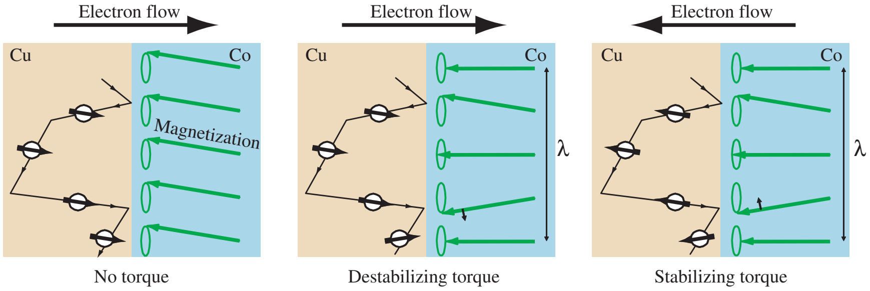

Fig. 15. Spin transfer torque due to lateral diffusion. Each panel shows an electron diffusing in a non-magnet and reflecting twice from the interface with a ferromagnet. After it scatters, it is oriented *on average* either parallel or antiparallel to the magnetization depending on the direction of the electron flow, see Fig. 10. In the first panel, the ferromagnetic magnetization is uniform laterally so that when the electron scatters the second time, it is aligned with the magnetization and there is no reorientation of either. The electron flow is from the non-magnet into the ferromagnet, so the accumulated spins are minority spins. In the second panel, there is a non-uniform magnetization, and the diffusing minority spin is not aligned with the magnetization the second time it scatters. The magnetization exerts a torque on it and it exerts a torque on the magnetization which tends to amplify the spin wave. In the third panel, the electron flow is in the opposite direction so the diffusing spins are majority spins. In this case, the torque in the second scattering event tends to reduce the amplitude of the non-uniform spin wave.

If, on the other hand, the magnetization varies slowly across the interface, the electron spins locally are antiparallel to the local magnetization direction after they reflect. When they diffuse laterally, they are no longer antiparallel to the local magnetization direction when they rescatter from the interface. Since they tend to be antiparallel to the average magnetization after they scatter, they are rotated by this scattering event, exerting a reaction torque on the ferromagnet.

When the net electron flow is from the non-magnet into the ferromagnet, this lateral diffusion and rescattering tends to amplify deviations away from the average magnetization direction. On the other hand, when the electron flow is from the ferromagnet into the non-magnet, the diffusing spins are now parallel to the magnetization on average, and the torque due to rescattering tends to suppress fluctuations away from the average direction.

Polianski and Brouwer [103] and Stiles et al. [67] have shown that these torques can be large enough to lead to instabilities in the magnetization of single thin films or single interfaces when the current is large enough. For a single interface, the instability only occurs for one direction of current flow. For finite thickness ferromagnetic layers embedded in a non-magnetic host, the lateral diffusion at one interface is destabilizing, but that at the other interface is stabilizing. Instabilities therefore require an asymmetry in the system either the details of the leads or a non-uniform (along the current direction) response in the ferromagnet. Point contact experiments by Ji et al. [14] and Chen et al. [38] and single film nanopillar experiments by Özyilmaz et al. [39] both show instabilities that are at least qualitatively similar to what is expected from the models.

4 Micromagnetics

Ideally, the models described in the previous sections could be tested directly. Unfortunately the probes available to investigate these systems are rather limited. Generally, only the current and voltage through the structure are measured. This provides a check on the transport calculations, but the test is stringent only when enough of the system parameters are known accurately, which is not generally the case. The torque cannot be directly investigated at all. Only the resulting behavior of the magnetization can be inferred from measurements of the resistance. However, the behavior can be measured as a function of current, applied field, and the geometry of the device. The agreement between calculations and measurements can be quite compelling, albeit not without a few free parameters. In this section we describe the tools used to model the magnetization dynamics and give some results found for these systems.

We start this section with a consideration of the geometry of the devices of interest and their static energetics. Then, we introduce the equation of motion that describes the dynamics of the system – the Landau-Lifshitz-Gilbert equation (see e.g. [105]). Before considering the full dynamics of the system that results from this equation, we consider the macrospin approximation, a simple limit that illustrates much of the essential physics. In this approximation, the magnetization of the layer undergoing dynamical evolution is considered to remain uniform throughout its motion. This approximation illustrates the way in which these systems exhibit precessional instability for large enough current flows. Further, it allows analytic determination of the regimes of stability of different states. After determination of the zero temperature “phase diagram” of such systems, we consider the effect of temperature on the dynamics through the introduction of thermally driven fluctuating fields into the equation of motion and finish with some examples of full micromagnetic simulations.

4.1 Geometry and Energetics

A typical GMR pillar geometry for the study of spin transfer effects is sketched in Fig. 16. It contains a soft thin layer (the top layer in Fig. 16) and a thick, ideally hard, uniformly magnetized layer, often referred to as the fixed or reference layer (bottom layer in Fig. 16). Most authors assume the current density J to be positive for electrons flowing along the $-\mathbf{z}$ direction. Under steady current, the soft, thin layer is thus flooded with electrons that become spin polarized through transmission across (reflection from) the thick layer for $J < 0$ ($J > 0$). Without loss of generality, one may safely assume that the magnetization of the fixed layer points along the $+\mathbf{x}$ direction. Starting from a parallel (P) magnetization configuration (both magnetization directions close to $+\mathbf{x}$), the spin transfer torque (28) tends to move the magnetization of the soft layer away from its initial direction for $J > 0$. Conversely, starting from an antiparallel (AP) configuration, spin transfer promotes parallel alignment for $J < 0$.

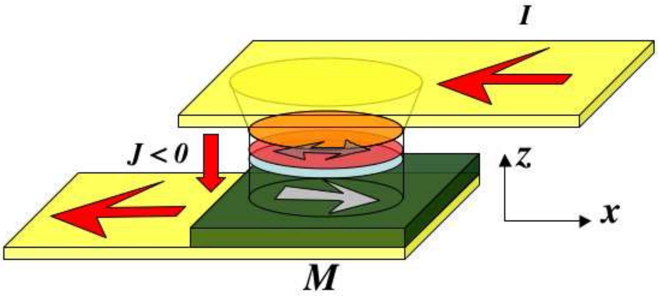

Fig. 16. Axes and sign conventions: note that the axes definition now conforms with the convention adopted by most experimentalists

Pillars like those used in the pioneering experiments of Albert et al. [104] have typical lateral dimensions in the 100 nm range with an in-plane aspect ratio close to 2:1 and soft layers with a thickness of a few nanometers. Because these stacks are nanofabricated from multilayers, we assume that the thickness of those elements remains constant across the element. Such elements are thus best described as flat cylinders with a close to elliptical cross-section. As a first approximation, it is convenient to think of the samples as pure ellipsoids because ellipsoids have uniform magnetizations and demagnetizing fields in equilibrium. However, the nanopillars do not behave entirely as pure ellipsoids. Even though the magnetization distribution only weakly departs from a uniform magnetization distribution at rest, the effective field is not uniform as as seen in Fig. 17.

Figure 17a displays the typical magnetization distribution within such an isolated thin element as a result of the competition between exchange and magnetostatic interactions. Due to demagnetizing effects, the effective easy magnetization axis coincides with the long ellipse principal axis. The color scheme highlights the weak deviations from uniformity close to the apices of this elliptical element. Clearly, these deviations help in reducing boundary magnetic charges at the expense of more distributed volume charges and exchange interactions. At equilibrium, there should be no torque acting on the magnetization [105, 106]:

$$\mathbf{M} \times \mathbf{H}_{\mathrm{eff}} = \mathbf{M} \times \left[-\frac{1}{\mu_0} \frac{\delta \epsilon}{\delta \mathbf{M}} \right] \equiv \mathbf{0} \,, \tag{27}$$

where $\mathbf{H}_{\mathrm{eff}}$ is the so-called effective field and ϵ the energy density, here including just exchange and demagnetizing field contributions. Fig. 17b displays a map of the effective field corresponding to the magnetization distribution in Fig. 17a, exhibiting large variations of the modulus of the demagnetizing field with a predictable influence on magnetization dynamics, be it under the action of an applied field or a current induced spin transfer torque. These variations lead to non-uniform behavior in the dynamics of such systems, limiting the validity of the macrospin approximation considered in Sec. 4.3.

The difference in energy between elliptical cylinders uniformly magnetized either along the long or the short ellipse axis is a good indicator of the thermal stability of such elements. The energy of the magnetization in either direction ($+\mathbf{x}$ and $-\mathbf{x}$) along the long axis is close to the ground state energy and that along the short axis is a first approximation to the energy barrier between the two equivalent ground states. An example of the results of such calculations is shown in Fig. 18. Assuming that a $40\,k_{\mathrm{B}}T$ barrier height is sufficient for long term stability, micromagnetics predicts that elliptical pillars should be stable at room temperature down to $L \approx 100\,\mathrm{nm}$ for the typical thicknesses and magnetic parameters of $\mathrm{Ni}_{80}\mathrm{Fe}_{20}$. Coming back to Fig. 16, it is clear that dipolar coupling between the thick and the thin layers does favor an antiparallel alignment of the magnetization directions (AP state).

4.2 Landau-Lifshitz-Gilbert Equation

We start by converting the spin densities $\mathbf{s}$ and number current densities $\mathbf{j}$ describing the torque Eq. (25) into magnetizations $\mathbf{M}$ and charge current densities $\mathbf{J}$. The magnetization and spin density are related through $\mathbf{M} = -(|g|\mu_{\mathrm{B}}/\hbar)\mathbf{s}$, where μ_{B} is the Bohr magneton ($\mu_{\mathrm{B}} > 0$). By convention, g_e is negative for free electrons. Since the orbital moment in transition metals

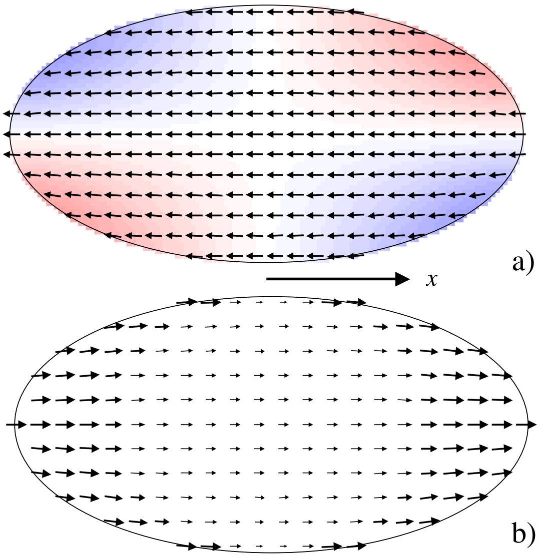

Fig. 17. Magnetization (a) and effective field (b) distributions typical of flat elliptical elements with long axis in the 130 nm range and 2:1 aspect ratio. $Ni_{80}Fe_{20}$, thickness $d = 2.5$ nm.

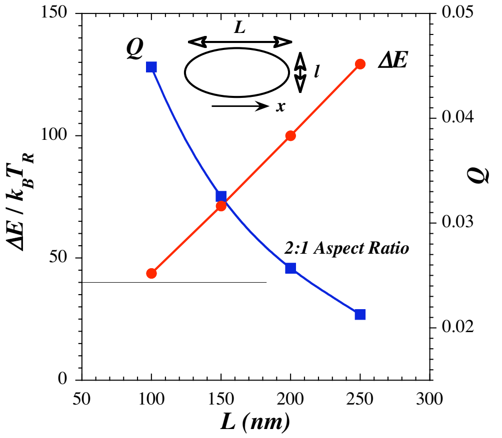

Fig. 18. Energy barrier between long and short axis uniformly magnetized elliptical elements ($Ni_{80}Fe_{20}$, $d = 2.5$ nm; room temperature, $T_R = 300\,K$). The shape induced anisotropy $Q = 2K/(\mu_0 M_S^2) = H_K/M_S$ is also plotted.

is small, the g-factor for transition metals is close to -2. We assume that the current flows normal to the interfaces of any of those devices sketched in Fig. 1, then, $\mathbf{j} \cdot \hat{\mathbf{z}} = -J/e$, J being the current density and e the charge of the electron ($e < 0$). Lastly, because the free layers of spin-injection devices need to remain ultra-thin for an optimized sensitivity to spin transfer torques (see above), it is assumed that the spin transfer torque is distributed over the thickness d of the soft element within the stack. The spin transfer torque is then

$$\left.\frac{d\mathbf{M}}{dt}\right|_{\mathrm{st}} = -\frac{|g|}{2}\frac{\mu_{\mathrm{B}}}{M_{\mathrm{S}}^2}\frac{1}{d}\frac{J}{e}\mathcal{P}\left[\mathbf{M}\times(\mathbf{M}\times\mathbf{p})\right] , \tag{28}$$

where J is the current per unit area, $\mathbf{M}$ the magnetization, $\mathbf{p}$ a unit vector in the direction of the fixed layer magnetization, $\mathcal{P}$ a polarization function that contains all the information stemming from the stack geometry and materials properties within the stack and depends on the relative orientations of the magnetizations. In most samples studied to date, $\mathcal{P}$ is generally positive, but it can be made negative by judicious choice of materials [12].

Starting with a magnetization distribution close to equilibrium under zero current, switching on the current allows the spin transfer torque to shift the magnetization away from its initial distribution. A new pattern of magnetic charges will appear that generates a new map of the demagnetizing field. Since there is no reason for the latter to be uniform, exchange interactions will also be modified. Summing-up, the magnetization will be subject to the micromagnetic effective field giving rise to a torque proportional to $\mathbf{M}\times\mathbf{H}_{\mathrm{eff}}$ and the spin transfer torque. Both are anticipated to be a function of position within the soft element. The total torque reads:

$$\begin{aligned}\frac{d\mathbf{M}(\mathbf{r})}{dt} = -\gamma_0\left[\mathbf{M}(\mathbf{r})\times\mathbf{H}_{\mathrm{eff}}(\mathbf{r})\right] - \frac{|g|}{2}\frac{\mu_{\mathrm{B}}}{M_{\mathrm{S}}^2}\frac{1}{d}\frac{J}{e}\mathcal{P}(\mathbf{r})\left[\mathbf{M}(\mathbf{r})\times(\mathbf{M}(\mathbf{r})\times\mathbf{p})\right] \\ + \alpha\left(\mathbf{M}(\mathbf{r})\times\frac{d\mathbf{M}(\mathbf{r})}{dt}\right) ,\end{aligned} \tag{29}$$

where γ_0 is the gyromagnetic ratio. The last term is the phenomenological Gilbert damping , which we assume without further proof may still be applied to magnetization dynamics in the presence of a spin-polarized current. The Gilbert damping constant α is typically of the order of 0.01. Eq. (29) is the Landau-Lifshitz-Gilbert (LLG) equation of magnetization motion augmented with the spin transfer torque term Eq. (28).

For the rest of the discussion, we ignore the spatial variation of the polarization function $\mathcal{P}$ and that of the magnetization direction of the nominally fixed layer $\mathbf{p}$. In reality, both of these vary. In a first approximation, the spatial variation of the polarization function could be treated using a laterally varying one-dimensional transport theory as outlined in Sec. 3. A better approximation would include lateral transport building on the discussion in Sec. 3.7. The spatial variation of the fixed layer magnetization could be treated explicitly through an equation like Eq. (29). However these effects are complications that should be added to an understanding built on simpler models. For instance, the inclusion of the dependence of the polarization function $\mathcal{P}$ on the magnetization direction, illustrated in Fig. 14, significantly complicates the use of generalized perturbation techniques, see Appendix B. For pedagogical purposes, the ability to use such techniques outweighs the quantitative differences in the results.

Up to this point, all equations in Sec. 4 have been written in the SI system of units. We can derive concise expressions for the LLG equation of magnetization motion with the appropriate variable reductions. Reduced variables include fields, magnetization, energy density and time, i.e. $\mathbf{H}$, $\mathbf{M}$, ϵ, t. Defining M_{S} as the saturation magnetization, SI and cgs units transform in dimensionless units as

$$\mathrm{SI}: \quad \mathbf{m} = \mathbf{M}/M_{\mathrm{S}} \quad \mathbf{h} = \mathbf{H}/M_{\mathrm{S}} \quad w = \epsilon/(\mu_0 M_{\mathrm{S}}^2) \quad \tau = \gamma_0 M_{\mathrm{S}} t \tag{30}$$

$$\mathrm{cgs}: \quad \mathbf{m} = \mathbf{M}/M_{\mathrm{S}} \quad \mathbf{h} = \mathbf{H}/(4\pi M_{\mathrm{S}}) \quad w = \epsilon/(4\pi M_{\mathrm{S}}^2) \quad \tau = 4\pi\gamma M_{\mathrm{S}} t. \tag{31}$$

The dimensionless LLG equation then reads:

$$\frac{d\mathbf{m}}{d\tau} = -\left(\mathbf{m} \times \mathbf{h}\right) - \chi\left[\mathbf{m} \times (\mathbf{m} \times \mathbf{p})\right] + \alpha\left(\mathbf{m} \times \frac{d\mathbf{m}}{d\tau}\right), \tag{32}$$

where we have suppressed the spatial dependence of all the quantities. The pre-factor of the spin transfer term

$$\chi = \frac{\hbar}{2}\frac{1}{\mu_0 M_{\mathrm{S}}^2}\frac{1}{d}\frac{J}{e}\mathcal{P}: \qquad [\mathrm{Js}]\left[\frac{1}{\mathrm{Jm}^{-3}}\right]\left[\frac{1}{\mathrm{m}}\right]\left[\frac{\mathrm{Cs}^{-1}\mathrm{m}^{-2}}{\mathrm{C}}\right][1] \tag{33}$$

is dimensionless as verified to the right of this equation by the units of each factor. This equation describes the magnetization dynamics in spin torque systems.

Manipulating Eq. (32) further gives an expression that characterizes the energy flow within these system. We take the cross product of the left and right hand sides of this equation with $d\mathbf{m}/d\tau$, use the triple cross product formula and factor out a common factor of $\mathbf{m}$ to give

$$\left(\mathbf{h} \cdot \frac{d\mathbf{m}}{d\tau}\right) + \chi\left((\mathbf{m} \times \mathbf{p}) \cdot \frac{d\mathbf{m}}{d\tau}\right) = +\alpha\left(\frac{d\mathbf{m}}{d\tau}\right)^2. \tag{34}$$

Eq. 34 underlies the whole of magnetization dynamics, including spin torque, in the classical limit. It expresses the trade-off between dissipation , the work per unit time (power) of the effective field, and power of the spin torque for which the (dimensionless) equivalent field is $\chi\,(\mathbf{m} \times \mathbf{p})$. In the next section, we consider the macrospin approximation in detail. Before we do, it is worthwhile to examine Eq. 34 in this limit. We see that when $\chi = 0$ ($J = 0$), the magnetization may not precess along a closed orbit in the absence of any time-periodic driving field, unless the damping is also zero. On the other hand, when $\chi \neq 0$, closed magnetization orbits are allowed even for non-zero damping. Integrating Eq. 34 around a closed path expresses this point mathematically. Micromagnetic fields are conservative so that integrating them along a closed path gives zero, that is $\oint \mathbf{h}^{\mu\mathrm{Mag}} \cdot d\mathbf{m} \equiv 0$. For a stable trajectory, the dissipated energy must equal the work due to the spin transfer over one period. Mathematically, this amounts to saying that for any closed magnetization trajectory Γ, the following relation should (cf Eq. 34) be satisfied:

$$\int_{\Gamma} \left[\chi \left((\mathbf{m} \times \mathbf{p}) \cdot \frac{d\mathbf{m}}{d\tau} \right) - \alpha \left(\frac{d\mathbf{m}}{d\tau} \right)^2 \right] d\tau = 0 \tag{35}$$

Trajectories that satisfy this condition are called precessional states. The existence of such closed magnetization orbits is a key prediction of spin transfer induced magnetization dynamics.

4.3 The single or macro-spin approximation

Despite the words of caution above, the macro-spin approximation remains essential in deciphering the main features of magnetization dynamics under the action of the spin transfer torque. One needs first to define an energy functional for the system under study. In a minimal approach, due to the large lateral dimension/thickness ratio, the demagnetizing field may be approximated by that of a thin elliptical cylinder. Since the thickness is so small compared to the in-plane dimensions, the dominant term is approximately the demagnetizing field of a uniformly magnetized thin film with infinite lateral dimensions, namely $\mathbf{H}_{\mathrm{D}} = [0, 0, -M_{\mathrm{S}} m_z]$. The associated energy density amounts to $\epsilon = -(1/2)\, \mu_0 \mathbf{M} \cdot \mathbf{H}_{\mathbf{D}} = -(1/2)\, \mu_0 M_{\mathrm{S}}^2 m_z^2$. The remaining terms describe demagnetizing effects linked to the shape of the soft element and are equivalent to a shape anisotropy of type $K\left(1 - m_x^2\right)$. Including the Zeeman energy, the overall energy density reads:

$$\epsilon = K\left(1 - m_x^2\right) + \frac{1}{2}\mu_0\, M_{\mathrm{S}}^2 m_z^2 - \mu_0\, \mathbf{M} \cdot \mathbf{H}^{\mathrm{a}}\,, \tag{36}$$

where $\mathbf{H}^{\mathrm{a}}$ is the applied field. In the following, we assume that the applied field has a non-zero component only along $\mathbf{x}$, the in-plane easy axis (see Fig. 16). When pulled out of equilibrium, the magnetization is subject to an effective field

$$\mathbf{H}_{\mathrm{eff}} = -\frac{1}{\mu_0 M_{\mathrm{S}}} \frac{\delta\epsilon}{\delta\mathbf{m}} = \left[H_x^{\mathrm{a}} + H_{\mathrm{K}} m_x,\ 0,\ -M_{\mathrm{S}} m_z\right]\,, \tag{37}$$

where $H_{\mathrm{K}} = 2K/(\mu_0 M_{\mathrm{S}})$ is the anisotropy field.

In dimensionless form, Eqs. 36 and 37 become:

$$
\begin{aligned}
w &= \frac{1}{2} Q \left(1 - m_x^2\right) + \frac{1}{2} m_z^2 - \mathbf{m} \cdot \mathbf{h}^{\mathrm{a}} \\
\mathbf{h}_{\mathrm{eff}} &= -\frac{\delta w}{\delta \mathbf{m}} = \left[h_x^{\mathrm{a}} + Q m_x,\, 0,\, -m_z\right] \,,
\end{aligned}
\tag{38}
$$

with $Q = 2K/(\mu_0 M_{\mathrm{S}}^2) = H_{\mathrm{K}}/M_{\mathrm{S}}$. Q provides a measure of the strength of the shape anisotropy versus stray field energy.

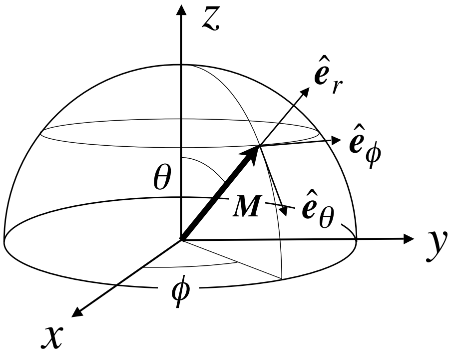

Fig. 19. Spherical coordinates: definition of angles. The usual Cartesian magnetization components read: $m_x = \cos\phi \, \sin\theta$, $m_y = \sin\phi \, \sin\theta$, $m_z = \cos\theta$.

The magnetization vector $\mathbf{m}$ has a fixed length, which suggests that we convert the equations of motion into spherical coordinates, namely:

$$
\begin{aligned}
\frac{d\theta}{d\tau} &= h_\phi - \alpha \sin\theta \frac{d\phi}{d\tau} \\
\sin\theta \frac{d\phi}{d\tau} &= -h_\theta + \alpha \frac{d\theta}{d\tau}
\end{aligned}
\tag{39}
$$

where θ and ϕ are the polar and azimuthal angles, as defined in Fig. 19, and h_θ, h_ϕ the reduced field components stemming both from the micromagnetic response of the system and spin transfer

$$
h_\theta = h_\theta^{\mu\mathrm{Mag}} + h_\theta^{\mathrm{ST}}; \qquad h_\theta^{\mu\mathrm{Mag}} = -\frac{\partial w}{d\theta}; \qquad h_\theta^{\mathrm{ST}} = -\chi p_\phi \tag{40}
$$

$$
h_\phi = h_\phi^{\mu\mathrm{Mag}} + h_\phi^{\mathrm{ST}}; \qquad h_\phi^{\mu\mathrm{Mag}} = -\frac{1}{\sin\theta} \frac{\partial w}{d\phi}; \qquad h_\phi^{\mathrm{ST}} = +\chi p_\theta \tag{41}
$$

p_θ and p_ϕ being the components of the fixed layer magnetization direction in spherical coordinates. It is also convenient to convert the LLG equation from the Gilbert form, in which the damping depends explicitly on $d\mathbf{m}/d\tau$ to the Landau-Lifshitz form in which it depends on the effective field. The vector LLG equation, Eq. (32) becomes a set of two first order differential equations

$$\begin{aligned}\left(1+\alpha^2\right)\frac{d\theta}{d\tau} &= h_\phi + \alpha h_\theta \\ \left(1+\alpha^2\right)\sin\theta\frac{d\phi}{d\tau} &= -h_\theta + \alpha h_\phi\,,\end{aligned} \tag{42}$$

Onset of precessional states

Numerical integration of an equation similar to Eq. 29, or, preferably, Eq. 42 gives stable precessional states, as first demonstrated by Sun [107]. Within the macro-spin approximation, the current threshold for the establishment of a stable magnetization trajectory may be simply derived from standard perturbation theory. Clearly, in the absence of current and under the action of any applied field $h_x^{\mathrm{a}} > 0$, the stable magnetization direction satisfies $m_x = 1$, or, $\theta = \pi/2$, $\phi = 0$. The damping constant α is generally small. In the trajectories we are interested in, the spin-transfer torque roughly balances the damping so that χ is of the same order of magnitude as α and both can be treated as small parameters. To investigate the onset of stable precessional states, we focus on trajectories in which the magnetization is close to its equilibrium direction. This suggests the replacement $\theta = \pi/2 + \xi$, so that ξ and ϕ can be treated as small. Taking $1 + \alpha^2 \cong 1$ leads to the following linearized equations of magnetization motion

$$\begin{aligned}\frac{d\xi}{d\tau} &= h_\phi + \alpha h_\theta \\ \frac{d\phi}{d\tau} &= -h_\theta + \alpha h_\phi\end{aligned} \tag{43}$$

with

$$\begin{aligned}h_\theta &= -\left(1 + Q + h_x^{\mathrm{a}}\right)\xi - \chi\phi \\ h_\phi &= +\chi\xi - \left(Q + h_x^{\mathrm{a}}\right)\phi.\end{aligned} \tag{44}$$

If D is the differential operator $D = d/d\tau$ and $u = Q + h_{\mathrm{x}}^{\mathrm{a}}$, the characteristic equation for the set of linear differential equations (43, 44) becomes:

$$D^2 + \left[\alpha + 2\left(\alpha u - \chi\right)\right]D + u\left(1+u\right) = 0 \tag{45}$$

Its determinant proves to be strictly negative to the lowest order in α and χ implying complex conjugate eigenvalues, μ. The focus $m_x = 1$ is stable when $\mathrm{Re}\mu > 0$, unstable in the opposite case. Converting to real time units, equations (43, 44) lead to elliptical precession proportional to

$$\exp(-t/t_0)\cos(\omega t + \Phi_0) \tag{46}$$

where

$$\begin{aligned}t_0 &= \frac{1}{\gamma_0 M_{\mathrm{S}}(\chi_{\mathrm{crit}} - \chi)} \\ \omega &= \gamma_0 M_{\mathrm{S}}\sqrt{u\left(1+u\right) - \left[\chi_{\mathrm{crit}} - \chi\right]^2}\end{aligned} \tag{47}$$

with,

$$\chi_{crit} = \alpha \left(\frac{1}{2} + Q + h_x^{\mathrm{a}} \right) \cong \frac{\alpha}{2} \quad \text{if} \quad Q,\, h_x^{\mathrm{a}} \ll 1 \tag{48}$$

Therefore, magnetization motion is expected to be exponentially damped out for χ less χ_{crit} (low currents) and exponentially amplified as the current increases to the point where $\chi > \chi_{crit.}$. As is usual, the characteristic time t_0 goes to infinity when $\chi = \chi_{crit}$. On the other hand, the angular precession frequency ω goes through a maximum equal to Kittel's resonance frequency $\omega_{\mathrm{K}} = \gamma_0 M_{\mathrm{S}} \sqrt{Q + h_x^{\mathrm{a}}}\,\sqrt{1 + Q + h_x^{\mathrm{a}}}$ at the transition.

In first approximation (Q, $h_x^{\mathrm{a}} \ll 1$), the critical current is proportional to the damping parameter , the soft layer thickness and to the square of the saturation magnetization. It is represented by the line labeled χ_1 in Fig. 22 that displays the phase diagram of the magnetization states in the $h_x^{\mathrm{a}} > 0$ half space. [1] As anticipated, direct numerical estimates of the critical current for the onset of precessional motion as a function of applied field are in perfect agreement with Eq. 48. Stability calculations such as these can be used to determine the stability ranges of the different configurations for different anisotropies and applied fields. Bazaliy et al. [108, 109] and Xi et al. [110] have carried out a variety of such calculations for various magnetic configurations.

As an illustration, using typical parameters for $\mathrm{Ni_{80}Fe_{20}}$ ($\mu_0 M_{\mathrm{S}} = 1$ T, $\alpha = 0.01$, $d = 2.5$ nm), one arrives at a critical current density $J_{\mathrm{c1}} \approx 3 \times 10^{10}$ A/m^2 or 30 mA/μm^2 for a 100 % polarization in zero field. For a typical elliptical element with lateral dimensions 130 × 70 nm^2, this would correspond to a current ≈ 0.2 mA. A three times higher current would be required for a more realistic electron polarization of 1/3.

Precessional states: stability range

In the previous section, we have shown that for current greater than the critical current, the static state becomes unstable to precession. However, this calculation does not address the issue of how large the precession becomes because the precession amplitude is determined by the non-linearities of the system. For currents just above the critical current, we compute numerically the finite precession amplitude that occurs. Concentrating first on the case with no applied field, $h_x^{\mathrm{a}} = 0$, simulations do show that stable magnetization trajectories may be found over a finite current range. Trajectories open up with increasing current beyond J_{c1} as shown in Figs. 20 and 21. This opening up can be monitored by the minimal and maximal ϕ values. In the immediate vicinity of J_{c1}, ϕ_{Max} increases with an infinite slope, a characteristic signature of a simple Hopf bifurcation (Fig. 21). Note that we use a double x scale in

---

[1] Unless otherwise stated, all simulations in sections 4.3 and 4.4 use parameters mimicking a $130 \times 65 \times 2.5\,\mathrm{nm}^3$ $\mathrm{Ni_{80}Fe_{20}}$ elliptical platelet, namely $M_{\mathrm{S}} = 800\,\mathrm{kA/m}$, $H_{\mathrm{K}} = 29.05\,\mathrm{kA/m}$ ($Q = 0.0365$), $\gamma_0 = 2.21\,10^5\,(\mathrm{s\,A/m})^{-1}$, $\alpha = 0.01$.

Fig. 21: the top scale refers to the current density ($A/\mu\mathrm{m}^2$), the lower to the corresponding χ/α value. As shown in Appendix B, χ/α is the true reduced current density and damping-related variable in this non-linear magnetization dynamics problem.

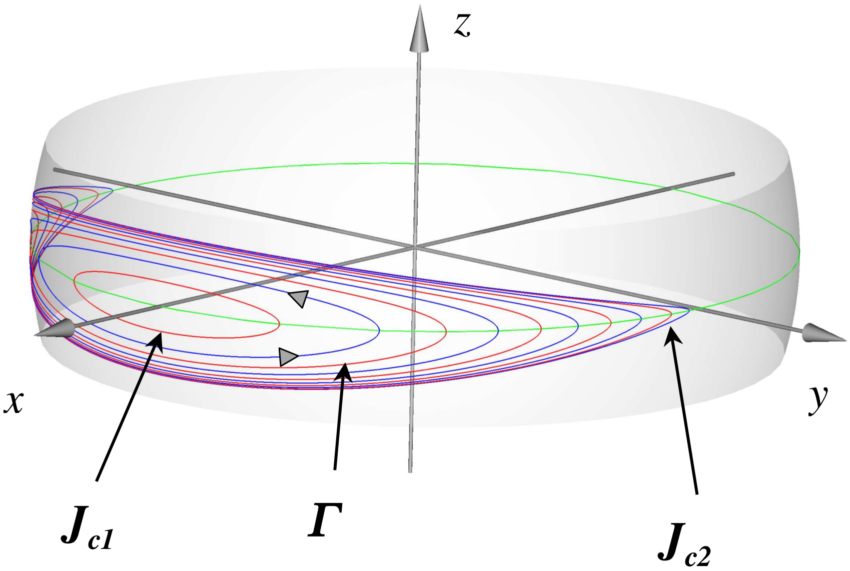

Fig. 20. Closed orbits characteristic of precessional states for current densities $J = 0.11 - 0.13$ in steps of $0.0025\,A/\mu\mathrm{m}^2$ and $J = 0.13175\,A/\mu\mathrm{m}^2$ in the single spin approximation. $h_x = 0$. The locus of the extrema of ϕ materialized by the light green line is slightly inclined with respect to the equatorial plane. See text for details

Soon after the onset of precessional states, the precession frequency decreases almost linearly with increasing current density (Fig. 21). Close to a second threshold, J_{c2}, trajectories pile up against a typical eye-shaped curve (Fig. 20), that is later going to be identified with a homoclinic cycle (see Appendix B). Whilst doing so, the velocity of the magnetization direction along a given trajectory, Γ, on the surface of the unit sphere, namely

$$\frac{ds}{d\tau} = \sqrt{\left(\frac{d\theta}{d\tau}\right)^2 + \sin^2\theta\left(\frac{d\phi}{d\tau}\right)^2} \tag{49}$$

is seen to drop to almost zero at the apices of the trajectory (Fig. 25a). The spin torque is however largest there. From a static point of view, it has to be compensated by another torque: the latter derives from the demagnetization field, hence a slight slanting of the trajectory that, in first approximation, obeys

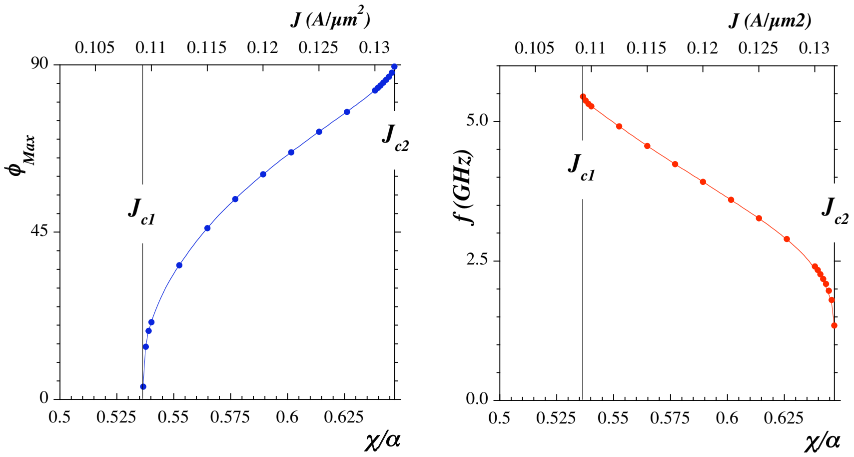

Fig. 21. Orbit opening as a function of current density (left) and associated precession frequency (right)

$$\begin{aligned} & m_z^{\mathrm{Apex}} + \chi m_y^{\mathrm{Apex}} = 0 \\ & \text{or,} \\ & \frac{\pi}{2} - \theta^{\mathrm{Apex}} = \chi \sin\left(\phi^{\mathrm{Apex}}\right) \end{aligned} \tag{50}$$

It also ought to be noted that the velocity distribution is not symmetrical (see Fig. 25a), another result of magnetization trajectories slanting. Lastly, close to $J_{\mathrm{c}2}$, the precession frequency collapses to zero (Fig. 21).

Switching and out-of-plane precessional states

Increasing the current density beyond $J_{\mathrm{c}2}$ leads to one of two possible events. As long as $h_x^{\mathrm{a}} < Q$, the system switches to a configuration with the magnetization opposite to the ground state, in the $-\hat{\mathbf{x}}$ direction. As shown in Fig. 23a, switching takes place when magnetization trajectories bifurcate close to one of the saddle points S_1 and S_2 [111]. Then, depending on the exact current density, switching takes place via either a clockwise or a counterclockwise motion. As first noticed by Sun [107], as soon as the magnetization has moved from one attraction basin (say F_1) into the next (say F_2) the spin transfer torque acts as an effective additional damping term as evidenced by the small number of ringing oscillations before reaching equilibrium despite the small Gilbert damping constant. Switching in the single spin approximation at 0 K is therefore to be viewed as a three stage event (Fig. 23a): during the initial phase, the magnetization creeps out of its initial equilibrium position through precession around the demagnetizing field that is parametrically amplified under the action of the spin transfer torque. It is indeed a parametric excitation because the spin transfer torque is a function of the magnetization orientation.

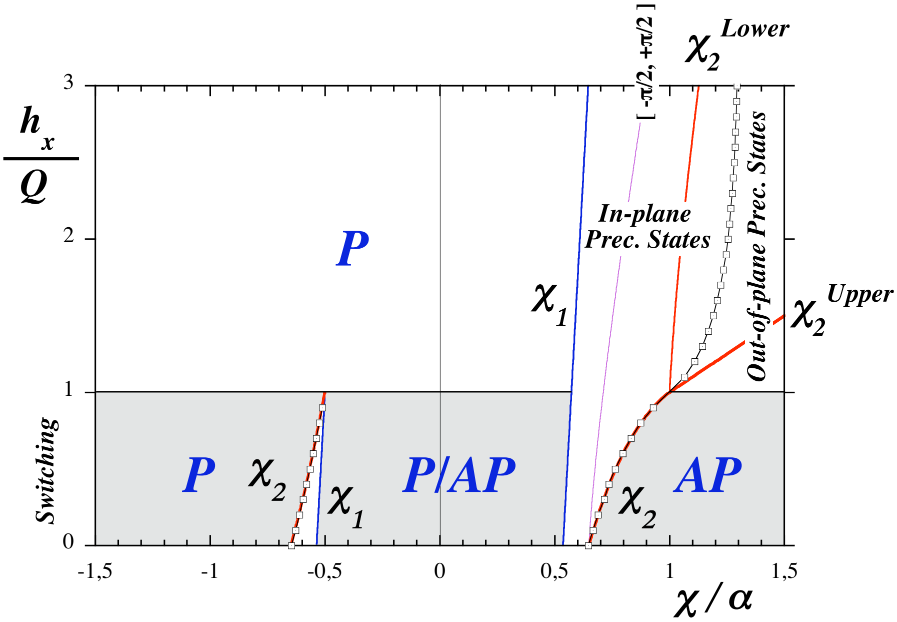

Fig. 22. Phase diagram in the $h_x > 0$ half space as a function of χ/α, a dimensionless quantity proportional to the current density. The line $h_x/Q \cong 1$ schematically separates regions where switching may take place (i.e. between neighboring shaded areas) from regions where only a positive current may upset the parallel alignment enforced by the applied field. Curves labelled χ_1 correspond to transitions between stable (P or AP) states and precessional states of type shown in Fig. 20 (In-plane Prec. States). Open square symbols delineate the transition between an In-plane Prec. State and a reversed state ($h_x/Q < 1$) or an Out-of-plane Prec. State ($h_x/Q > 1$) according to numerical micromagnetics in the single-spin approximation. Curves labelled χ_2 correspond to the critical switching current *vs.* field according to Melnikov's method. When $h_x > Q$, the critical current χ_2/α for transition between an In-plane and an Out-of-plane Prec. State may not be estimated directly, although bounds to χ_2/α may be defined (curves labelled χ_2^{Lower} and χ_2^{Upper}: see Appendix B for details). The faint line between χ_1 and χ_2-χ_2^{Lower} is the locus for In-plane Prec. States with π span in the equatorial (sample) plane.

Following bifurcation (second phase), a more highly damped precession type motion (third stage) drives the magnetization into its new equilibrium state. Spin transfer induced switching therefore appears to qualitatively mirror a field induced precessional switching event [105, 112, 113] where the initial phase proves ringing-free whereas relaxation within the new potential well may imply a large number of ringing oscillations. Critical currents vs. applied field for bifurcation into a reversed state ($h_x < Q$) are shown as square symbols in Fig. 22.

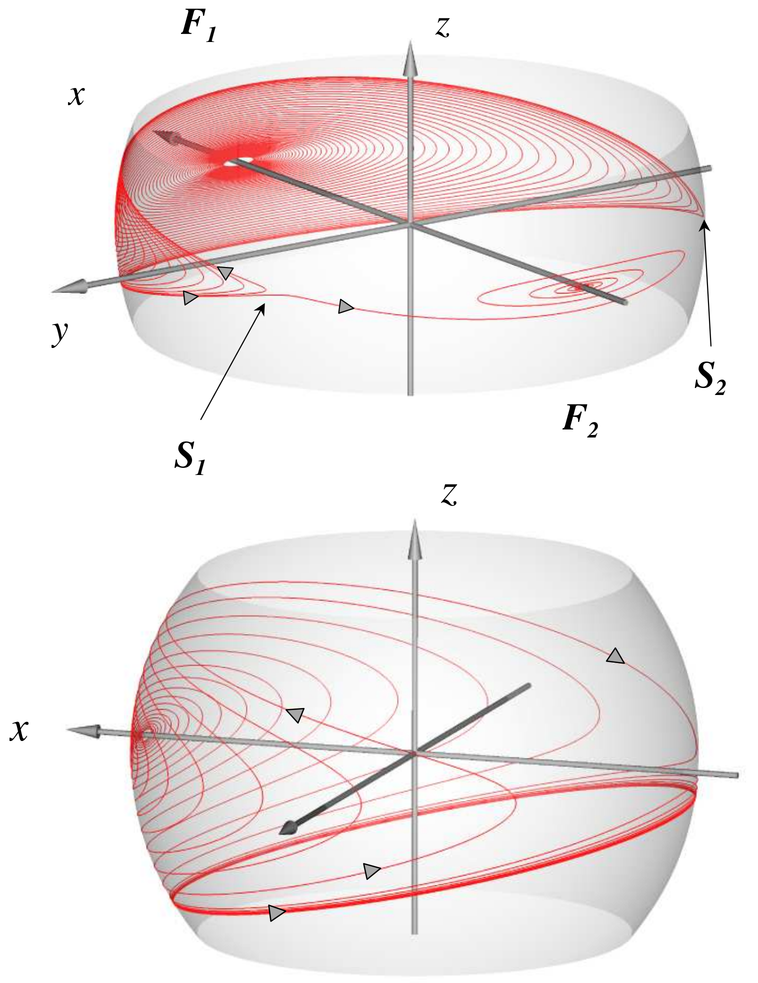

Fig. 23. Top : example of switching trajectory ($h_x^{\mathrm{a}} = Q/2$, $\chi/\alpha = 0.77$); F_1 and F_2 are fixed points owing to sample energetics whereas S_1 and S_2 are saddle points that correspond to a velocity minimum along the switching trajectory. Bottom : bifurcation to an out-of-plane precessional state ($h_x^{\mathrm{a}} = 2Q$, $\chi/\alpha = 1.75$)

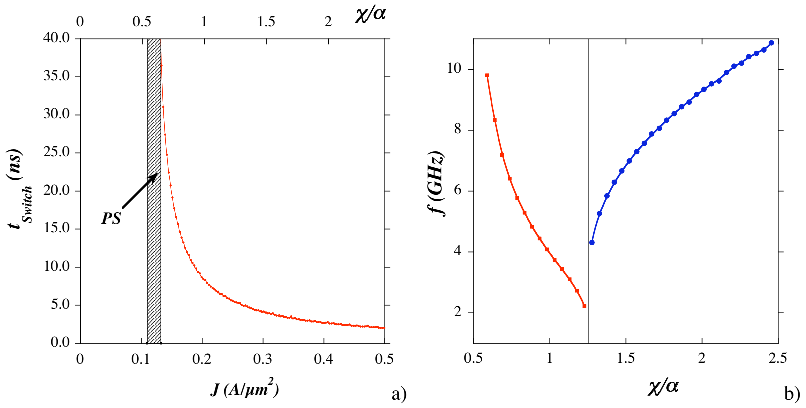

Fig. 24. a) Switching time vs. current density at zero temperature and field. In this example, the switching time behaves roughly as $(J - J_{c1})^{\eta}$ with $\eta \approx -0.9$, i.e. a value close to expectation based on perturbation theory ($\eta = -1$ [107]); b) Frequency of precessional states (in-plane to the left, out-of-plane to the right) for $h_x = 2Q$ at zero temperature

In the previous section, the onset of precessional states could be derived from elementary perturbation theory. However, the switching current is distinctly different than the critical current for the onset of precessional states, as seen in numerical simulations. However, no closed form could be established for the switching current starting from simple perturbation theory. As shown in Appendix B, such a result may be derived from Melnikov's method [114, 115], a method applying to weakly perturbed time periodic Hamiltonian systems for which unperturbed trajectories in space may be derived from the energy landscape. Within the relevant field interval $-Q \le h_x \le Q$ and within the framework of our simple energetics, the critical current for switching is found to be equal to:

$$\frac{\chi_2}{\alpha} = r^2 \sqrt{1+Q} \left[\frac{h\,\xi_S + \sqrt{Q}\sqrt{1-\frac{h_x^2}{Q^2}}}{h\sqrt{1-\frac{h_x^2}{Q^2}} + r^2\sqrt{Q}\,\xi_S} \right] \tag{51}$$

with $h = \frac{h_x}{Q}\sqrt{\frac{Q}{1+Q}}$, $r^2 = 1 - h^2$, $\xi_S = \cos^{-1}(-\frac{h}{\sqrt{Q}\sqrt{1-h^2}})$ (see Appendix B for details). Notable switching currents values include $\frac{\chi_2}{\alpha} = \frac{1}{2}, \frac{2}{\pi}\sqrt{1+Q}$ and 1 for $h_x = -Q, 0, +Q$, respectively. The reduced critical current density for switching in the interval $-Q \le h_x \le Q$ ($-H_K \le H_x \le H_K$) is displayed as line labelled χ_2 in Fig. 22. Clearly, the agreement with numerical simulations in the single-spin approximation proves excellent. Lastly, the time necessary for switching is very close to the time necessary to reach the bifurcation point and depends sharply on the current density as shown in Fig. 24a.

When $h_x^{\rm a} > Q$, switching in the conventional sense does not occur because the field exceeds the effective anisotropy field. Instead, a bifurcation takes place between a closed orbit that is essentially symmetrical with respect to to the equatorial plane ($z = 0$) and another closed orbit either above or below the equatorial plane as shown in Fig. 23b. Similarly to "in-plane" precessional trajectories, the velocity along "out-of-plane" trajectories also proves to be highly non-uniform as shown in Fig. 25b.

Lastly, the case $h_x^{\rm a} = Q$ ($H_{\rm x}^{\rm a} = H_{\rm K}$) proves singular. Mathematically, the switching time diverges to ∞. However, such a situation is not robust against thermal fluctuations and leads to intermittency as shown in Fig. 4. Here also, critical currents vs. applied field for bifurcation into an "out-of-plane" precessional state are shown as square symbols in Fig. 22. Note that precessional states are expected to be precursor states to both the "P" to "AP" and "AP" to "P" transitions, as confirmed by experiments [116]. At zero temperature, the frequency of precessional states follows trends indicated in Fig. 24b for a given value of the applied field. Essentially, the frequency decreases with increasing current for "in-plane" precessional states whereas the opposite behavior characterizes "out-of-plane" precessional states.

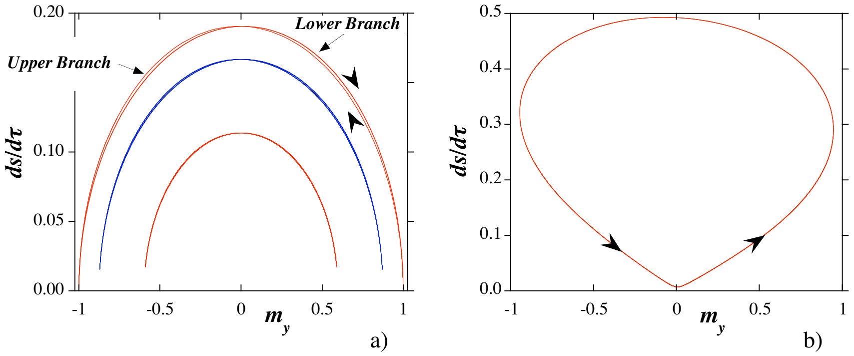

Fig. 25. Velocity along closed orbits. a) $h_x^{\rm a} = 0$, $J = 0.1150, 0.1225, 0.13175\, A/\mu{\rm m}^2$, i.e. $\chi/\alpha = 0.5647, 0.60155, 0.64697$; b) $h_{\rm x}^{\rm a} = 2Q$, $m_z > 0$ (upper branch), $J = 0.256\, A/\mu{\rm m}^2$, i.e. $\chi/\alpha = 1.2571$. Motion is counterclockwise and clockwise for the upper and lower branches, respectively.

4.4 Langevin dynamics

The results in the previous sections were computed at zero temperature. They provide a reasonably accurate description of measurements made at low (liquid He) temperatures. However, most experiments are done at room temperature where thermal effects become much more important. Finite temperatures cause the system to fluctuate between states. For the most part, these states are close-by to the zero temperature state, but large fluctuations can cause transitions over barriers into other stable or metastable states. Thus, finite temperatures change the transition between states from deterministic to statistical. Thermal effects can be modelled through statistical descriptions in Fokker-Planck approaches [117, 118] or barrier crossing models [25, 33]. Alternatively, thermal effects can be included in dynamical simulations through the addition of a random field, H_{Rd}, to the effective field. Each component of H_{Rd} is uncorrelated both in space and time and obeys a purely Gaussian distribution with zero average value and variance μ:

$$\begin{aligned} \langle H_{\mathrm{Rd}} \rangle &= 0 \\ \langle H_{\mathrm{Rd}}^{i}(t)\, H_{\mathrm{Rd}}^{j}(t') \rangle &= \mu\, \delta_{ij}\, \delta(t-t') \\ \mu &= \frac{2k_{\mathrm{B}}T}{\mu_0 \gamma_0 M_{\mathrm{S}} V}\alpha \end{aligned} \tag{52}$$

as derived from the application of the fluctuation dissipation theorem [119]. Here V is the volume of the sample for macrospin simulations and the volume of the simulation cells for micromagnetic simulations (see next section).

Several authors have studied the effect of thermal fluctuations in macrospin models and simulations [25, 33, 117, 120, 118, 121]. The main effect is that thermal fluctuations promote transitions between metastable (or stable) zero temperature configurations. These fluctuations move the phase boundaries shown in Fig. 22 and give them a degree of indeterminacy. Figure 26 illustrates the stochastic nature of finite temperature switching. It shows the distribution of switching times for two pairs of fields and currents. For one pair, the system is stable (and would never switch) at zero temperature, and for the other it is unstable and would switch with a unique switching time at zero temperature.

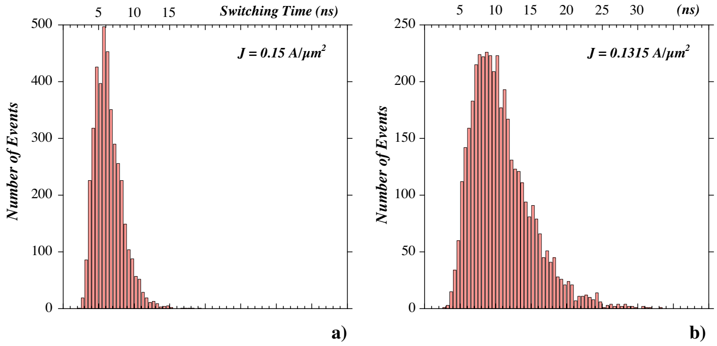

Fig. 26. Switching time distribution at 300 K for $H_x = 0$. Average over 4096 trajectories. a) $J = 0.15\,\mathrm{A}/\mu\mathrm{m}^2$: current density slightly above the switching threshold at 0K; b) $J = 0.1315\,\mathrm{A}/\mu\mathrm{m}^2$: current density just below the switching threshold at 0K.

Generally speaking, switching time distributions appear to be pseudo-log-normal, with a rapidly increasing distribution width as soon as the current density falls below the switching threshold at 0 K. Experiments do not yield switching time distributions for preset current densities but rather switching probabilities vs. current density for preset waiting times or current ramp rates [25, 34, 116]. Measured distributions of switching currents are substantially skewed on the side of the small current densities (absolute value). Unfortunately, typical experimental waiting times (ramp rates) prove far too long (too slow) for direct comparisons to be made between experimental data and Langevin dynamics predictions, even in the single spin regime. An important conclusion of [34] is that the barrier height appears mostly independent of the free layer thickness, a disproof of any thermal activation model over a single barrier. Indeed, as shown below, full scale micromagnetic simulations lead to genuinely complex representations of spin-transfer induced switching.

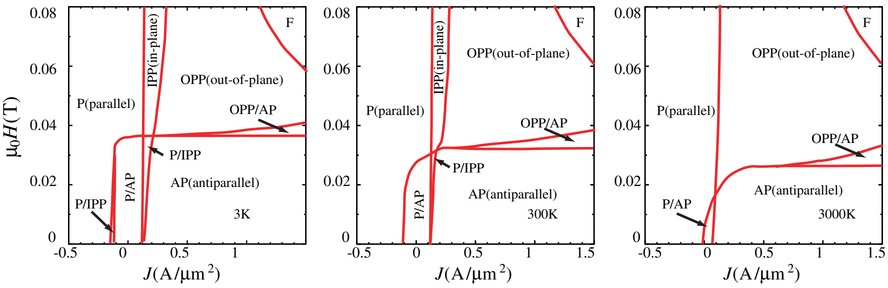

Fig. 27. Dynamic phase diagrams for a 130 nm by 70 nm elliptical Co free layer of thickness 3 nm. Left panel: $T = 3$ K; middle panel: $T = 300$ K; Right panel: $T = 3000$ K. For fixed H, a bistable region labelled A/B exhibits the A state when J is scanned from left to right and the B state when J is scanned from right to left. The correspondence needed to compare with Fig. 6 is 10^8 A/cm^2 $\leftrightarrow$ 10 mA. "F" refers to a configuration with a fixed magnetization direction that is not along the easy axis.

Russek et al. [120] and Xiao et al. [121] have computed the effect of temperature on phase diagrams like that shown in Fig. 22. The evolution of the phase boundaries with temperature in illustrated in Fig. 27. These phase diagrams were computed by sweeping the current at fixed field as done in the experiment in Fig. 6. However, as noted above, the field sweep rates in the calculation are orders of magnitude faster than those in the experiment. The effect of the slower sweep rate can be qualitatively captured by considering higher temperatures, hence the calculation at the unphysical temperature of 3000 K. The 3000 K simulation gives some indication of how the 300 K simulation might look if the sweep rate was comparable to that of the experiment. This indication is only approximate because the trade off between sweep rate and temperature depends on the energy barrier between the competing configurations and this energy barrier varies throughout the phase diagram. These finite temperature simulations show trends toward better agreement with the results in Fig. 6. Two differences are apparent. The simulation does not show the "W" phase, in which there is no apparent precessional peak, but which has a resistance distinctly different than the antiparallel state. On the other hand, there is no indication of the high current, high field fixed phase "F" in the experimental data.

Temperature also affects the details of the precessional dynamics [120]. In the single spin and zero temperature limit, precessional states are characterized by a frequency that is just a function of current density, in-plane anisotropy and damping parameter. In the frequency domain precessional states are thus defined by a pure Dirac delta function. Raising the temperature introduces stochasticity in the magnetization trajectories. As a result of the action of the stochastic field, magnetization motion also displays fluctuations when compared to the 0K limit. Of major interest here is a quantity that measures the influence of a value of the function $\mathbf{m}$ at time t on the value at time $t + \xi$, a quantity called the autocorrelation function (see e.g. [122]). The Power Spectrum Density (PSD) of a scalar quantity $x\,(t)$ is the Fourier transform of the autocorrelation function (Wiener-Khinchin theorem). It is the "power" emitted within the interval $[f, f + df]$ (natural units W/Hz). Physically, a long correlation time corresponds to nicely peaked power spectra whereas short correlation times yield flat spectra. Lastly, it ought to be stressed that care is necessary when estimating PSD's from data $x\,(t)$ extending over finite times (see e.g. [123] for an outlook at windowing and averaging methods).

Figs. 28 and 29 ($H_x = 2H_{\mathrm{K}}$) display the main results to be expected from the single spin model at low temperature in a current regime allowing for precessional states of the first kind (see Fig. 20). Due to symmetry of the closed magnetization trajectories with respect to $\mathbf{x}$, the easy magnetization axis, the fundamental frequency for a given current density is given by the power spectrum density of the m_y magnetization component, whereas the PSD deduced from m_x corresponds to twice the fundamental frequency. Thus, depending on the observable, PSD's may reveal either the fundamental frequency, its first harmonics or a mixture of both, as well as higher harmonics. Hopefully, however, ambiguity in the spectral response should in most cases be lifted due to the fact that, at the onset of sustained precession, the fundamental frequency is equal to Kittel's resonance frequency, which only depends on materials parameters and applied field (see section 4.3). Figs. 28 and 29 show that the peak in the PSD initially grows with rising current density as the frequency decreases (the so-called "redshift" regime owing to [30]). Further increases of the current density lead to a decrease of the peak in the PSD and power is gradually transferred into higher harmonics, namely $3, 5..., (2n + 1)\,f$ for the m_y PSD, $2, 4..., (2n)\,f$ for the PSD stemming from m_x. In this precessional regime, in agreement with the phase diagram in Fig. 22 and general perturbation theory (Appendix B), closed magnetization orbits gradually open up up

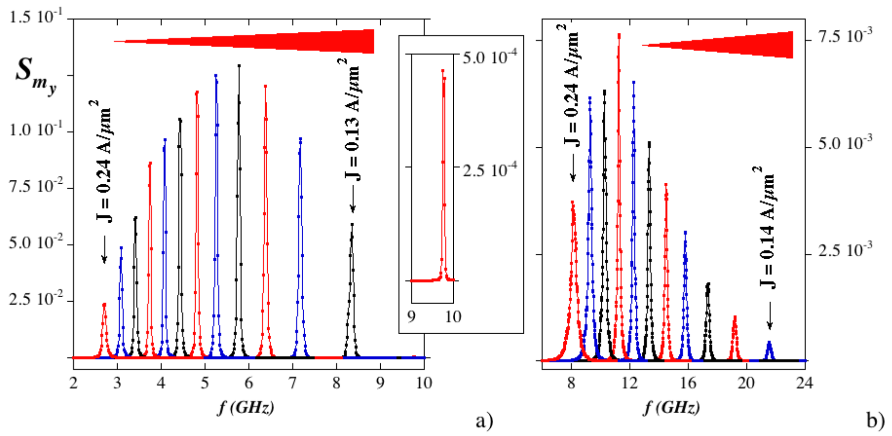

Fig. 28. m_y power spectrum density (PSD) vs. current density at 4.2K for $H_x = 2H_\mathrm{K}$. Current density step: 0.01 A/μm^2. "Low" current density regime: precessional states essentially symmetrical with respect to the sample plane. a) fundamental frequency $f(J)$). The frequency decreases with increasing current (redshift), as symbolized by the elongated red triangle. Inset: PSD very close to Kittel's resonance frequency; b) 3rd harmonics. Pollution from higher harmonics has been removed.

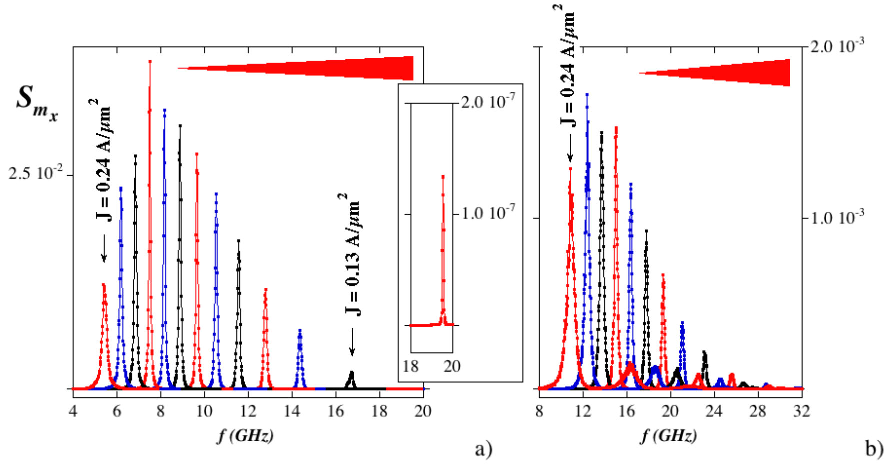

Fig. 29. m_x Power spectrum density vs. current density at 4.2K for $H_x = 2H_\mathrm{K}$. Current density step: 0.01 A/μm^2. "Low" current density regime: precessional states essentially symmetrical with respect to the sample plane. a) lowest frequency. Inset: PSD in the immediate vicinity of twice Kittel's resonance frequency; b) harmonics.

to extremely wide excursion angles (from typically $\pm\pi/3$ for $J = 0.13\,\mathrm{A}/\mu\mathrm{m}^2$ to $\pm\pi$ for $J = 0.24\,\mathrm{A}/\mu\mathrm{m}^2$). A plot of the log of the power spectrum density vs. frequency (not shown) indicates the presence of higher harmonics to orders up to about 20 with a close to exponential decay of the PSD maximum with increasing frequency (typically 30 dB per octave). Note also that at these very low temperatures and usual damping parameter ($\alpha = 0.01$ in these simulations), the line width remains extremely narrow with full width at half maximum in the 70 MHz to 80 MHz range.

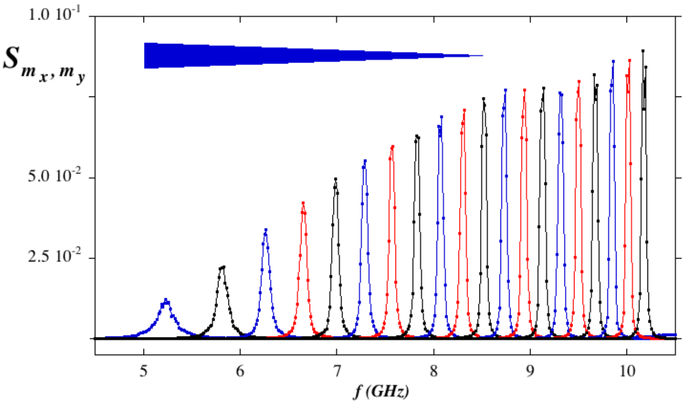

Fig. 30. Power spectrum density vs. current density at 4.2K for $H_x = 2H_\mathrm{K}$. "High" current density regime: out-of-plane precessional states. The frequency increases with increasing current (blueshift), as symbolized by the elongated blue triangle. The m_x and m_y spectra are indistinguishable in this regime. Current density ranging from 0.27 to $0.45\,\mathrm{A}/\mu\mathrm{m}^2$ in steps of $0.1\,\mathrm{A}/\mu\mathrm{m}^2$.

As explained above, a further increase of the current density leads to the onset of a new precessional regime characterized by out-of-plane precessional states (see Figs. 23, bottom). The power spectrum density in this regime is displayed in Fig. 30. As expected from 0K simulations, out-of-plane precessional states are characterized by a blueshift in frequency with increasing current density with, roughly speaking, a $\frac{1}{2}$ power law dependence of the frequency vs. current density. It is noteworthy that in this regime the PSD's associated with m_x or m_y are indistinguishable, a property that might help in establishing a clear separation between precessional states in the "low" and "high" current regimes (in other words, the PSD should remain essentially independent from the exact orientation of the applied field in the vicinity of the easy magnetization axis).

Remarkably enough, many of the predictions of the simple single spin approximation have clear transcriptions in the room temperature point-contact experiments of Rippard et al. [30]. The existence of a redshift and a blueshift regime has been clearly identified, although the latter has only been observed under high perpendicular applied field ($> 0.6\,\mathrm{T}$). Similarly, precessional states in the redshift regime have been observed only for easy axis fields exceeding a threshold ($50\,\mathrm{mT}$) well above any estimated effective anisotropy field in these systems. At large applied fields, frequency domain measurements of the magnetoresistance (reported in units of $\mathrm{V/Hz}^{1/2}$) show extremely narrow magnetoresistance peaks that behave at least qualitatively similarly to PSD's shown in Figs. 28-29. MR spectra do imply some mixing between f and $2f$ contributions, the source of which has been attributed to misalignment between the magnetization directions at equilibrium under field within the reference and free layers. It is generally estimated that a misalignment of less than $10°$ proves sufficient to restore PSD's of comparable magnitude for the fundamental frequency and its first harmonics. Higher harmonics have not been observed but, clearly, theoretical expectations ought to be convoluted with the experimental spectral bandwidth and take into account detailed features of the magnetoresistance response such as shown in Fig. 14. On the other hand, a major discrepancy between experimental data and theoretical expectations appears as soon the temperature is raised in the simulations: the line width grows with roughly the square root of the temperature reaching typical values around 300 MHz at 77 K and some 700 MHz at 300 K for a damping parameter still equal to its nominal value as extracted from e.g. an FMR experiment. Now, raising the anisotropy will mainly affect the resonance frequency at the onset of precessional states, but not so much the line width that remains essentially controlled by the damping parameter. It thus turns out that a few tens of MHz full width at half maximum at room temperature requires an effective damping parameter in the 10^{-4} range, the origin of which remains mysterious at this stage.

The experiments of Rippard et al. [30] use a lithographically defined point contact with continuous magnetic films (see Fig. 1). The exchange coupling of the dynamic part of the system to an extended magnetic film raises doubts on the applicability of the macrospin approximation. The experiments of Kiselev et al. [28, 124], on the other hand, use a nanopillar geometry with a finite free layer. We expect the macrospin model to be a better approximation for these samples. Unfortunately, the results complexity extends far beyond macrospin predictions, calling for full micromagnetic simulations.

4.5 The micromagnetic regime

In contrast to the single spin approximation, micromagnetics allows for non uniform magnetization distributions across the area (and thickness) of both the free and hard layers elements. As stressed in section 4.1, the magnetization now becomes a function of position within a given element and is subject to the spin transfer torque as well as to the action of an effective field, itself a function of the magnetization distribution. Both the spin transfer torque and the effective field are thus position dependent within the considered element (see Eqs. 29 or 32). Excitations such as spin- or magnetization waves are now allowed within the elements of the stack. Moreover, the effect of the Oersted field may now be taken into account.

There have been a number of calculations using this approach [125, 126, 127, 15, 128, 129, 130, 131, 132]. These have clarified some of the discrepancies between measurements and macrospin simulations. In particular, Lee et al. [15] have shown that in the region where experiments show the "W" phase, the magnetization is far from uniform. Vortices enter and leave the system reducing the resistance from the full antiparallel value without exhibiting well defined precession. Berkov and Gorn [132], have shown that a postulated distribution of local anisotropies qualitatively reproduces the current dependence of the precession frequency and linewidth seen in experiments of Kiselev et al. [28]. While full micromagnetic simulations do a better job describing the behavior of the system, they do it with a greater degree of uncertainty because many unmeasured details of the system are important, included among these are the exchange stiffness and saturation magnetization, the distribution of anisotropies, the details of the shape, particularly the edges of the sample, etc.

Even for a perfectly characterized sample, however, micromagnetics alone does not provide a fully consistent model of spin transfer induced excitations and switching since, up to this date, it has not been twinned with a truly 3D transport model [101, 102]. So far, micromagnetics calculations have relied on 1D transport theory for the evaluation of the spin transfer torque. Additional approximations are often made. In most instances, micromagnetic simulations rely on the assumption of a uniform and static magnetization distribution within the hard (pinned) layer as well as a uniform current density across the element. It is often further assumed that the polarization $\mathcal{P}(\mathbf{r})$ is constant, irrespective of the relative orientations of the magnetization within the hard and soft elements . According to the results of section 3.7, lateral diffusion and rescattering are anticipated to have a stabilizing effect for a net electron flow from the free layer into the adjacent non-magnet and a destabilizing effect in the reverse geometry. Owing to prevailing conventions, lateral diffusion and rescattering would thus be anticipated to improve and degrade spatial coherence for the P-AP and AP-P transitions, respectively.

We start this section by considering the fate of precessional states ($H_x > H_{\mathrm{K}}$) within small elements when shifting from the single spin approximation to the full micromagnetic regime [131]. These states are substantially the same but there are important differences between the two descriptions. At low current densities and room temperature, power is emitted at basically constant frequency within a well defined current density span. Two peaks in the power spectrum density extracted from the time variation of $\langle m_y \rangle$, i.e. the m_y magnetization component averaged over the volume of the element, are observed. They correspond to two vibration eigenmodes of elliptical elements [133] as depicted in Fig. 31a. The largest emitted power corresponds

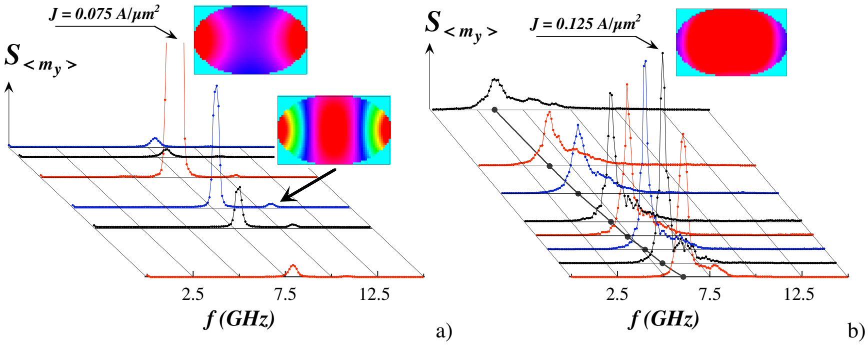

Fig. 31. Micromagnetic regime: $\langle m_y \rangle$ power spectrum density vs. current density at 300 K for $H_x = 3\,H_\mathrm{K}$. a) Low current density regime ($J = 0.025, 0.05, 0.06, 0.075, 0.085, 0.09\,\mathrm{A}/\mu\mathrm{m}^2$); Insets: eigenmodes at 8.2 and 11.2 GHz. b) Redshift regime at higher current densities ($J = 0.1, 0.125, 0.150, 0.175, 0.2, 0.25, 0.3, 0.4\,\mathrm{A}/\mu\mathrm{m}^2$); Inset: spatial PSD distribution at 5.4 GHz ($J = 0.125\,\mathrm{A}/\mu\mathrm{m}^2$). $\mathrm{Ni}_{80}\mathrm{Fe}_{20}$ like materials parameters (Exchange constant: $A = 1.0\,10^{-11}$ J/m, saturation magnetization $M_S = 800$ kA/m, damping parameter $\alpha = 0.01$). Elliptical free element: thickness $d = 2.5$ nm, long and short axes 115 nm and 70 nm, respectively. For this set of material parameters and dimensions, the shape induced anisotropy field amounts to ≈ 19.5 kA/m (≈ 245 Oe). After [131]

to a mode characterized by enhanced in-phase magnetization precession in the vicinity of the apices of the elliptical element . For this mode, the emitted power first grows with increasing current density, then decreases. Worth noticing is the fact that the characteristic frequencies of these eigenmodes differ from Kittel's frequency (8.2 and 11.2 GHz for the former vs. 9.18 GHz for the latter for the dimensions and material parameters considered). Over a large current density range beyond a second current threshold, (Fig. 31b), the PSD vs. current density exhibits the redshift behavior also characteristic of the single spin approximation for $\chi > \chi_{crit.}$ (cf Eq. 48). In the redshift regime, precessional states correspond to an essentially coherent precession of the magnetization within the central zone of the element as illustrated in the inset of Fig. 31b. Results contained in Fig. 31 are, qualitatively at least, consistent with the experimental results of Kiselev et al. (notably Figs. 1c and d in [28]). The results above differ from the simulation data of Lee et al. [129] who found that precessional states could only be maintained over a very narrow current density range for fields typically equal to $3\,H_\mathrm{K}$ in Co elements. Actually, in their respective attempts to fit Kiselev's et al. experiments, Lee et al. [129] and Berkov and Gorn [132] rely on markedly different assumptions with respect to material parameters (exchange stiffness, existence or not of a depressed saturation magnetization) and microstructure. These analyses also differ in the conversion of the time dependent micromagnetic magnetization distributions into a measurable GMR signal (Berkov and Gorn apply the field along a rather skewed direction with respect to the ellipse long axis, Lee et al. do not). Altogether, assuming that all of the simulations referred to above are technically sound, it seems clear that simulation results prove extremely sensitive to a wide range of parameters that remain only poorly known in these tiny magnetic elements.

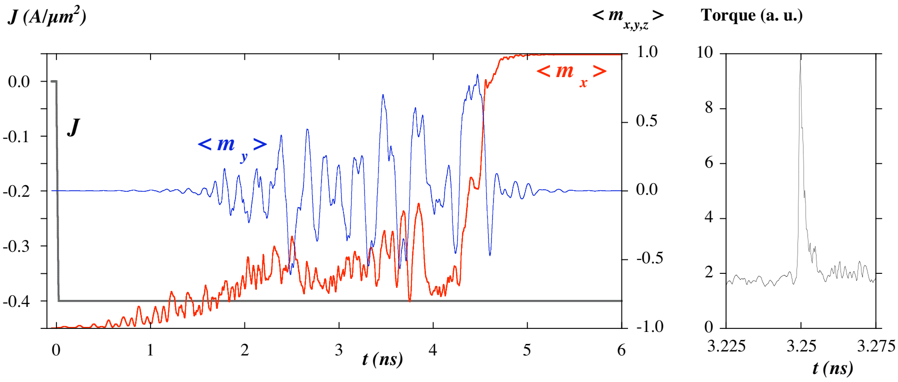

Fig. 32. Switching event in a $170 \times 80 \times 2.5\,\mathrm{nm}^3$ elliptical element at 0 K owing to numerical micromagnetics. Left: average magnetization components $\langle m_x \rangle$ and $\langle m_y \rangle$ *vs* time. Right: Torque spike linked to vortex pair annihilation. Current density: $J = -0.4\,\mathrm{A}/\mu\mathrm{m}^2$, polarization $\mathcal{P} = 0.3$. Co/CoFe like material parameters (Exchange constant: $A = 1.3\,10^{-11}$ J/m, saturation magnetization $M_S = 1500$ kA/m, damping parameter $\alpha = 0.006$).

We turn now to a micromagnetic switching event. For simplicity, we keep the fixed layer frozen and fix the spin current coming from it to the free layer, thus, the free layer is treated as a soft element flooded with a uniform density of spin-polarized electrons. The Oersted field is assumed to originate from an elliptical cross-section cylinder with height 50 nm meant to represent the pillar height with the soft layer located at half-height across the pillar. We further assume that the hard layer is left unpatterned so that the soft element is only subject to its self demagnetizing field, exchange interactions and the spin transfer torque with $\mathcal{P}(\mathbf{r})$ constant. Symmetry in the spin torque is lifted through the application of a minute constant field along **y**. The current is assumed to start flowing at time $t = 0$ and follow a simple step function. The current density is chosen to stand slightly above the switching threshold current density at zero temperature.

Three phases characterize the switching event. During the first phase, lasting about 1.5 ns, the average value of the transverse magnetization component $\langle m_y \rangle$ remains almost zero, as shown in Fig. 32. So does the $\langle m_z \rangle$ component. Due to the inhomogeneous magnetization and effective field distribution , including the Oersted field, the spin torque proves most efficient close to the apices of the elliptical element, leading to a beating between two mirror-symmetric C-type states (Fig. 33) with a period of $\approx$ 160 ps. Magnetization

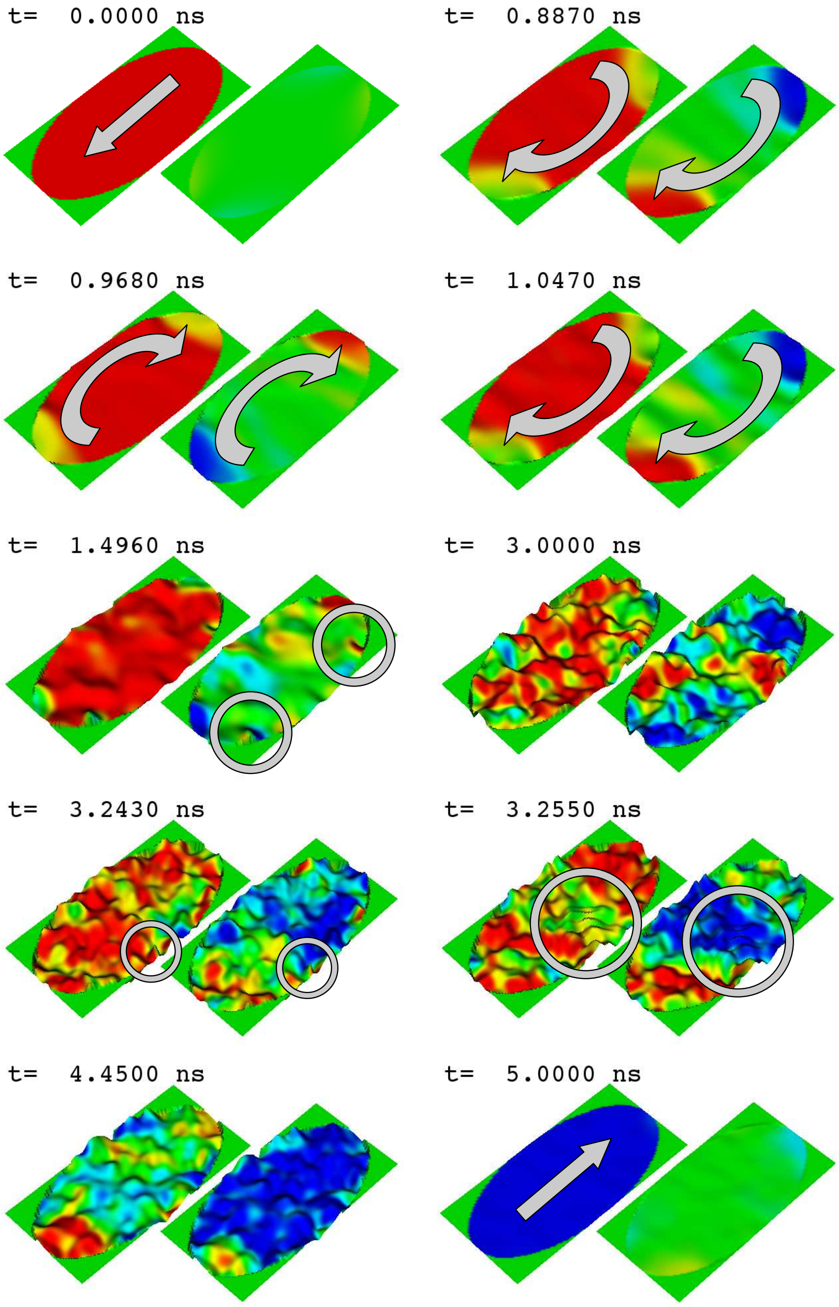

Fig. 33. Magnetization distribution *vs* time corresponding to Fig. 32 ($T = 0\,\mathrm{K}$). Color map extending from red (-1) to blue ($+1$) for the m_x and m_y magnetization components (the left and right image of each images pair, respectively). The surface of the element distorts according to the sign and amplitude of the m_z magnetization component. See text for details.

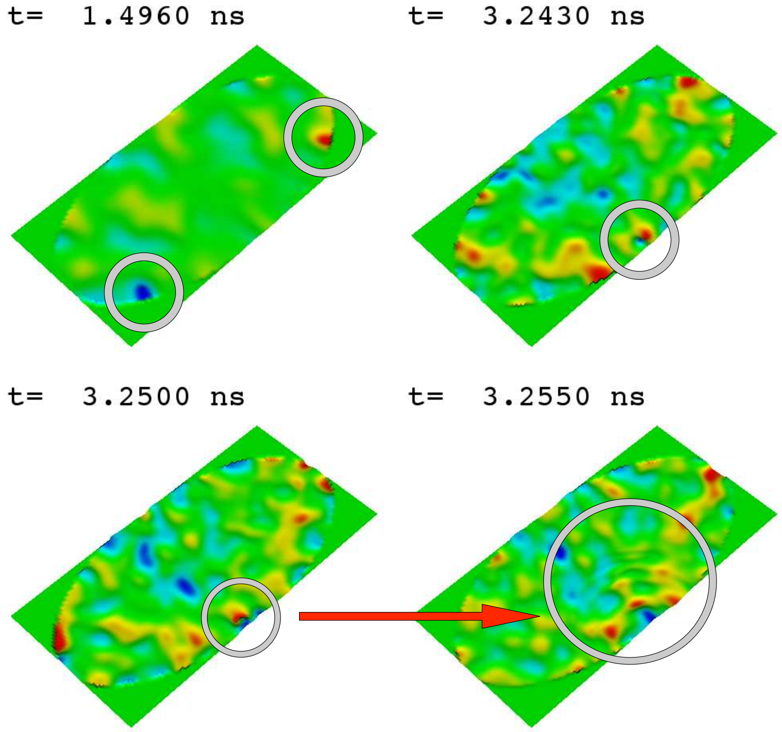

Fig. 34. Vortex nucleation $t = 1.496\,\text{ns}$ and pair annihilation (starting at $t = 3.243\,\text{ns}$) during the switching event described in Fig. 33. Color representation and surface distortion according to the sign and amplitude of the m_z magnetization component. Note the extremely sharp transition between the blue and red colors within the grey circle for $t = 3.25\,\text{ns}$, followed by the emission of a magnetization wave for $t = 3.255\,\text{ns}$.

waves develop smoothly ($t = 1.0 - 1.5\,\text{ns}$). When t reaches $1.496\,\text{ns}$, the first vortex pair is nucleated along the lower rim of the element (see Figs. 33 and 34).

During the second phase, the magnetization motion becomes complicated with extreme excursions of both the m_y and m_z components between -1 and $+1$, as displayed in Fig. 33 ($t = 2.5 - 4.4\,\text{ns}$). However, the average transverse magnetization component $\langle m_y \rangle$ undergoes globally increasing oscillations away from its ground state. This phase is equivalent to the parametric pumping phase characteristic of the single spin model.

Switching, the third phase, only occurs if partial resynchronization takes place ($t = 4.45\,\text{ns}$, Fig. 33). This feature is quite general. With increasing current density, sub-ns switching speeds may be achieved in simulations, in agreement with experiments [134]. However, prior to switching, the element still contains winding vortex-antivortex pairs indicated e.g. by the grey circles in Figs. 33 and 34 for $t = 3.243\,\mathrm{ns}$ that are seen to decay through the emission of magnetization waves ($t = 3.255\,\mathrm{ns}$ in Figs. 33 and 34). In most instances, the annihilation process manifests itself through a sharp peak in the maximum torque recorded across the simulation area (see Fig. 32, right). Vortex pairs are termed winding if both the circulation of the magnetization and the core magnetization [135] change sign between the elements of the pair so that the magnetization would rotate by 360° along a line joining the vortex cores. The annihilation of such a vortex pair would normally imply the nucleation and propagation of a Bloch point.

Although numerical micromagnetics can be done in a sophisticated enough manner to treat Bloch points rather satisfactorily [136], annihilation of winding vortex-pairs is usually a numerical artifact [137], especially when the simulation mesh implies a single plane of nodes in these very thin elements. If such structures in the magnetization do occur, the fine details of the simulation become unreliable as the results become strongly mesh and time-step dependent, even at zero temperature. Readers are in this respect cautioned to examine all simulations of spin transfer induced dynamics critically.

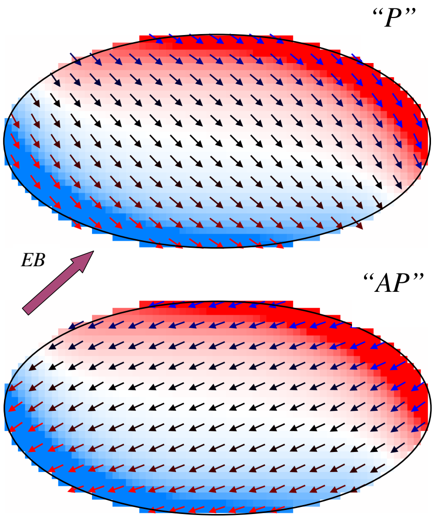

Fig. 35. "P" and "AP" states of a fully patterned elliptical pillar exchange biased at a skewed angle. Soft and hard elements dimensions: $130 \times 65 \times 2.5\,\mathrm{nm}^3$; spacer thickness: 5 nm. Biasing direction EB at 45°. $\mathrm{Ni}_{80}\mathrm{Fe}_{20}$ type material parameters. The background color coding follows the m_z magnetization component and is determined solely by the demagnetization field from the biased fixed layer, and hence does not differ much between the two states. Note however, that in the "AP" state the magnetization is largely antiparallel to the fixed layer while in the "P" it is almost perpendicular.

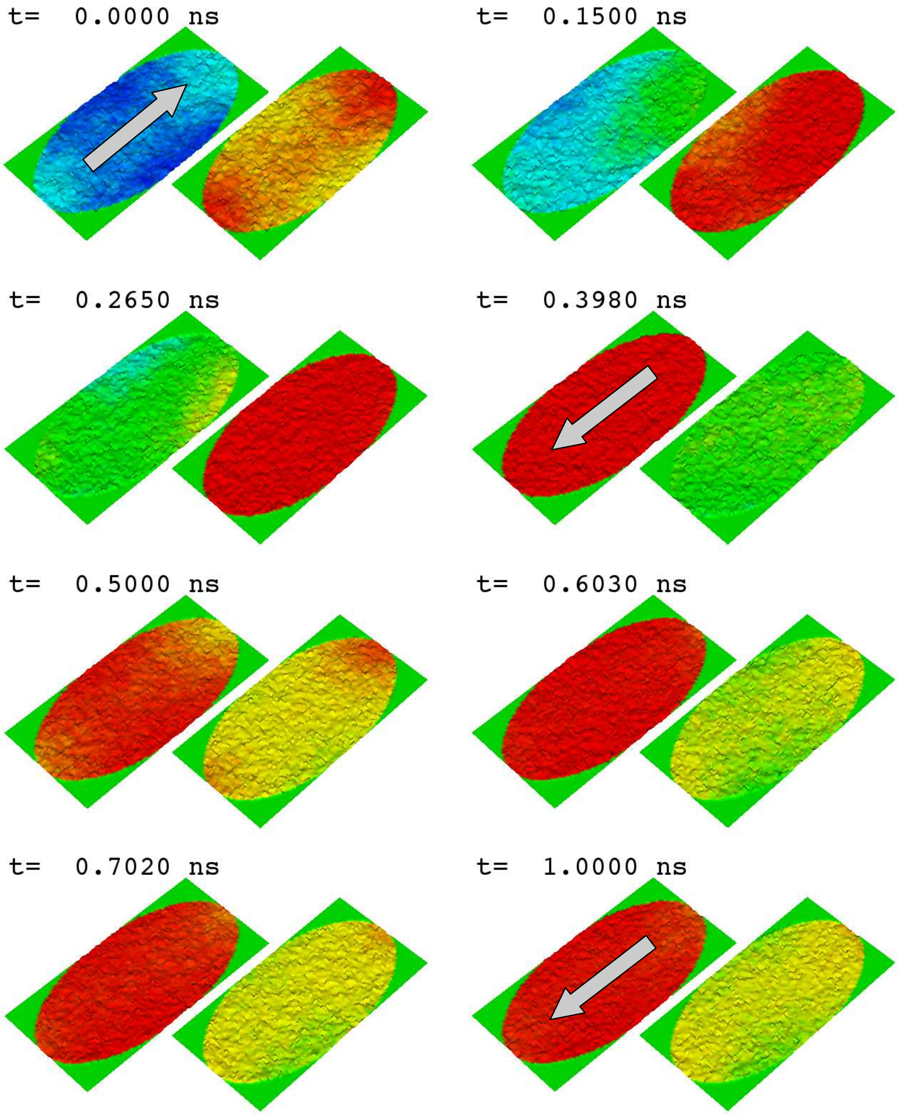

Fig. 36. Typical switching event in a $130 \times 65 \times 2.5\,\mathrm{nm}^3$ elliptical element with the hard layer fully patterned and biased at a skewed angle. Micromagnetic simulations at 20 K. $\mathrm{Ni_{80}Fe_{20}}$ like material parameters (damping parameter $\alpha = 0.01$). Same representation conventions as in Fig. 33. Switching at $t = 0.265\,\mathrm{ns}$. Subsequent $\langle m_y \rangle$ maxima and minima at $t = 0.398, 0.603$ and $t = 0.5, 0.702\,\mathrm{ns}$, respectively. Note that thermal fluctuations at time $t = 0$ and $t = 1\,\mathrm{ns}$ appear dissimilar: the current still flows at $t = 1\,\mathrm{ns}$ and enhances damping

Fortunately, a markedly different picture emerges from exchange-biased stacks whereby the biasing direction is set at an angle with respect to the shape

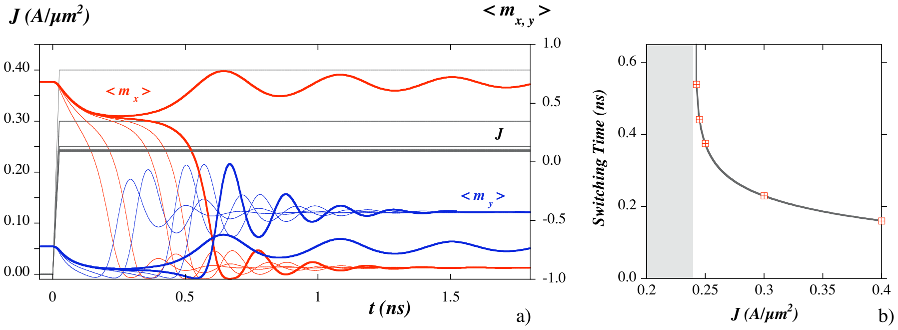

Fig. 37. a) Switching trajectories as a function of current density at 0 K owing to numerical micromagnetics. Dimensions and material parameters identical to those in Fig. 36. The thick lines show trajectories across the current density bifurcation threshold $0.2425 > J > 0.24\,\mathrm{A}/\mu\mathrm{m}^2$. b) Switching time vs. current density. The switching time is defined as the time for which $\langle m_x \rangle = 0$. Current densities: $J = 0.4, 0.3, 0.25, 0.245, 0.2425, 0.24\,\mathrm{A}/\mu\mathrm{m}^2$.

induced easy magnetization axis. We therefore now consider a fully patterned stack composed of an exchange-biased "hard" layer, a normal metal spacer and a free layer, all with an identical elliptical cross section. In our model calculations, the biasing direction is set at an angle of +45° with respect to the long axis of the elliptical hard layer element, the magnetization of which we assume to be uniform. The free element is now subject to a rather large demagnetizing field that enforces two noticeably asymmetrical magnetization distributions at equilibrium: for the dimensions considered, the magnetization distribution within the free element is oriented at a mean angle close to −155° (almost opposite) for the "AP" configuration, but at −45° (almost perpendicular rather than parallel) for the "P" configuration (see Fig. 35). Due to biasing at a skewed angle, the potential wells for the "P" and "AP" states are also strongly asymmetrical giving a much easier "P" to "AP" transition as compared to the "AP" to "P" transition. Also due to the shallow potential well of the "P" state, spontaneous "P" to "AP" transitions are observed in numerical simulations for temperatures as low as 40 K. At 20 K on the other hand, $\langle m_y \rangle$ undergoes $\approx 6°$ to 7° peak to peak thermal fluctuations that do not prove large enough to jeopardize the long term stability of the "P" state. A typical "P" to "AP" switching event is depicted in Fig. 36.

The skewed biasing causes the greater simplicity of the switching event in Fig. 36 as compared to that in Fig. 33. The large angle between the fixed layer and free layer magnetizations provides a substantial spin transfer torque the instant the current is switched on. This shortens or eliminates the growing oscillation phase illustrated in Fig. 32. The major features of the reversal process are, i) the existence of weak thermal fluctuations at the temperature considered, ii) an essentially coherent magnetization rotation that takes place within less than 1 ns, iii) the existence of post-switching oscillations that decay

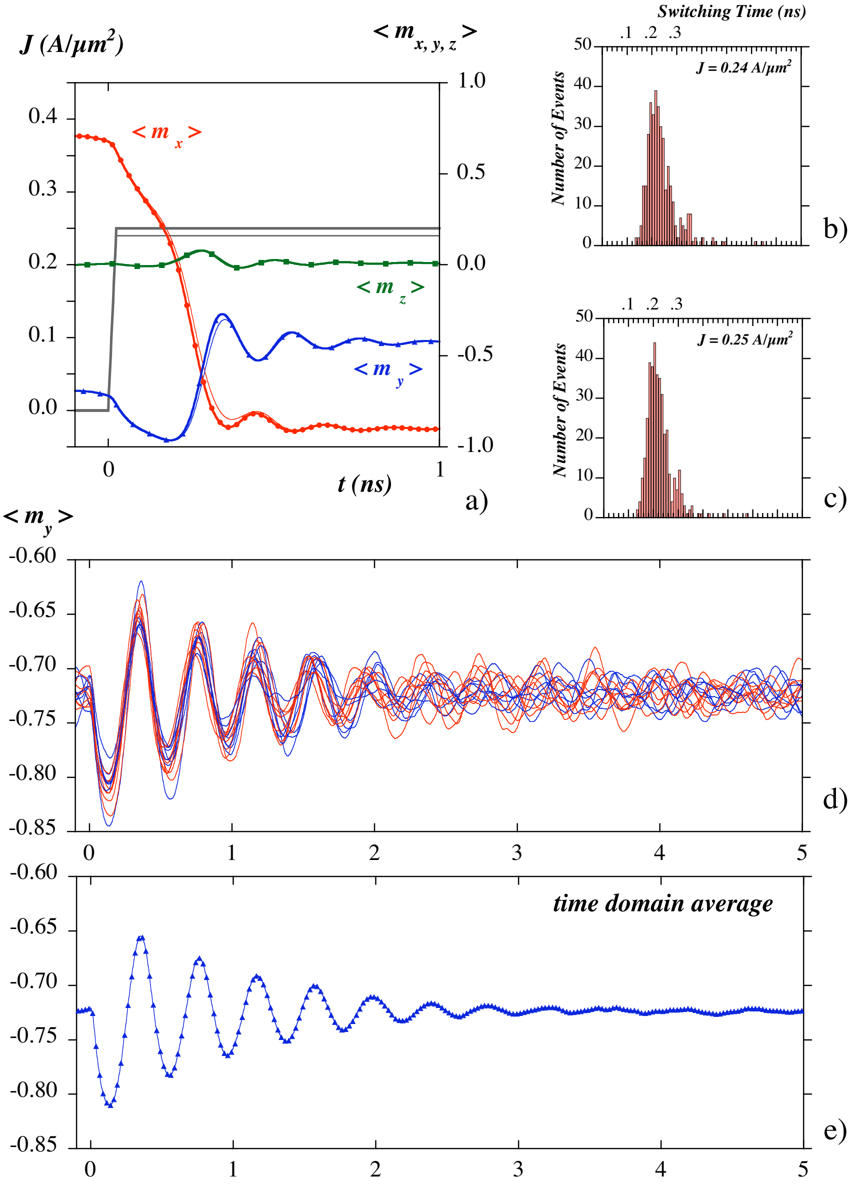

Fig. 38. Full scale micromagnetics for a hard layer biased at a skewed angle: a) time domain averages of "P" to "AP" switching trajectories at 20 K for current density $J = 0.24$ (thin lines) and $0.25\,\mathrm{A}/\mu\mathrm{m}^2$ (full symbols). Over 400 simulated trajectories, 19 (14) failed to display switching within the maximum allowed time for switching in the simulations, namely 10 ns, for $J = 0.24$ (0.25) $\mathrm{A}/\mu\mathrm{m}^2$; b and c) corresponding switching time histograms; d) selected $\langle m_y \rangle$ vs. time trajectories in the sub-critical regime at 4.2 K; e) time domain average over 100 trajectories such as shown in d).

over times also less than 1 ns. Similar features may be observed in Fig. 37 depicting $\langle m_{\mathrm{x,y}} \rangle$ vs. time at zero temperature with the current density as a parameter.

Coherence in the time domain is emphasized in Fig. 38a that displays an average over 400 trajectories of $\langle m_{\mathrm{x,y}} \rangle$ vs. time for two values of the current density. Very remarkably, the essential characters of a switching trajectory at zero temperature are preserved. The corresponding switching time histogram is shown in Fig. 38b-c; unsurprisingly, the histograms prove rather narrow. It may also be shown that coherence in the time domain is similarly preserved for low current density excitations (Fig. 38d-e), in particular in the sub-critical regime, i.e. for current densities below the onset of precessional states. Although no attempt was made to reproduce the experimental data of Krivorotov et al [138], micromagnetic simulations permit a qualitative understanding of these results. Still, a proper description of correlated data in the time and frequency domains owing to conventional micromagnetics appears almost out of reach because of the extremely narrow line widths extracted from the experiments.

Two additional remarks deserve to be made, namely i) fully patterned pillars with skewed exchange-biasing do, when viewed from a micromagnetic perspective, allow for extremely coherent magnetization rotation, at least for a “P” to “AP” transition, in a way that is conceptually very similar to spin-transfer induced switching in systems with a fourfold shape anisotropy [125], ii) precessional states may in such systems be excited for fast rising currents with both positive or negative current densities whether starting from the “P” or the “AP” state, a fact directly linked to the non-collinearity between the mean magnetization direction and the electrons spin-polarization.

Altogether, this section shows that the behaviors observed in experiment can be qualitatively explained by the torque originally proposed by Slonczewski. However, all of the calculations described here have ignored many of the features of the spin transport calculations, that is, the polarization $\mathcal{P}$ in Eq. (28) has been treated as a constant, and the angular dependence described in Eq. (26) has been ignored. So far, the comparison between experiments and simulations appears to be somewhat insensitive to the details of the polarization, at least given the other uncertainties about the systems. Only the size of the polarization has been important, and that can only be determined from experiment if the size of the damping is accurately known. It appears that the best possibility for testing the results of calculations like those in Sec. 3 is in measurements of biased samples with $\mathrm{Ni_{80}Fe_{20}}$ free layers. $\mathrm{Ni_{80}Fe_{20}}$ layers have smaller fluctuations in local anisotropies and biased samples appear to behave like macrospins in micromagnetic simulations. The recent measurements of Smith et al. [98] are significant progress in this direction.

5 Summary

Since the concept of spin transfer torques was first proposed by Slonczewski and Berger, there has been remarkable experimental and theoretical progress. Experiments have observed and characterized a variety of different behaviors including hysteretic switching, precession, and two level fluctuations. In this chapter we have tried to review the physical picture that has been developed to explain this variety of behaviors.

A generally accepted description of these systems has evolved from a hierarchy of models based on a separation of time and length scales. At the most basic level, quantum mechanical calculations describe the behavior of electrons spins close to the interface between ferromagnetic and non-magnetic layers. The exchange interaction in the ferromagnet rotates non-collinear spins in complicated ways. Calculations of this effect show that the component of the spin current along the magnetization is conserved as electrons transmit through and reflect from the interface. However, the transverse component of the incident spin current is effectively absorbed close to the interface and transferred to the magnetization. This absorption of the transverse spin current is the origin of the torque that drives the magnetization dynamics measured in these systems.

In such systems, any quantum mechanical coherence due to multiple scattering from interfaces tends to be washed out. The lack of coherence allows the results of the quantum mechanical calculations calculations to enter as boundary conditions into semiclassical transport calculations, which is the next level in the hierarchy of models. The semiclassical calculations give the spin currents flowing through the different layers and the torques on the magnetizations. A variety of semiclassical transport equations, the Boltzmann equation, the drift-diffusion equation, and circuit theory all give qualitatively the same result. The magnitude of the torque depends on the polarization of the current flowing from the fixed layer to the free layer, and the polarization of the current depends on everything in the sample within a few spin diffusion lengths, both upstream and downstream. This dependence leads to the result that the torque for small deviations away from antiparallel alignment is generally much stronger than the torque for equivalent deviations away from parallel alignment. These two consequences are the important observable predictions of the transport calculations.

The electron velocities are high enough and spin flip scattering lifetimes short enough that from the point of view of transport, the magnetization can be thought of as fixed. This separation of time scales allows the torques to be computed for fixed magnetic configurations and the resulting torques then used to describe the magnetization dynamics. Macrospin or micromagnetic simulations of the dynamics are the final level of model in the hierarchy. Macrospin models accurately describe the system when the magnetization remains uniform throughout the sample. The resulting behavior separates naturally into two regimes depending on the size of the applied field.

For applied fields less than the coercive field of the free layer the system is stable in either a parallel or antiparallel alignment. For large electron flow from the fixed layer to the free layer, the stable alignment is parallel and for electron flow in the opposite direction it is antiparallel. There is a region of bistability for small currents. The transitions from one stable region to the other are preceded by a small region of in-plane precession. In-plane precession describes a state in which the magnetization precesses around the easy axis, which lies in-plane. As the transition to the opposite configuration is approached, the amplitude of the precession gets large, with a substantial out-of-plane component. For applied fields larger than the coercive field, the applied field inhibits switching because the antiparallel state is never stable. Instead, with increasing electron flow from the free into the fixed layer, the system goes from parallel through the in-plane precession region into an out-of-plane precession configuration.

At finite temperature, the transitions between the different configurations become statistical rather than deterministic. The transitions can be modelled either through direct integration of the Landau-Lifshitz-Gilbert equation including a term to generate thermal fluctuations or through modified barrier crossing models. In this chapter we briefly described transition time distributions for cases in which the switching time is not impractically long. In some regimes, particularly for high fields, the effective barrier in both directions is sufficiently small that the systems can make thermally driven transitions in both directions. Then the magnetization exhibits two level fluctuations with the associated low frequency noise in the resistivity.

Full micromagnetic simulations, in which the magnetization is allowed to become non-uniform, show that the magnetization does indeed become non-uniform. These simulations show that non-uniform dynamics may explain some of the discrepancies between the predictions of the macrospin model and experiment. Unfortunately, the results of the simulations are sensitive to many unmeasured details of the sample, so that such simulations are simply suggestive rather than rigorously conclusive.

Taken together, the theoretical work described in this review suggests that the form of the torque originally envisioned by Slonczewski is capable of explaining the experimentally observed phenomena. However, the confirmation is not yet quantitative. There is only limited experimental observations that confirm the detailed angular dependence of the torque as predicted by a series of transport calculations. In fact, all of the micromagnetic simulations to date ignore these details. One reason it is difficult to quantitatively test the model is the variability from sample to sample. Samples are still difficult enough to fabricate that the results from nominally identical samples differ substantially in detail. Detailed testing of models will probably depend on experimental developments that allow sufficient characterization of the samples to constrain the theoretical models.

Additional theoretical developments may be necessary. For example, it may be necessary to integrate a fully three dimensional transport calculation with the micromagnetics in order to describe the non-uniform dynamics. The standard form used to describe damping in all of the calculations is phenomenological. A more accurate form may be necessary to describe the precessing states in these systems. Finally, when the models are quantitatively tested, they may not be consistent with the measured results, necessitating and driving a deeper understanding of the behavior of spins in magnetic multilayers. [2]

Acknowledgements: J. M. gratefully acknowledges enlightening discussions with André Thiaville, Gonçalo Albuquerque and Benoit Montigny. He also thanks G. Albuquerque and Yoshinobu Nakatani for assistance with advanced graphics. M. S. thanks his collaborators Andrew Zangwill and Jiang Xiao with whom most of his understanding has been developed. He also thanks Gerrit Bauer, Arne Brataas, and Yaroslav Tserkovnyak for informative discussions on spin pumping. Both thank Robert McMichael, Stephen Russek, André Thiaville and Andrew Zangwill for critical readings of the manuscript.

A Drift-Diffusion Solution for a Single Interface

In the non-magnet, the spin accumulation decays away from the interface with a length given by the spin accumulation length

$$s_z(x) = s(0)\exp[x/l_{\rm sf}^{\rm NM}]. \tag{53}$$

According to Eq. (16), the gradient of this spin accumulation determines the spin current in the non-magnet. In the ferromagnet, the spin accumulation also decays away from the interface

$$\delta s(x) = \delta s(0)\exp[-x/l_{\rm sf}^{\rm FM}]. \tag{54}$$

However,the spin current also depends on the total current because the conductivity is spin dependent. Using Eq. (18) and adjusting the internal electric field so that the total current is constant and there is no charge accumulation, the spin accumulation and the spin current satisfy

$$Q_{zx}(x) = P_\sigma \frac{\hbar}{2} j - D_z \nabla_z \delta s(x), \tag{55}$$

where $D_z = (D_\uparrow \sigma_\downarrow + D_\downarrow \sigma_\uparrow)/(\sigma_\uparrow + \sigma_\downarrow)$. See Ref. [67] for more details. The bulk equations give relations between the spin accumulation and the spin current at the interface

$$\begin{aligned} 0 &= -Q_{zx}(0) - \frac{D}{l_{\rm sf}^{\rm NM}} s_z(0) \\ 0 &= P_\sigma \frac{\hbar}{2} j - Q_{zx}(0) + \frac{D_z}{l_{\rm sf}^{\rm FM}} \delta s(0). \end{aligned} \tag{56}$$

---

[2] Completed on June 15, 2005 .

In the absence of spin flip scattering, the longitudinal spin current is conserved across the interface.

Equation (19) gives the boundary conditions for the spin currents and spin electrochemical potentials. The latter are related to the spin accumulation through the densities of states

$$\delta s = \frac{\hbar}{2}(\mathcal{N}_\uparrow \mu_\uparrow - \mathcal{N}_\downarrow \mu_\downarrow), \tag{57}$$

where $\mathcal{N}_\uparrow = (\partial n/\partial \mu)_\uparrow$. In the bulk, the internal electric field adjusts itself so there is no charge accumulation. However, we must include the dipole layer that develops across the interface when a current is flowing. We do this by allowing for charge accumulation in the ferromagnet just at the interface, but then ignore this charge accumulation for the behavior away from the interface. The interface dipole is specified through

$$\delta n(0) = \mathcal{N}_\uparrow \mu_\uparrow + \mathcal{N}_\downarrow \mu_\downarrow. \tag{58}$$

The boundary conditions in terms of densities and currents are then

$$\begin{aligned} \frac{\hbar}{2} j_x &= C_1 \frac{\hbar}{2} \delta n(0) + C_2 \delta s(0) - C_3 s_z(0) \\ Q_{zx}(0) &= C_2 \frac{\hbar}{2} \delta n(0) + C_1 \delta s(0) - C_4 s_z(0) \end{aligned} \tag{59}$$

The coefficients are

$$\begin{aligned} C_1 &= \frac{1}{2}\left(\frac{1}{R_\uparrow \mathcal{N}_\uparrow} + \frac{1}{R_\downarrow \mathcal{N}_\downarrow}\right) \qquad & C_3 &= \frac{1}{2}\left(\frac{1}{R_\uparrow \mathcal{N}} - \frac{1}{R_\downarrow \mathcal{N}}\right) \\ C_2 &= \frac{1}{2}\left(\frac{1}{R_\uparrow \mathcal{N}_\uparrow} - \frac{1}{R_\downarrow \mathcal{N}_\downarrow}\right) \qquad & C_4 &= \frac{1}{2}\left(\frac{1}{R_\uparrow \mathcal{N}} + \frac{1}{R_\downarrow \mathcal{N}}\right) \end{aligned} \tag{60}$$

$\mathcal{N}$ is the per-spin density of states in the non-magnet. The two boundary conditions, Eq. (59) together with the boundary values of the bulk solutions, Eq. (56) give four equations in four unknowns which can be determined in terms of the specified current j_x. Then using the bulk solutions, Eq. (53) and Eq. (54) gives curves like those in Fig. 10.

The same procedure is used for collinear transport in more complicated structures. However, in each finite thickness layer the spin accumulation is a superposition of exponentials decaying in opposite directions. The same procedure is used for non-collinear transport as well, but needs to be augmented by the non-collinear boundary conditions, Eq. (20). Values for the parameters that enter such calculations are given in Ref. [67].

B Precession and spin transfer in phase space: Melnikov's method

Melnikov's method [114, 115] applies to weakly perturbed time periodic Hamiltonian systems for which unperturbed trajectories may be derived from the energy landscape. Material below owes much to the work of Valet, Serpico, Bertotti et al. [139, 140, 141, 142] although the following results have been derived independently. We first establish the nature of unperturbed trajectories with the energy as a parameter in the simple case of a zero applied field and show that the switching current is well described as the current that satisfies Eq. 35 for a specific trajectory of the unperturbed system. We then extend results obtained for $h_\mathrm{x}^\mathrm{a} = 0$ to the $h_\mathrm{x}^\mathrm{a} \neq 0$ case.

Eq. 38 together with the conservation of the modulus of $\mathbf{m}$ define stable magnetization orbits in the absence of damping, namely,

$$\begin{aligned} Q\left(1 - m_x^2\right) - 2m_x h_x^\mathrm{a} + m_z^2 = 2w \\ m_x^2 + m_y^2 + m_z^2 = 1 \end{aligned} \tag{61}$$

The velocity field reads:

$$\frac{d\mathbf{m}}{d\tau} = -\left[\begin{pmatrix} m_x \\ m_y \\ m_z \end{pmatrix} \times \begin{pmatrix} Qm_x + h_x^\mathrm{a} \\ 0 \\ -m_z \end{pmatrix}\right] = \begin{bmatrix} m_y m_z \\ -\left[(1+Q)\, m_x + h_x^\mathrm{a}\right] m_z \\ \left(Qm_x + h_x^\mathrm{a}\right) m_y \end{bmatrix} . \tag{62}$$

Magnetization directions where the torque vanishes define the fixed points for this problem. These are the parallel state, $m_x = 1$, labeled F_1; the antiparallel state, $m_x = -1$, labelled F_2; two points with $m_y = 0$ and $(1+Q)m_x + h_x^\mathrm{a} = 0$ (m_z can be positive or negative); and two points S_1 and S_2 with $m_z = 0$ and $Qm_x + h_x^\mathrm{a} = 0$ (m_y can be positive or negative). Depending on the applied field h_x^a, these points can be stable, unstable or saddle points. For zero applied field, F_1 and F_2 are both stable, S_1 and S_2 are saddle points, and the other two points are unstable.

Let us first look at unperturbed trajectories in the $h_x^\mathrm{a} = 0$ case. The energy relationship then simply reads

$$m_z^2 - Qm_x^2 = 2w - Q\,, \tag{63}$$

indicating that unperturbed trajectories are defined through the intersection of hyperbolic cylinders (63) with the unit sphere. The saddle points are now located at $m_y = \pm 1$ and all possible trajectories within the attraction basin of F_1 span the $(0,\, Q/2)$ energy range. Variables can easily be separated, and, e.g. one finds that $dm_y/d\tau$ may be expressed as:

$$\begin{aligned} &\frac{dm_y}{d\tau} = \sqrt{2w\,(1+Q-2w)}\,\sqrt{1 - \frac{1}{1+Q-2w} m_y^2}\,\sqrt{1 - \frac{Q}{2w} m_y^2} \\ &m_z > 0 \end{aligned} \tag{64}$$

Letting $u = \sqrt{Q/2w}\; m_y$, one obtains readily:

$$\frac{du}{\sqrt{1-u^2}\sqrt{1-k^2u^2}} = \sqrt{Q\,(1+Q-2w)}d\tau\,, \tag{65}$$

with $k^2(w) = 2w/Q\,(1+Q-2w)$. Thus,

$$\begin{aligned} \tau - \tau_0 &= \frac{1}{\sqrt{Q\,(1+Q-2w)}} \int_0^u \frac{du}{\sqrt{1-u^2}\sqrt{1-k^2u^2}} \\ &= \frac{1}{\sqrt{Q\,(1+Q-2w)}} F\left(\psi,\, k\left(w\right)\right) \end{aligned} , \tag{66}$$

where $u = \sin(\psi)$; $k \in [0,1]$ and $F(\psi,\, k)$ is the Elliptic integral of the First Kind. The period for any unperturbed trajectory within the specified energy span amounts to four times the time necessary for m_{y} to move from 0 to $m_y^{\mathrm{Max}} = \sqrt{2w/Q}$, namely,

$$\begin{aligned} T\left(w\right) &= \frac{1}{\gamma_0 M_{\mathrm{S}}} \frac{4}{\sqrt{Q\,(1+Q-2w)}} \int_0^1 \frac{du}{\sqrt{1-u^2}\sqrt{1-k^2u^2}} \\ &= \frac{1}{\gamma_0 M_{\mathrm{S}}} \frac{4}{\sqrt{Q\,(1+Q-2w)}} K\left(k\right) \end{aligned} , \tag{67}$$

where $K(k)$ is the Complete Elliptic Integral of the First Kind. Periodic orbits obeying (65, 66) (unperturbed system) in the vicinity of fixed point F_1 are shown in Fig. 39 (top). The velocity along such trajectories as deduced from Eq. 66 proves highly non-uniform in agreement with the results of numerical simulations (see Fig. 25a). When w increases towards $Q/2$, orbits pile-up against the heteroclinic orbits (they link two separate saddle points) forming an homoclinic cycle Γ^0 displayed as a red line in Fig. 39 (top) similar to the numerical results of Fig. 20. In addition, the period increases with w and diverges (the frequency drops to 0) when $w = Q/2$ as shown in Fig. 40. Conditions for the application of Melnikov's theory, a general perturbation theory, are now met, namely, the existence of a homoclinic orbit to a saddle point for $\alpha = \chi = 0$, the existence of a continuous family of periodic orbits within Γ^0 and the fact that the period is a differentiable function of the energy of the Hamiltonian system. Then, to order $\mathscr{O}(\alpha)$, there exist closed orbits of the perturbed system, the proximity of which to unperturbed orbits is governed by Melnikov's function G. In order to estimate the latter, it proves first convenient to rewrite Eq. 39 according to

$$\begin{aligned} \frac{d\theta}{d\tau} &= -\frac{1}{\sin\theta}\frac{dw}{d\phi} - \alpha\sin\theta\frac{d\phi}{d\tau} + \chi p_\theta \\ \sin\theta\frac{d\phi}{d\tau} &= \frac{dw}{d\theta} + \alpha\frac{d\theta}{d\tau} + \chi p_\phi \end{aligned} \tag{68}$$

Since we are interested in Hamiltonian trajectories, Eq. 68 readily transforms into

$$\begin{aligned} \frac{d\theta}{d\tau} &= -\frac{1}{\sin\theta}\frac{dw}{d\phi} + \alpha(-\frac{dw}{d\theta} + \frac{\chi}{\alpha}p_\theta) &&= f_1 + \alpha\, g_1 \\ \sin\theta\frac{d\phi}{d\tau} &= \frac{dw}{d\theta} + \alpha(-\frac{1}{\sin\theta}\frac{dw}{d\phi} + \frac{\chi}{\alpha}p_\phi) &&= f_2 + \alpha\, g_2 \end{aligned} \tag{69}$$

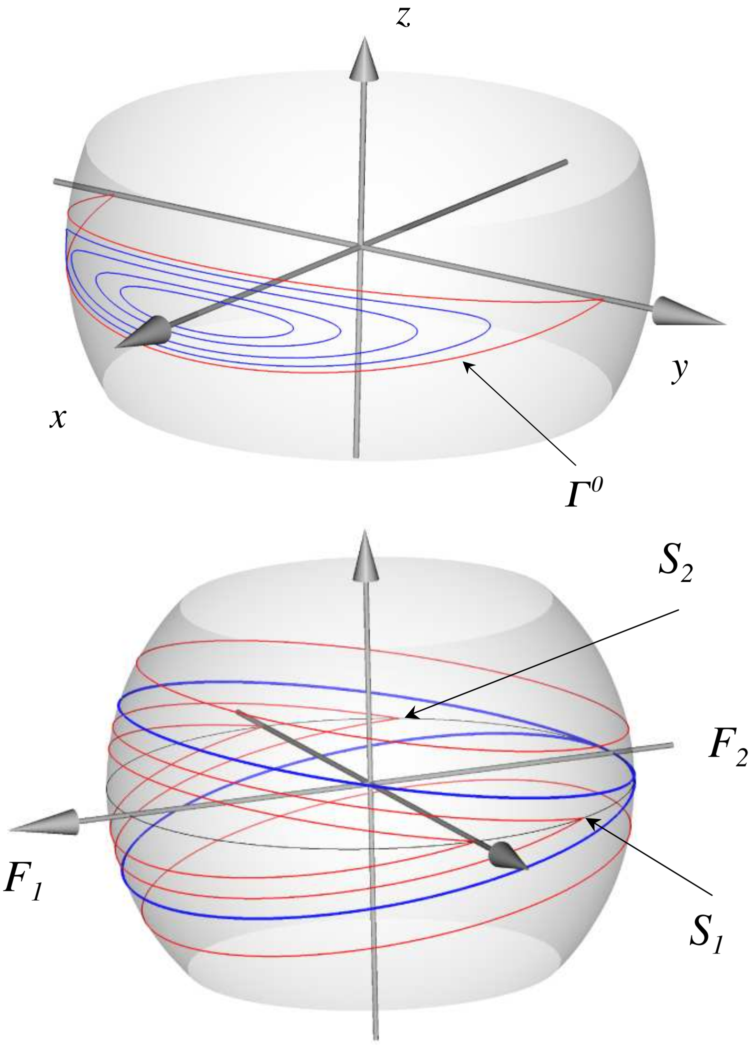

Fig. 39. Top: unperturbed trajectories for $w \in [0, Q/2[$; Bottom: homoclinic cycles ($h_x^{\mathrm{a}} \in [0, Q]$) and limit cycles ($h_x^{\mathrm{a}} > Q$) *vs.* reduced field $h_x^{\mathrm{a}} = 0, \frac{Q}{2}, Q, 3Q$. Eq.73 defines the corresponding reduced energies. S_1 and S_2 are the saddle points pertaining to the $h_x^{\mathrm{a}} = \frac{Q}{2}$ homoclinic cycle.

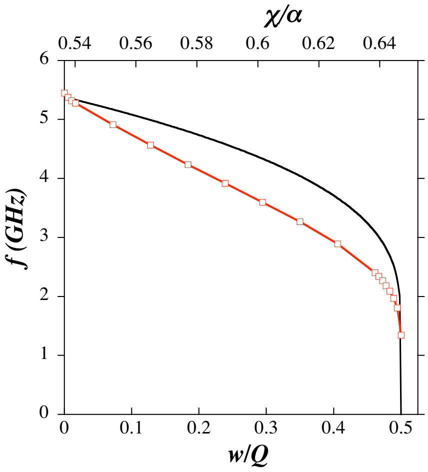

Fig. 40. Frequency for unperturbed orbits in the $w \in [0, Q/2]$ range in zero applied field. Also shown is the frequency of precessional states in the single spin approximation as a function of χ/α (open symbols) as determined by numerical simulation (single spin approximation).

Melnikov's function would, in the (θ, ϕ) plane, classically be built from Eq. 69 owing to $G\left(w, \frac{\chi}{\alpha}\right) = \int_0^T (f_1 g_2 - f_2 g_1)\, d\tau$, or

$$G\left(w, \frac{\chi}{\alpha}\right) = \int_0^{T(w)} \left[\left(\frac{d\mathbf{m}}{d\tau}\right)^2 - \frac{\chi}{\alpha}\left[\frac{d\mathbf{m}}{d\tau} \cdot (\mathbf{m} \times \mathbf{p})\right]\right] d\tau, \tag{70}$$

if a static variable could be associated with $\sin\theta \, \frac{d\phi}{d\tau}$. In the limit $\sin\theta \to 1$, a condition easily fulfilled due to the strong ellipticity of the Hamiltonian trajectories, $G\left(w, \frac{\chi}{\alpha}\right)$ is cleanly approximated by (70), a relation equivalent to (35), but now evaluated along an unperturbed trajectory with period $T(w)$.

It follows directly from the definitions above that the onset of precessional states should coincide with the current density that zeroes Melnikov's function for an infinitesimal unperturbed trajectory around F_1 whereas the critical current density for switching in zero applied field should coincide with the current that zeroes Melnikov's function for the unperturbed homoclinic cycle. Note that, for $w = Q/2$, one gets $m_z = \pm\sqrt{Q} m_x$, an equation defining planes in space, indicating that the homoclinic cycle is the locus of the intersection of the unit sphere with the above mentioned planes.

Although we have completely characterized the Hamiltonian trajectories in the case $h_x^{\mathrm{a}} = 0$, it actually proves unnecessary. Indeed, as noticed earlier [115, 140], the time integral in (70) may be written as a line integral owing to:

$$G\left(w, \frac{\chi}{\alpha}\right) = \oint_{\Gamma} \left[\left(\frac{d\mathbf{m}}{d\tau}\right) - \frac{\chi}{\alpha}(\mathbf{m} \times \mathbf{p})\right] \cdot d\mathbf{m} \tag{71}$$

Extension to the $h_x^{\mathrm{a}} \neq 0$ case is straightforward. With increasing h_x^{a} the saddle points S_1 and S_2 gradually move (Fig. 39, bottom) in the equatorial plane in the direction of the fixed point F_2, according to :

$$\cos\left(\phi^{\max}\right) = -\frac{h_x^{\mathrm{a}}}{Q} \tag{72}$$

Rewriting the energy expression yields $2w = Q\left(1 + m_x^2\right) + m_z^2$, or:

$$2w = Q + \frac{h_x^2}{Q}\,, \tag{73}$$

where $h_x \equiv h_x^{\mathrm{a}}$. Eq. 73 defines the relation between the applied field and the energy level for the homoclinic bifurcation. When w reaches Q (or, equivalently, h_x reaches Q), $\phi^{\max}$ reaches π, so that the two saddle points S_1 and S_2 merge at $m_x = -1$ (Fig. 39, bottom). Similar arguments hold true for $h_x < 0$ ($-Q \leq h_x \leq 0$) with the two saddle points S_1 and S_2 merging at $m_x = +1$ for $h_x = -Q$.

In summary, in the whole interval $-Q \leq h_x \leq Q$, the homoclinic cycle as a function of parameter $w\left(h_x\right)$ is defined as the intersection of the unit sphere with planes defined by

$$m_z = \pm\left(\frac{h_x}{\sqrt{Q}} + \sqrt{Q}m_x\right)\,, \tag{74}$$

and the critical current density for switching vs. h_x is defined as the current density that zeroes Melnikov's function (71) for the corresponding homoclinic trajectory. Proper parameterization of the homoclinic cycles allows for an analytical expression for the switching threshold (Eq. 51) in which ξ_S is a measure of the opening of the homoclinic cycle in the equatorial plane.

Altogether, Melnikov's method both establishes a clear distinction between the critical currents for the onset of precessional states and switching, and expresses the critical current for switching vs. applied field as the ratio of line integrals that may be evaluated analytically for the present simple energy ansatz. It also emphasizes the fact that $\frac{\chi}{\alpha}$ is the fundamental parameter of this particular non-linear dynamical system. Ultimately, within the framework of our simple energetics, Q stands as the only remaining free parameter in the reduced units of Fig. 22.

As h_x keeps growing beyond Q, the unique saddle point forces Hamiltonian trajectories to split into two subsets still satisfying relation (74), one above, the second under the equatorial plane (Fig. 39, bottom). For $h_x > Q$, however, Melnikov's theory may not be directly applied anymore, although it is still possible to look for solutions satisfying (71). The critical current density χ/α deduced from this approach is proportional to $\cong \frac{h_x}{Q}$ in the limit $Q \ll 1$, a result easily reached through application of Stoke's theorem to unperturbed out-of-plane orbits. It turns out that, for $h_x > Q$, the critical current density necessary to the onset of out-of-plane precessional states appears to be bound on the one hand by the current density that zeroes the Melnikov function G for the last homocline cycle $w = Q$ (curve labelled χ_2^{Lower} in Fig. 22) and on the other hand by the current density that zeroes G for the unperturbed out-of-plane orbit (curve labelled χ_2^{Upper}).

References

1. J. C. Slonczewski, J. Magn. Magn. Mater. **159**, L1 (1996); **195**, L261 (1999)
2. L. Berger, Phys. Rev. B **54**, 9353 (1996); J. Appl. Phys. **90**, 4632 (2001)
3. J. Slonczewski, United States Patent #5,695,864, Dec 9, (1997)
4. M. Tsoi, A. G. M. Jansen, J. Bass, W. C. Chiang, M. Seck, V. Tsoi, P. Wyder, Phys. Rev. Lett. **80**, 4281 (1998)
5. E. B. Myers, D. C. Ralph, J. A. Katine, R. N. Louie, R. A. Buhrman, Science **285**, 867 (1999)
6. J. E. Wegrowe, D. Kelly, Y. Jaccard, P. Guittienne, J. P. Ansermet, Europhys. Lett. **45**, 626 (1999); J. E. Wegrowe, D. Kelly, X. Hoffer, P. Guittienne, J. P. Ansermet, J. Appl. Phys. **89**, 7127 (2001); D. Kelly, J. E. Wegrowe, T. K. Truong, X. Hoffer, J. P. Ansermet, Phys. Rev. B **68**, 7947 (2003)
7. J. Z. Sun, J. Magn. Magn. Mater. **202**, 157 (1999)
8. J. A. Katine, F. J. Albert, R. A. Buhrman, E. B. Myers, D. C. Ralph, Phys. Rev. Lett. **84**, 3149 (2000)
9. J. Grollier, V. Cros, A. Hamzić, J.-M. George, H. Jaffrès, A. Fert, G. Faini, J. Ben Youssef, H. Le Gall, Appl. Phys. Lett. **78**, 3663 (2001); J. Grollier, V. Cros, H. Jaffrès, A. Hamzic, J.-M. George, G. Faini, J. Ben Youssef, H. Le Gall, A. Fert, Phys. Rev. B **67**, 174402 (2003); A. Fert, V. Cros, J.-M. George, J. Grollier, H. Jaffrès, A. Hamzić, A. Vaurès, G. Faini, J. Ben Youssef, H. Le Gall, J. Magn. Magn. Mater. **272-76**, 1706 (2004)
10. F. B. Mancoff, S. E. Russek, IEEE Trans. Magn. **38**, 2853 (2002)
11. W. H. Rippard, M. R. Pufall, T. J. Silva, Appl. Phys. Lett. **82**, 1260 (2003); M. R. Pufall, W. H. Rippard, T. J. Silva, Appl. Phys. Lett. **83**, 323 (2003)
12. S. Urazhdin, N. O. Birge, W. P. Pratt, J. Bass, Phys. Rev. Lett. **91**, 146803 (2003)
13. B. Özyilmaz, A. D. Kent, D. Monsma, J. Z. Sun, M. J. Rooks, R. H. Koch, Phys. Rev. Lett. **91**, 067203 (2003)
14. Y. Ji, C. L. Chien, M. D. Stiles, Phys. Rev. Lett. **90**, 106601 (2003)
15. K. J. Lee, Y. Liu, A. Deac, M. Li, J. W. Chang, S. Liao, K. Ju, O. Redon, J.-P. Nozières, B. Dieny, J. Appl. Phys. **95**, 7423 (2004)
16. J. Hayakawa, K. Ito, M. Fujimori, S. Heike, T. Hashizume, J. Steen, J. Brugger, H. Ohno, J. Appl. Phys. **96**, 3440 (2004)
17. M. Covington, M. AlHajDarwish, Y. Ding, N. J. Gokemeijer, M. A. Seigler, Phys. Rev. B **69**, 184406 (2004); M. Covington, A. Rebei, G. J. Parker, M. A. Seigler, Appl. Phys. Lett. **84**, 3103 (2004)
18. Y. Jiang, S. Abe, T. Ochiai, T. Nozaki, A. Hirohata, N. Tezuka, K. Inomata, Phys. Rev. Lett. **92**, 167204 (2004)
19. Y. M. Huai, F. Albert, P. Nguyen, M. Pakala, T. Valet, Appl. Phys. Lett. **84**, 3118 (2004)
20. R. Moriya, K. Hamaya, A. Oiwa, H. Munekata, Jpn. J. Appl. Phys. Part 2 - Lett. & Express Lett. **43**, L825 (2004)

21. Y. W. Liu, Z. Z. Zhang, J. G. Wang, P. P. Freitas, J. L. Martins, J. Appl. Phys. **93**, 8385 (2003)
22. G. D. Fuchs, N. C. Emley, I. N. Krivorotov, P. M. Braganca, E. M. Ryan, S. I. Kiselev, J. C. Sankey, D. C. Ralph, R. A. Buhrman, J. A. Katine, Appl. Phys. Lett. **85**, 1205 (2004)
23. A. Deac, O. Redon, R. C. Sousa, B. Dieny, J.-P. Nozières, Z. Zhang, Y. Liu, P. P. Freitas, J. Appl. Phys. **95**, 6792 (2004)
24. M. Tsoi, A. G. M. Jansen, J. Bass, W. C. Chiang, V. Tsoi, P. Wyder, Nature **406**, 46 (2000)
25. E. B. Myers, F. J. Albert, J. C. Sankey, E. Bonet, R. A. Buhrman, D. C. Ralph, Phys. Rev. Lett. **89**, 196801 (2002)
26. A. Fabian, C. Terrier, S. S. Guisan, X. Hoffer, M. Dubey, L. Gravier, J. P. Ansermet, J. E. Wegrowe, Phys. Rev. Lett. **91**, 257209 (2003)
27. M. R. Pufall, W. H. Rippard, S. Kaka, S. E. Russek, T. J. Silva, J. Katine, M. Carey, Phys. Rev. B **69**, 214409 (2004)
28. S. I. Kiselev, J. C. Sankey, I. N. Krivorotov, N. C. Emley, R. J. Schoelkopf, R. A. Buhrman, D. C. Ralph, Nature **425**, 380 (2003)
29. I. N. Krivorotov, N. C. Emley, A. G. F. Garcia, J. C. Sankey, S. I. Kiselev, D. C. Ralph, R. A. Buhrman Phys. Rev. Lett. **93**, 166603 (2004)
30. W. H. Rippard, M. R. Pufall, S. Kaka, S. E. Russek, T. J. Silva, Phys. Rev. Lett. **92**, 027201 (2004)
31. W. H. Rippard, M. R. Pufall, S. Kaka, T. J. Silva, S. E. Russek, Phys. Rev. B **70**, 100406(R) (2004)
32. S. I. Kiselev, J. C. Sankey, I. N. Krivorotov, N. C. Emley, M. Rinkoski, C. Perez, R. A. Buhrman, D. C. Ralph, Phys. Rev. Lett. **93**, 036601 (2004)
33. R. H. Koch, J. A. Katine, J. Z. Sun, Phys. Rev. Lett. **92**, 088302 (2004)
34. F. J. Albert, N. C. Emley, E. B. Myers, D. C. Ralph, R. A. Buhrman, Phys. Rev. Lett. **89**, 226802 (2002)
35. F. B. Mancoff, R. W. Dave, N. D. Rizzo, T. C. Eschrich, B. N. Engel, S. Tehrani, Appl. Phys. Lett. **83**, 1596 (2003)
36. M. Tsoi, J. Z. Sun, S. S. P. Parkin, Phys. Rev. Lett. **93**, 036602 (2004)
37. M. AlHajDarwish, H. Kurt, S. Urazhdin, A. Fert, R. Loloee, W. P. Pratt, Jr., J. Bass Phys. Rev. Lett. **93**, 157203 (2004); M. AlHajDarwish, A. Fert, W. P. Pratt, J. Bass, J. Appl. Phys. **95**, 6771 (2004)
38. T. Y. Chen, Y. Ji, C. L. Chien, M. D. Stiles, Phys. Rev. Lett. **93**, 026601 (2004)
39. B. Özyilmaz, A. D. Kent, J. Z. Sun, M. J. Rooks, R. H. Koch, Phys. Rev. Lett. **93**, 176604 (2004)
40. B. T. Jonker, A. T. Hanbicki, D. T. Pierce, M. D. Stiles, J. Magn. Magn. Mater. **277**, 24 (2004)
41. X. Waintal, E. B. Myers, P. W. Brouwer, D. C. Ralph, Phys. Rev. B **62**, 12317 (2000)
42. K. Xia, P. J. Kelly, G. E. W. Bauer, A. Brataas, I. Turek, Phys. Rev. B **65**, 220401 (2002)
43. M. D. Stiles, A. Zangwill, Phys. Rev. **66**, 014407 (2002)
44. *Electron correlations in molecules and solids*, by P. Fulde (Springer-Verlag, New York, 1995); K. Held, D. Vollhardt, European Phys. J. B **5**, 473 (1998); I. Yang, S. Y. Savrasov, G. Kotliar, Phys. Rev. Lett. **87**, 216405 (2001)

45. W. Kohn, L. J. Sham, Phys. Rev. A **140**, 1133 (1965); U. von Barth, L. Hedin, Phys. Rev. B **4**, 1629 (1972); O. Gunnarsson, B. I. Lundqvist, Phys. Rev. B **13**, 4274 (1976); R. O. Jones, O. Gunnarsson Rev. Mod. Phys. **61**, 689 (1989)
46. *Calculated electronic properties of metals* by V. L. Moruzzi, J. F. Janak, A. R. Williams (Pergamon, New York, 1978)
47. K. M. Schep, J. B. A. N. van Hoof, P. J. Kelly, G. E. W. Bauer, J. E. Inglesfield, J. Magn. Magn. Mater. **177**, 1166 (1998); M. D. Stiles, D. R. Penn, Phys. Rev. B **61** 3200 (2000); K. Xia, P. J. Kelly, G. E. W. Bauer, I. Turek, J. Kudrnovsky, V. Drchal, Phys. Rev. B **63**, 064407 (2001); G. E. W. Bauer, K. M. Schep, K. Xia, P. J. Kelly, J. Phys. D, **35**, 2410 (2002)
48. Spatial precession occurs when a coherent superposition of up and down spin states have the same energy (E_{F} in this case) but different wave vectors. The more familiar case of temporal precession occurs when a coherent superposition of up and down spin states have the same wave vector but different energies. In both cases, an accumulation of phase changes the orientation of the spin vector.
49. M. D. Stiles, J. Appl. Phys. **79**, 5805 (1996)
50. L. Berger, IEEE Trans. Magn. **31**, 3871 (1995)
51. C. Heide, P. E. Zilberman, R. J. Elliott, Phys. Rev. B **63**, 64424 (2001); C. Heide, Phys. Rev. Lett. **87**, 197201 (2001); C. Heide, Phys. Rev. B **65**, 054401 (2001)
52. S. Zhang, P. M. Levy, A. Fert, Phys. Rev. Lett. **88**, 236601 (2002)
53. A. Shpiro, P.M. Levy, S. Zhang, Phys. Rev. B **67**, 104430 (2003)
54. W. N. G. Hitchon, R. W. Chantrell, A. Rebei, `cond-mat/0407051`
55. S. Urazhdin, Phys. Rev. B **69**, 134430 (2004)
56. L. Berger, J. Appl. Phys. **81**, 4880 (1997); Phys. Rev. B **59**, 11465 (1999); J. Appl. Phys. **91**, 6795 (2002)
57. M. V. Tsoi, V. S. Tsoi, JETP Lett. **73**, 98 (2001)
58. M. Tsoi, J. Z. Sun, M. J. Rooks, R. H. Koch, S. S. P. Parkin, Phys. Rev. B **69**, 100406 (2004)
59. Y. Tserkovnyak, A. Brataas, G. E. W. Bauer, Phys. Rev. B **67**, 140404 (2003)
60. M. D. Stiles, J. Magn. Magn. Mater. **200**, 322 (1999); P. Bruno, J. Phys.-Cond. Matter **11**, 9403 (1999); D. E. Bürgler, P. Grünberg, S. O. Demokritov, M. T. Johnson, in *Handbook of Magnetic Materials, Vol. 13*, ed. K. H. J. Buschow (2001); M. D. Stiles, Contemporary Concepts of Condensed Matter Science (to be published).
61. S. Yuasa, T. Nagahama, Y. Suzuki, Science **297**, 234 (2002)
62. H. Itoh, J. Inoue, A. Umerski, J. Mathon, Phys. Rev. B **68**, 174421 (2003)
63. G. E. W. Bauer, Y. V. Nazarov, D. Huertas-Hernando, A. Brataas, K. Xia, P. J. Kelly, Mater. Sci. Eng. B-Solid State Mater. Adv. Technol. **84**, 31 (2001)
64. D. M. Edwards, F. Federici, J. Mathon, A. Umerski, Phys. Rev. B **71**, 054407 (2005)
65. M. D. Stiles, A. Zangwill, J. Appl. Phys. **91**, 6812 (2002)
66. L. Berger, IEEE Trans. Magn. **34**, 3837 (1998); J. Appl. Phys. **89**, 5521 (2001)
67. M. D. Stiles, J. Xiao, A. Zangwill, Phys. Rev. B **69**, 054408 (2004)
68. T. Valet, A. Fert, Phys. Rev. B **48**, 7099 (1993)
69. A. Brataas, Yu. V. Nazarov, G. E. W. Bauer, Phys. Rev. Lett. **84**, 2481 (2000); A. Brataas, Yu. V. Nazarov, G. E. W. Bauer, Europhys. Phys. J. B **22**, 99 (2001)

70. J. Xiao, A. Zangwill, M. D. Stiles, Phys. Rev. B **70**, 172405 (2004)
71. A. Brataas, G. E. W. Bauer, Paul J. Kelly, Physics Reports (to be published)
72. J. Zhang, P. M. Levy, S. Zhang, V. Antropov, Phys. Rev. Lett. **93**, 256602 (2004); P. M. Levy, J. Zhang, Phys. Rev. B 70, 132406 (2004); J. Zhang, P. M. Levy, Phys. Rev. B **71**, 184417 (2005); J. Zhang, P. M. Levy, Phys. Rev. B **71**, 184426 (2005)
73. Y. B. Bazaliy, B. A. Jones, S. C. Zhang, Phys. Rev. B **57**, R3213 (1998)
74. J. P. Ansermet, IEEE Trans. Magn. **40**, 358 (2004)
75. J. Grollier, P. Boulenc, V. Cros, A. Hamzić, A. Vaurès, A. Fert, G. Faini, J. Appl. Phys. **95**, 6777 (2004); A. Thiaville, Y. Nakatani, J. Miltat, N. Vernier, J. Appl. Phys. **95**, 7049 (2004); Z. Li, S. Zhang, Phys. Rev. Lett. **92**, 7049 (2004); A. Yamaguchi, T. Ono, S. Nasu, K. Miyake, K. Mibu, T. Shinjo, Phys. Rev. Lett. **92**, 7049 (2004); G. Tatara, H. Kohno, Phys. Rev. Lett. **92**, 7049 (2004); X. Waintal, M. Viret, Europhys. Lett. **65**, 427 (2004); M. Tsoi, R. E. Fontana, S. S. P. Parkin, Appl. Phys. Lett. **83**, 2617 (2003)
76. L. Berger, J. Appl. Phys. **49**, 2156 (1978); *ibid.* **50**, 2137 (1979)
77. Y. Tserkovnyak, A. Brataas, G. E. W. Bauer, Phys. Rev. Lett. **88**, 117601 (2002); A. Brataas, Y. Tserkovnyak, G. E. W. Bauer, B. I. Halperin, Phys. Rev. B **66**, 060404 (2002)
78. Y. Tserkovnyak, A. Brataas, G. E. W. Bauer, B. I. Halperin, Rev. Mod. Phys. (to be published)
79. D. L. Mills, Phys. Rev. B **68**, 014419 (2003)
80. E. Šimánek, B. Heinrich, Phys. Rev. B **67**, 144418 (2003); E. Šimánek, Phys. Rev. B **68**, 224403 (2003)
81. R. Urban, G. Woltersdorf, B. Heinrich, Phys. Rev. Lett. **87**, 217204 (2001)
82. S. Mizukami, Y. Ando, T. Miyazaki, J. Magn. Magn. Mater. **239**, 42 (2002)
83. S. Ingvarsson, L. Ritchie, X. Y. Liu, G. Xiao, J. C. Slonczewski, P. L. Trouilloud, R. H. Koch, Phys. Rev. B **66**, 214416 (2002)
84. P. Lubitz, S. F. Cheng, F. J. Rachford, J. Appl. Phys. **93**, 8283 (2003)
85. B. Heinrich, R. Urban, G. Woltersdorf, E. Šimánek, J. Appl. Phys. **93**, 7545 (2003)
86. K. Lenz, T. Tolinski, J. Lindner, E. Kosubek, K. Baberschke, Phys. Rev. B **69**, 144422 (2004)
87. A. G. Aronov, JETP Lett. **24**, 32 (1977)
88. M. Johnson, R. H. Silsbee, Phys. Rev. B **35**, 4959 (1987)
89. P. C. van Son, H. van Kempen, P. Wyder, Phys. Rev. Lett. **58**, 2271 (1987)
90. I. Zutic, J. Fabian, S. Das Sarma, Rev. Mod. Phys. **76**, 323 (2004)
91. A. Vedyayev, N. Ryzhanova, B. Dieny, P. Dauguet, P. Gandit, J. Chaussy, Phys. Rev. B **55**, 3728 (1997)
92. J. C. Slonczewski, J. Magn. Magn. Mater. **247**, 324 (2002)
93. D. Huertas-Hernando, G. E. W. Bauer, Y. V. Nazarov, J. Magn. Magn. Mater. **240**, 174 (2002)
94. G. E. W. Bauer, Y. Tserkovnyak, D. Huertas-Hernando, A. Brataas, Phys. Rev. B **67**, 094421 (2003)
95. J. Manschot, A. Brataas, G. E. W. Bauer, Phys. Rev. B **69**, 092407 (2004); *ibid*, Appl. Phys. Lett. **85**, 3250 (2004)
96. A. A. Kovalev, A. Brataas, G. E. W. Bauer, Phys. Rev. B **66**, 224424 (2002)
97. A. Fert, V. Cros, J.-M. George, J. Grollier, H. Jaffrès, A. Hamzić, A. Vaurès, G. Faini, J. Ben Youseff, H. Le Gall, J. Magn. Magn. Mater. **69**, 184406 (2004)

98. N. Smith, J. A. Katine, J. R. Childress, M. J. Carey, `cond-mat/0505117`
99. W. P. Pratt, Jr. (private communication)
100. S. Urazhdin, R. Loloee, W. P. Pratt, Jr., Phys. Rev. B **71**, 100401 (2005)
101. L. Berger, J. Magn. Magn. Mater. **278**, 185 (2004)
102. J. Hamrle, T. Kimura, T. Yang, Y. Otani, Phys. Rev. B **71**, 094434 (2005)
103. M. L. Polianski, P. W. Brouwer, Phys. Rev. Lett. **92**, 026602 (2004)
104. F. J. Albert, J. A. Katine, R. A. Buhrman, D. C. Ralph, Appl. Phys. Lett. **77**, 3809 (2000)
105. J. Miltat, G. Albuquerque, A. Thiaville, in *Spin Dynamics in Confined Magnetic Structures I*, B. Hillebrands and K. Ounadjela (Eds,) (Springer Verlag Berlin Heidelberg 2002) pp. 1-33
106. A. Hubert, R. Schäfer: *Magnetic Domains* (Springer-Verlag, Berlin, 1998)
107. J. Z. Sun, Phys. Rev. B **62**, 570 (2000)
108. Y. B. Bazaliy, B. A. Jones, S. C. Zhang, J. Appl. Phys. **89**, 6793 (2001); Y. B. Bazaliy, B. A. Jones, Physica B **329**, 1290 (2003)
109. Y. B. Bazaliy, B. A. Jones, S. C. Zhang, Phys. Rev. B **69**, 094421 (2004)
110. H. W. Xi, Y. M. Shi, J. Appl. Phys. **96**, 1585 (2004); H. W. Xi, K. Z. Gao, Y. M. Shi, Appl. Phys. Lett. **84**, 4977 (2004)
111. Y. Acremann, C. H. Back, M. Buess, D. Pescia, V. Pokrovsky, Appl. Phys. Lett. **79**, 2228 (2001)
112. H. W. Schumacher, C. Chappert, P. Crozat, R. C. Souza, P. P. Freitas, J. Miltat, J. Fassbender, B. Hillebrands, Phys. Rev. Lett. **90**, 017201 (2003) H. W. Schumacher, C. Chappert, R. C. Souza, P. P. Freitas, J. Miltat, Phys. Rev. Lett. **90**, 017204 (2003)
113. T. Devolder, this volume
114. V. K. Melnikov: On the stability of the center for time periodic perturbations, Trans. Moscow Math. Soc. **12**, 1-57 (1963)
115. J. Guckenheimer, P. Holmes: *Nonlinear Oscillations, Dynamical Systems and Bifurcations of Vector Fields* (Springer-Verlag, New York, 1983)
116. T. Devolder, P. Crozat, C. Chapppert, J. Miltat, A. A. Tulapurkar, Y. Suzuki, T. K. Yagami, Phys. Rev. B, Rapid Communications, in the press
117. Z. Li, S. Zhang, Phys. Rev. B **69**, 134416 (2004)
118. D. M. Apalkov, P. B. Visscher, `cond-mat/0405305`; *ibid* J. Magn. Magn. Mater. **286**, 370 (2005)
119. W. F. Brown, Jr., Phys. Rev. **130**, 1677 (1963)
120. S. E. Russek, S. Kaka, W. H. Rippard, M. R. Pufall, T. J. Silva Phys. Rev. B **71**, 104425 (2005)
121. J. Xiao, A. Zangwill, M. D. Stiles, `cond-mat/0504142`
122. C. W. Gardiner: *Handbook of Stochastic Methods* (Springer-Verlag, Berlin Heidelberg New York, 2002)
123. *Numerical Recipes in Fortran 77: The Art of Scientific Computing* by W. H. Press, S. A. Teukolsky, W. T. Wetterling, B. P. Flannery (Cambridge University Press, 2001)
124. S. I. Kiselev, J. C. Sankey, I. N. Krivorotov, N. C. Emley, A. G. F. Garcia, R. A. Buhrman, D. C. Ralph, `cond-mat/0504402`
125. J. Miltat, G. Albuquerque, A. Thiaville, C. Vouille, J. Appl. Phys. **89**, 6982 (2001)
126. Z. Li, S. Zhang, Phys. Rev. B **68**, 024404 (2003)
127. X. C. Zhu, J. G. Zhu, R. M. White, J. Appl. Phys. **95**, 6630 (2004); X. C. Zhu, J. G. Zhu, J. Appl. Phys. **95**, 7318 (2004)

128. J. G. Zhu, X. C. Zhu, IEEE Trans. Magn. **40**, 182 (2004); J. G. Zhu, N. Kim, Y. C. Zhou, Y. F. Zheng, J. W. Chang, K. C. Ju, X. C. Zhu, R. M. White, IEEE Trans. Magn. **40**, 2323 (2004)
129. K.-J. Lee, A. Deac, O. Redon, J.-P. Nozières, B. Dieny, Nature Mater. **3**, 877 (2004)
130. D. Berkov, N. Gorn, Phys. Rev. B **71**, 052403 (2005)
131. B. Montigny, J. Miltat, J. Appl. Phys. **97**, 10C708 (2005)
132. D. Berkov, N. Gorn, `cond-mat/0503754`
133. R. D. McMichael, M. D. Stiles, J. Appl. Phys. **97**, 10J901 (2005) and references cited therein
134. A. A. Tulapurkar, T. Devolder, K. Yagami, P. Crozat, C. Chappert, A. Fukushima, Y. Suzuki, Appl. Phys. Lett. **85**, 5358, (2004); T. Devolder, A. A. Tulapurkar, K. Yagami, P. Crozat, C. Chappert, A. Fukushima, Y. Suzuki, J. Magn. Magn. Mat. **286**, 77, (2005)
135. J. Miltat, A. Thiaville, Science **298**, 555 (2002)
136. A. Thiaville, J. M. Garciá, R. Dittrich, J. Miltat, T. Schrefl, Phys. Rev. B **67**, 094410 (2003)
137. M. Labrune, J. Miltat, J. Appl. Phys. **75**, 2156 (1994)
138. I. N. Krivorotov, N. C. Emley, J. C. Sankey, S. I. Kiselev, D. C. Ralph, R. A. Buhrman, Science **307**, 228, (2005)
139. T. Valet, (2004) unpublished
140. C. Serpico, M. d'Aquino, G. Bertotti, I. D. Mayergoyz, J. Appl. Phys. **95**, 7052 (2004)
141. C. Serpico, M. d'Aquino, G. Bertotti, I. D. Mayergoyz, J. Magn. Magn. Mat. **290-291**, 502, (2005)
142. G. Bertotti, C. Serpico, I. D. Mayergoyz, A. Magni, M. d'Aquino, R. Bonin, Phys. Rev. Lett. **94**, 127206 (2005)

Index